

September 1976

420

GAMMA-RAY ENERGY DEPOSITION IN FAST NUCLEAR REACTORS

Alan D Knipe

A Thesis submitted for the award of  
the Degree of Doctor of Philosophy  
of the University of London

Nuclear Power Group  
Imperial College of Science and Technology

## GAMMA-RAY ENERGY DEPOSITION IN FAST NUCLEAR REACTORS

### ABSTRACT

A series of gamma-ray energy deposition measurements in the zero power fast reactor ZEBRA is described. The purpose of the experiments was to test the adequacy of existing methods of calculation and data. The interpretation of gamma-ray measurements in the fast reactor environment presents several problems. These are discussed in relation to the two experimental techniques employed during the ZEBRA program. A zirconium-walled ionisation chamber and a solid-state cavity dosimeter, utilising the  $\text{Li}^7\text{F}$  thermoluminescent dosimeter (TLD), provided a complete dose-mapping of the reactor assembly. Additionally, energy deposition within control rods and structural materials was measured with the TLD. One of the major difficulties with this type of measurement is the discontinuity that is usually created by the introduction of the detector into the medium of interest. Standard gamma-ray Monte Carlo computer codes are based on the assumption that the energy transferred from a photon to a secondary charged particle is deposited at the point of interaction. The dimensions of typical solid-state integrating dosimeters, such as the TLD, are however comparable with the range of these particles, and therefore this approximation is not valid. A method is described of extending the Monte Carlo process to track the charged particles, thus making it possible to relate the energy deposition in the detector and surrounding media. A benchmark experiment carried out to validate the TLD technique is discussed. The sources of gamma-rays in a fast breeder reactor and the process of energy deposition are outlined. Details of the ionisation chamber and TLD measurements during the ZEBRA program are reported and the results compared with calculated values.

#### ACKNOWLEDGEMENTS

The author wishes to express his appreciation to Dr A J H Goddard of the Nuclear Power Section, Imperial College, and Dr J Butler of the Radiation Physics and Shielding Group, AEE Winfrith, for their assistance and encouragement throughout this work.

The author is indebted to Mr A F Avery, Mr D E Bendall, Mr M J Grimstone, Mr A K McCracken, Dr P C Miller and Mr A Packwood, all of the Winfrith Shielding Group, for many useful discussions.

Sincere thanks are also due to Dr J E Sanders and the ZEBRA team for their assistance during the measurement programs and to the Special Investigations Group, AERE Harwell, for undertaking the TLD readout.

The support of both Imperial College and the United Kingdom Atomic Energy Authority, under whose joint auspices this research was carried out, is gratefully acknowledged.

## CONTENTS

SECTION	TITLE	PAGE
1	INTRODUCTION	1
2	GAMMA-RAY SOURCES IN THE FAST REACTOR AND THE PROCESS OF ENERGY DEPOSITION	4
2.1	Sources of Gamma-Rays	4
2.2	Gamma-Ray Interactions	5
2.3	Charged Particle Interactions	6
2.4	Units of Energy Deposition	8
3	THE MEASUREMENT TECHNIQUES	12
3.1	Ionisation Chambers	12
3.2	Thermoluminescent Dosimeters	19
4	THERMOLUMINESCENT DOSIMETER IRON BLOCK BENCHMARK	32
4.1	Description of the Experiment	32
4.2	The Benchmark Calculations	32
4.3	Discussion of Results	43
5	THE ZEBRA MEASUREMENT PROGRAM	45
5.1	The ZEBRA Facility	45
5.2	The MZB Assembly	46
5.3	The MZC Assembly	50
5.4	Assembly 13/3	50
5.5	Experimental Methods Within ZEBRA	57
6	THE ZEBRA CALCULATIONS	63
6.1	The MZB Assembly Calculations	63
6.2	The MZC Assembly Calculations	73

CONTENTS (Contd.)

SECTION	TITLE	PAGE
6.3	Corrections to the Measurements	77
6.4	Discussion of the Results	87
7	CONCLUSIONS	101
	APPENDICES	
A	Calibration Sheet for Type IG8 Ionisation Chambers	104
B	Ionisation Chamber Neutron Sensitivity Experiment	105
C	The Monte Carlo Program PROCEED	113
D	List of Symbols	146
	REFERENCES	152

TABLES

NUMBER	TITLE	PAGE
1	Results from the Iron Block Benchmark	43
2	The MZB Measurement Program	47
3	Region Compositions for the MZB(2) Assembly	64
4	Reaction Rates and Source Strengths (MZB McGID Calculation)	67
5	Source Energy Spectra for the MZB Radial Calculations	68
6	Cross-Sections for Gamma-Ray Production from Inelastic Scatter	70
7	Percentage Contributions to the Dose-Rates in MZB	73
8	Percentage Contributions to the Dose-Rates in MZC	74
9	Magnitude of the Neutron Sensitivity Correction ( $-C_1\%$ ) and Non-Saturation of Fission Product Activity Correction ( $+C_2\%$ ) for Ionisation Chamber Measurements - Dose-Rates ( $D \text{ rad hr}^{-1}$ ) at the Core Centre and Mid-Blanket	79
10	1D McGID Calculation - Radial Scan Gamma Dose-Rates ( $Zr, \text{ rad hr}^{-1}$ )	81
11	The Ratio of the Fission Product Photon Source at Time of Measurement ( $f_t$ ) to the Source at Saturation ( $f_s$ ) for the MZB Histories	86
12	The MZC Results	98
13	Gamma DMSA Pattern A	99
14	Gamma DMSA Pattern B	99
B1	Calculated Neutron Recoil Dose-Rates ( $\text{rad hr}^{-1}$ ) at the MZB Centre Plane	109
B2	Experimental and Calculated Values for $S_c$	111
C1	The Functions $f^{(n)}$ used in Molière's Theory of Multiple Scattering	130
C2	$\text{Li}^7\text{F}$ Mass Energy Absorption Coefficients	133

TABLES (Contd.)

NUMBER	TITLE	PAGE
C3	$\epsilon_w / \epsilon_c$ as a Function of Cavity Size for Lead Wall and Carbon Cavity at 0.66 MeV	133
C4	Data for the PROCEED Calculations	137
C5	PROCEED Input Data	139

## FIGURES

NUMBER	TITLE	PAGE
1	Type IG8 Ionisation Chamber (Graphite Lined)	14
2	Block Diagram for the Current Measuring Assembly (C1X 1092 B)	16
3	The TLD Readout Cycle	21
4	Typical $\text{Li}^7\text{F}$ (TLD-700) Dose Response Curve	23
5	The Neutron Sensitivity of $\text{Li}^7\text{F}$ (TLD-700)	26
6	The Thermoluminescent Dosimeter Iron Block Benchmark	33
7	Example of the Calculated Probability of Scatter Using Legendre Expansion	38
8	Photon Spectra 100 mm from $\text{Co}^{60}$ Source in the Iron Block Benchmark	42
9	Core and Breeder Cell Types	48
10	MZB Loading Pattern	49
11	Dimensions and Cell Layout of MZB RZ Model	49
12	General Arrangement of the MONJU Mock-Up Control Rods	51
13	The MZC MONJU Mock-Up Rod Positions	51
14	Assembly 13/3 Core Plan	52
15	An Example of Results from the ZEBRA Multi-Chamber Scanning System in Assembly 13/3	53
16	The Gamma-Ray Energy Deposition DMSA	55
17	Pin Fuelled Calandria Containing the Gamma DMSA	56
18	ZEBRA Element Drawer Arrangement	59
19	Photon Spectra in the MZB(2) Assembly (McGID Calculations)	72
20	MZB(2) Fission Product Gamma Build-Up Curves (Full Power)	83
21	MZB(2) Fission Product Gamma Decay Curves (after 7 hour full power run)	83



FIGURES (Contd.)

NUMBER	TITLE	PAGE
22	Comparison of Monte Carlo Calculation of Absorbed Dose-Rate and Ionisation Chamber Measurements Along Major Axis of Assembly MZB(2)	91
23	Comparison of Monte Carlo Calculation of Absorbed Dose-Rate and TLD Measurements Along Major Axis of Assembly MZB(2)	92
24	Comparison of Monte Carlo Calculation of Absorbed Dose-Rate and Ionisation Chamber Measurements Along Central Vertical Axis of Assembly MZB(2)	93
25	Comparison of Monte Carlo Calculation of Absorbed Dose-Rate and TLD Measurements Along Central Vertical Axis of Assembly MZB(2)	94
26	Absorbed Dose-Rate Along Major Axis of Assembly MZB(3) Measured with TLD	95
27	TLD Axial Scans in Assembly MZB(2) (No Cavity Correction Applied)	96
28	ZEBRA MZB Gamma Dose Rate Distribution	97
29	Oxide Breeder Radial Scan in Assembly 13/3	100
C1	A Schematic of the Program PROCEED	116
C2	Flow Diagram for the Calculation of the Relative Number of Photon Interactions in the Wall and Cavity Regions	122
C3	Angular Distribution of Multiply Scattered Electrons in Aluminium	127
C4	The Cavity Correction Ratio $\epsilon_w / \epsilon_c$ as a Function of Energy for a 1 mm x 1 mm x 6 mm Li <sup>7</sup> F Cavity Surrounded by Various Materials Without Multiple Scattering	134
C5	The Calculated Energy Deposition, as a Function of Energy, in a 1 mm x 1 mm x 6 mm Cavity Containing Ta( $\epsilon_w$ ) and Li <sup>7</sup> F( $\epsilon_c$ ) While Surrounded by Tantalum Without Multiple Scattering	135
C6	The Cavity Correction Ratio $\epsilon_w / \epsilon_c$ as a Function of Energy for a 1 mm x 1 mm x 6 mm Li <sup>7</sup> F Cavity Surrounded by Various Materials With Multiple Scattering	136

## 1 INTRODUCTION

Gamma-rays are a significant heat source in a fast nuclear reactor since their absorption contributes approximately ten per cent to the total reactor energy. The optimisation of cooling and shielding requirements demands reliable data and methods of calculation in order to predict accurately energy deposition and penetration. A stringent test of the adequacy of data and methods is provided by comparison with experimental results from zero power fast reactor assemblies. Such a comparison was carried out in a mock-up of the Prototype Fast Reactor (PFR) in ZEBRA at the UKAEA Winfrith [1]. The predicted gamma-ray dose-rates were lower than the measurements by 20% in the core, increasing to a factor of two in the reflector region. Similar measurements were carried out at zero power facilities in other countries and in some cases corresponding observations were reported. The conclusion drawn from this study was that the discrepancies were due to errors either in the photon source data or in the measurements. The initial object of the present work was to resolve the discrepancies in the PFR mock-up study.

Although many accurate dosimeters are available [2], the fast reactor environment complicates the absolute accurate measurement of gamma-ray energy deposition. Ionisation chambers were chosen as the basic technique because they are well established and were used by Adamson [1] in the previous study. A solid-state integrating dosimeter, namely the  $\text{Li}^7\text{F}$  thermoluminescent dosimeter (TLD), was selected as a second method. A solid-state cavity dosimeter (SSCD) was devised for comparative dose-mapping with the ionisation chambers. However, the interest in TLD was mainly due to its small size, and the project progressed to the development of the TLD technique for the accurate

measurement of energy deposition within control rod mock-ups and demountable sub-assemblies (DMSA's) which contained various test materials.

Gamma-ray energy deposition was studied in several ZEBRA assemblies during this work and many measurements were made whilst developing the experimental techniques. For the purposes of this thesis selected measurements, made during two major programs, are described. Details of the assemblies and measurements are given in section 5, together with the problems of detector access and operation within ZEBRA. Section 3 describes the characteristics and calibration of the ionisation chambers and thermoluminescent dosimeters. Adjustments to the measured values were minimised by careful design of the experiments. However, corrections to account for the non-saturation of fission product activity at the time of measurement, and the detectors' sensitivity to neutrons, were necessary. The procedures for obtaining these corrections, and their magnitudes, are examined in section 6 for each set of measurements. A study of the ionisation chamber's neutron sensitivity, which also provided a test of published values for the average energy required by a recoil nucleus to produce one ion pair, is described in Appendix B.

One of the major difficulties in measuring the energy deposited directly in a material is the discontinuity created by the detecting medium. In order to relate the energy absorbed per unit mass in the detecting medium to the energy absorbed per unit mass in the surrounding medium it is necessary to use a suitable "cavity theory" [3]. These range from the Bragg-Gray theory which is valid only for small gas-filled cavities, to the general theory of cavity ionisation by

T E Burlin which is considered to be applicable to most situations. Standard calculational methods for predicting energy deposition in reactors do not account for the migration of secondary charged particles. Gamma-ray Monte Carlo codes assume that the energy transferred from a photon to an electron or positron is deposited at the point of interaction. The validity of the direct application of the Burlin theory to measurements in ZEBRA was questionable and therefore the Monte Carlo method was extended to track the secondary charged particles in the region of the detector (Appendix C). Predictions of the cavity correction by this method have been examined in relation to results from the Burlin theory. A benchmark experiment, described in section 4, was designed to investigate the correction in the absence of reactor environment complications. The benchmark study highlighted various shortcomings in the discrete-ordinate and Monte Carlo methods of calculating photon spectra and energy deposition.

Test materials from the benchmark experiment were used in DMSA experiments in the ZEBRA Assembly 13. During the MOZART program [4] the measurement of gamma-ray energy deposition within control rod mock-ups, and a comprehensive dose-mapping of ZEBRA, was carried out. The analysis of these measurements, and possible sources of error in the methods of calculation and data, are described in section 6.

This section outlines the main sources of gamma-rays arising within a fast reactor; the relative importance of these sources is discussed in relation to the MZB(2) calculations in sub-section 6.1. The general principles of gamma-ray energy deposition are introduced and for further information the reader is referred to "Radiation Dosimetry" [2]. The basic quantities and units are also defined, following the International Commission on Radiation Units specification [5].

## 2.1 Sources of Gamma-Rays

### 2.1.1 Prompt Fission Gamma-Rays

Prompt gamma-rays from fission are those emitted in apparent coincidence with the fission event (ie delay of about a microsecond).

### 2.1.2 Fission Product Decay Gamma-Rays

Following fission the fission fragments are unstable and may emit at least one photon while decaying. The period over which this energy is released is determined by the half-lives of the nuclei in the decay chains.

### 2.1.3 Neutron Radiative Capture Gamma-Rays

As a result of neutron absorption, a nucleus gains excitation energy equal to the binding energy plus its kinetic energy. The compound nucleus so formed may lose this excitation energy in various ways. In radiative capture, de-excitation occurs by the prompt emission (ie about  $10^{-12}$  seconds after the capture event) of gamma-rays, leaving the nucleus in its ground state. Only a few elements emit a single photon and emission usually goes through intermediate excited states producing up to four photons. Where

de-excitation leads to the emission of protons or alpha-particles these processes may also be accompanied by gamma-rays.

#### 2.1.4 Neutron Inelastic Scattering Gamma-Rays

When a neutron undergoes inelastic scattering it is first captured to form a compound nucleus. A neutron of lower kinetic energy is then expelled, leaving the target nucleus in an excited state. The target nucleus returns to its ground state by emitting one or more gamma-rays approximately  $10^{-14}$  seconds after the scattering event.

#### 2.1.5 Radioactive Decay Gamma-Rays

When a nucleus absorbs a neutron it becomes unstable. After this instability is relieved by the emission of capture gamma-rays the nucleus may be radioactive and, in the process of decaying, emit further gamma-rays.

#### 2.1.6 Bremsstrahlung

Bremsstrahlung are photons emitted as a result of the change of velocity of a charged particle in the electric field of an atom. They must also be considered as a secondary source of photons.

#### 2.1.7 Annihilation Radiation

One or two photons may result from positron annihilation. This is usually of no importance as a primary source of gamma-rays but must be considered following pair-production (sub-section 2.2.3).

### 2.2 Gamma-Ray Interactions

Gamma-rays of the energies produced in a reactor transfer their energy to secondary particles through the following three main competing interactions.

### 2.2.1 Photoelectric Absorption

The photoelectric effect is significant only at low energies and the cross-section increases with decreasing energy. In a photoelectric collision total absorption of the photon takes place and a bound atomic electron is ejected with kinetic energy equal to the original photon energy less the electron binding energy. Momentum is conserved by the recoil of the residual atom and the binding energy is emitted promptly, as low energy photons and Auger electrons, from the filling of the inner shell vacancy.

### 2.2.2 Compton Scattering

Compton scattering is competitive with both photoelectric absorption and pair-production with a cross-section exceeding them at intermediate energies. Unlike photoelectric absorption the incident photon cannot be completely absorbed by a loosely bound or free electron. The energy of the incident photon is shared between the recoil electron and the scattered photon.

### 2.2.3 Pair-Production

A photon of energy above  $2m_0c^2$  can produce a positron-electron pair, the cross-section for this event increasing with increasing energy. The process takes place in the field of a charged particle, usually an atomic nucleus but to some degree in the field of an atomic electron at energies above  $4m_0c^2$ .

## 2.3 Charged Particle Interactions

The complex collision processes of the electrons and positrons produced through neutron and photon interactions can be divided into four broad categories and these are outlined in the following sub-sections. The energy deposition in a medium by these charged particles appears as

heat or produces chemical changes in the medium.

### 2.3.1 Inelastic Collisions with Atomic Electrons

In a collision with an atomic electron the incident particle both loses energy and changes direction. The cross-section for the scattering of electrons by electrons is given by Møller and for positron-electron scattering by Bhabha as described in References [6] and [7]. Inelastic collisions are the predominant mechanism for energy transfer at reactor energies. If the energy transferred to an electron is only enough to raise it to a higher energy level in the atom the process is called excitation. However, if the electron can separate completely from the atom the process is called ionisation. Energetic electrons that are ejected in the process are termed delta-rays.

### 2.3.2 Elastic Collisions with an Atom

In elastic scattering, particularly with the atomic nucleus, the incident particle is deflected but only loses the kinetic energy required to conserve momentum. The exact cross-section is given by Mott (outlined in Reference [7]) and incident particles have a high probability of experiencing nuclear elastic scattering. Electrons with energies below the atom's excitation energy can also interact with the coupled system of the nucleus and atomic electrons.

### 2.3.3 Radiative Collisions with an Atom

Deceleration or acceleration of a charged particle in the electric field of an atom, mainly the nucleus, may result in the emission of bremsstrahlung. Bremsstrahlung cross-section formulae are reviewed by Koch and Motz [8]. The process becomes important at



higher energies.

#### 2.3.4 Positron Annihilation

If a positron encounters an electron, annihilation results with the production of one or more photons, two-quanta annihilation having the greater probability. The probability of one-quantum annihilation is generally much smaller than that for the two-quanta process, although in high-Z elements it accounts for up to 15% of the total annihilations. Heitler [9] shows that below 20 MeV 85% of all positrons come to rest before annihilation and that two photons of similar energy are emitted in opposite but randomly orientated directions.

### 2.4 Units of Energy Deposition

The energy deposited by gamma-rays is through the secondary charged particles. The energy imparted to a medium will be subject to random fluctuations if the volume of interest or the fluence of particles is small. Obviously for meaningful results from experiments and calculations macroscopic quantities of energy deposition must be defined.

#### 2.4.1 Kerma

The kerma  $K$  is the quotient of  $dE_k$  by  $dm$  where  $dE_k$  is the sum of the initial kinetic energies of all the charged particles liberated by indirectly ionising particles in a volume element of mass  $dm$  in a specified material. The kerma-rate is the quotient of  $dK$  by  $dt$  where  $dt$  is the time interval.

#### 2.4.2 Absorbed Dose

The absorbed dose is the quotient of  $dE_p$  by  $dm$  where  $dE_p$  is the energy imparted by gamma-rays in a volume element of mass  $dm$ .

The special unit of energy absorption (absorbed dose) was until recently the "rad", and this is used throughout the thesis.

$$1 \text{ rad} = 10^{-2} \text{ J Kg}^{-1}$$

The energy absorption rate (absorbed dose-rate), D, is expressed in rad hr<sup>-1</sup>.

However, it should be noted that the internationally adopted unit for absorbed dose is now the "gray":

$$1 \text{ Gy} = 1 \text{ J Kg}^{-1} = 100 \text{ rad}$$

Other units for energy deposition are sometimes convenient and the following relationships exist:

$$1 \text{ MeV g}^{-1} \text{ sec}^{-1} = 1.60219 \times 10^{-13} \text{ W g}^{-1}$$

$$1 \text{ W g}^{-1} = 3.6 \times 10^8 \text{ rad hr}^{-1}$$

$$1 \text{ MeV g}^{-1} \text{ sec}^{-1} = 5.76788 \times 10^{-5} \text{ rad hr}^{-1}$$

(Unit conversion constant k)

#### 2.4.3 Mass Attenuation Coefficient

For gamma-rays the mass attenuation coefficient  $\mu/\rho$  is defined by:

$$\frac{\mu}{\rho} = \frac{1}{\rho N} \frac{dN}{dx} \text{ cm}^2 \text{ g}^{-1} \quad \text{--- (1)}$$

where  $dN/N$  is the fraction of photons that experience interactions in traversing a distance  $dx$  in a medium of density  $\rho$ .

$\mu$  is sometimes referred to as the macroscopic photon interaction cross-section (cm<sup>-1</sup>). The microscopic cross-section  $\sigma$  is given by:

$$\sigma = \frac{\mu}{\rho} \frac{A}{N_A} \text{ cm}^2/\text{atom} \quad \text{--- (2)}$$

where  $A$  is the atomic weight and  $N_A$  is the Avagadro constant.

#### 2.4.4 Mass Energy Transfer Coefficient

For gamma-rays the mass energy transfer coefficient  $\mu_k/\rho$  is defined by:

$$\frac{\mu_k}{\rho} = \frac{1}{\rho E} \frac{dE_k}{dx} \quad \text{cm}^2 \text{ g}^{-1} \quad \text{--- (3)}$$

where  $dE_k/E$  is the fraction of incident photon energy (excluding rest energies) that is transferred to the kinetic energy of the secondary electrons in traversing a distance  $dx$ . Therefore the energy of scattered photons, fluorescence radiation and annihilation radiation are not included.

#### 2.4.5 Mass Energy Absorption Coefficient

For gamma-rays the mass energy absorption coefficient  $\mu_{en}/\rho$  is defined by:

$$\frac{\mu_{en}}{\rho} = \frac{\mu_k}{\rho} (1 - g) \quad \text{cm}^2 \text{ g}^{-1} \quad \text{--- (4)}$$

where  $g$  is the fraction of the energy of secondary electrons that is lost to bremsstrahlung in the medium.

#### 2.4.6 Mass Stopping Power

The mass stopping power  $S/\rho$  for electrons in a medium is defined by:

$$\frac{S}{\rho} = \frac{1}{\rho} \frac{dE}{dx} \quad \text{MeV cm}^2 \text{ g}^{-1} \quad \text{--- (5)}$$

where  $dE$  is the energy lost by the charged particle of specified energy in traversing a distance  $dx$ .

#### 2.4.7 Linear Energy Transfer

The linear energy transfer, LET, for charged particles in a medium is defined by:

$$\text{LET} = \frac{dE_{\text{LET}}}{dx} \quad \text{erg cm}^{-1} \quad \text{--- (6)}$$

where  $dE_{\text{LET}}$  is the average energy locally imparted to a medium by a charged particle of specified energy in traversing a distance  $dx$ .

The term locally imparted may mean a range or energy cut-off.

#### 2.4.8 Half-Value Thickness

The half-value thickness (HVT) is defined as the thickness of absorber that will reduce the intensity of a narrow beam of radiation to one half when the absorption is exponential:

$$\text{HVT} = \ln 2 / \mu \quad - - - (7)$$



### 3 THE MEASUREMENT TECHNIQUES

#### 3.1 Ionisation Chambers

This section outlines the theory of the Bragg-Gray ionisation chamber and describes those used in the ZEBRA work. The calibration of the chambers and the considerations necessary when using them in the reactor are also discussed.

##### 3.1.1 The Bragg-Gray Equation

The Bragg-Gray equation relates the amount of ionisation produced in a gas cavity to the energy absorbed in the surrounding wall medium. The theory has recently been re-examined by Burlin [3]. Gamma-ray interactions in the wall medium produce a charged particle spectrum. The relationship between the gamma-ray energy deposition per unit mass in the wall medium ( $E_w$ ) and the ionisation per unit mass in the gas cavity ( $E_c$ ) can be written as:

$$\begin{aligned} E_w &= E_c \left( \frac{S}{\rho} \right)_w / \left( \frac{S}{\rho} \right)_c \\ &= W_e J \left( \frac{S}{\rho} \right)_w / \left( \frac{S}{\rho} \right)_c \quad \text{--- (8)} \end{aligned}$$

where  $\left( \frac{S}{\rho} \right)_w$  is the mass stopping power in the wall medium;

$\left( \frac{S}{\rho} \right)_c$  is the mass stopping power in the gas cavity;

$W_e$  is the average energy expended in the gas to form one ion pair;

$J$  is the number of ion pairs per unit mass of gas.

Equation (8) is the Bragg-Gray equation and is based upon three assumptions:

- (i) The charged particle spectrum set up in the wall medium is

not modified by the gas cavity.

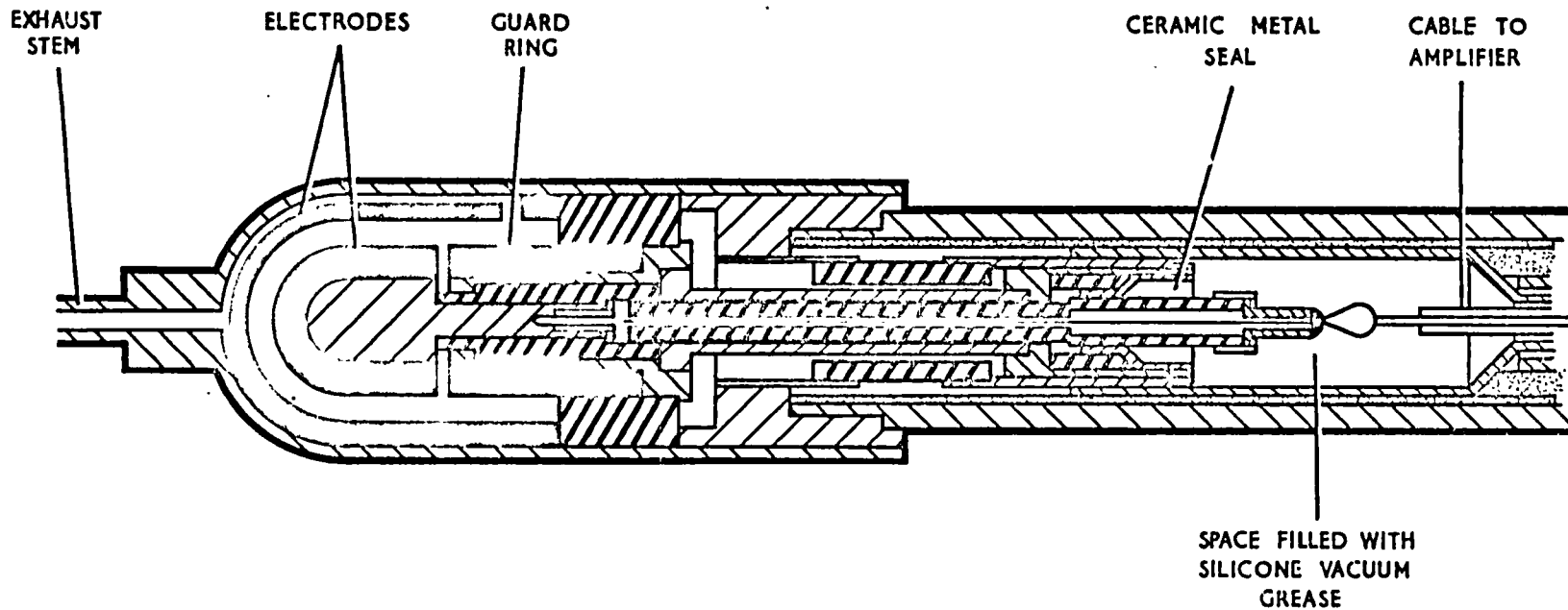
- (ii) Photon interactions in the cavity itself produce a negligible contribution to the measured ionisation.
- (iii) The charged particles lose energy continuously.

When the wall medium is exposed to a spectrum of gamma-ray energies the stopping powers must be averaged over the charged particle spectrum set up in the cavity. The various advances in cavity theory are discussed later in the thesis.

### 3.1.2 Description of the Ionisation Chambers

The ionisation chambers, type IG8, were designed and developed by the Electronics and Applied Physics Division, AERE Harwell, and made by 20th Century Electronics Ltd. The design of the chambers was based on the Bragg-Gray assumptions. However, they were not intended as absolute dosimeters and rely upon calibration in a known gamma-ray field.

The following description is of the zirconium-walled chamber used in the MZB dose-rate measurement program. Three carbon-walled chambers of identical type were used in an attempt to measure the chamber's neutron sensitivity (Appendix B). The electrode geometry was hemispherical-cylindrical and the 2 mm gas gap was filled with argon at a pressure of 450 mm Hg. The active volume of the chamber was  $1304 \text{ mm}^3$ . The outer zirconium electrode was 0.76 mm thick and the whole chamber was enclosed within a thin aluminium case giving an overall diameter of 22.5 mm. The tip of the chamber stem to the geometric centre of the active volume was 38 mm. The usual precautions to reduce secondary ionisation sites such as filling the gas seal and cable connections with



GRAPHITE



ALUMINA



HIGH DENSITY POLYTHENE



OTHER STRUCTURAL MATERIAL



{	ALUMINIUM	}	IN CHAMBER HEAD
	MAGNOX		
	NICKEL		IN SEALS AND CONNECTIONS

TYPE IG 8 IONISATION CHAMBER (GRAPHITE LINED)  
FIGURE 1

silicone grease were of course taken. One of the type IG8 chambers is illustrated in Figure 1.

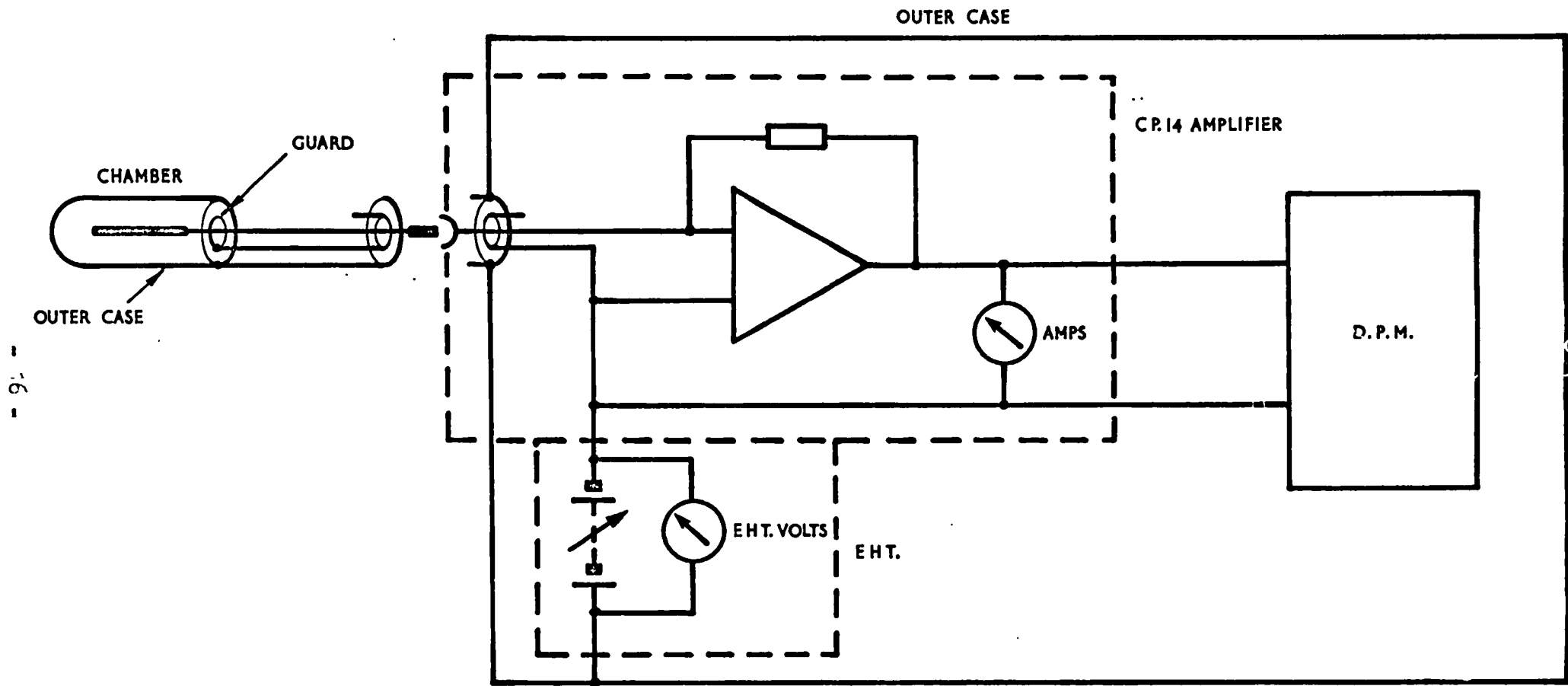
The wall thickness of an ionisation chamber is decided by two factors. From the point of view of cavity theory the wall thickness must be equal to the range of the maximum energy electron produced by the photon interactions in the wall medium (the equilibrium thickness). The wall can be considered an infinite medium as no electrons being generated at greater distances can reach the cavity, although it must be ensured that particles originating outside the chamber cannot enter the cavity. However the wall, besides generating the charged particles also absorbs and scatters the primary photons, and thus disturbs the gamma-ray field. It is therefore desirable to keep dimensions to a minimum. Various calculations [10] have shown that in practice it is not necessary for the wall thickness to be equal to the maximum electron range.

Ideally, the wall material and gas should be of identical atomic composition. However, for an unmatched situation the Bragg-Gray principle is fulfilled provided the gas gap is very much less than the mean-free-path of the secondary electrons. These conditions were met in the design of the IG8 chambers. The dimension of both the zirconium and carbon walls was approximately 10 half-value-thicknesses at 1 MeV. The corresponding figure for the gas gap in the 450 mm Hg chambers was 0.0043.

### 3.1.3 Description of the Current Measuring Devices

In order to reduce leakage current through the insulation a guard ring was maintained at the same potential as the centre collector





- 9: -

BLOCK DIAGRAM FOR THE CURRENT MEASURING ASSEMBLY (CIX 1092 B)

FIGURE 2

electrode. Special screened leads from the chamber helped to eliminate leakage despite the long cables necessary to reach the amplifier. From the practical operations point of view, it was simpler to insulate the amplifier from ground rather than the chamber which is manipulated in the reactor. This required the amplifier to float at the polarising voltage of 90 volts. Several current measuring systems were used during this work, leading to the development of the CIX 1092 B current measuring assembly, a block diagram of which is given in Figure 2. This was made by Cooknell Electronics, Weymouth, in co-operation with the Control and Instrumentation Division, AEE Winfrith. The CP14 amplifier had a stability of better than 0.5%/annum in the  $10^{-10}$  -  $10^{-12}$  amp range applicable to the ZEBRA work. The amplifier systems were current calibrated by the Instrument Section, AERE Harwell, in order for the intercomparison of results.

#### 3.1.4 Calibration of the Ionisation Chambers

Five type IG8 ionisation chambers were calibrated against a Farmer secondary standard X-ray dosimeter Mk 2 (Nuclear Enterprises Ltd) in a low scatter cell at the Isotope Production Unit, AERE Harwell. The Farmer dosimeter was calibrated at the National Physical Laboratory (July 1972) against their primary standard.

The Farmer dosimeter was used to measure the exposure rate at one metre from a  $\text{Co}^{60}$  source and a  $\text{Cs}^{137}$  source in turn. The saturation characteristics for each chamber were obtained for both sources. The currents were adjusted according to the current calibration. To convert the exposure-rate ( $R$  Roentgen  $\text{hr}^{-1}$ ) to the absorbed dose-rate ( $D$  rad  $\text{hr}^{-1}$  in zirconium or carbon), the

following expression was used:

$$D = 0.869R \frac{\left(\frac{\mu_{en}}{\rho}\right)_{Zr,C}}{\left(\frac{\mu_{en}}{\rho}\right)_{air}} \quad - - - (9)$$

(One Roentgen of gamma radiation produces in dry air under charged particle conditions 0.869 rad. This value takes the mean energy expended by an electron per ion pair produced in air ( $W_{air}$ ) to be 33.7 eV/ion pair [62].)

The mass energy absorption coefficients were taken from Hubbell's compilation [11]. The values for zirconium were obtained by interpolation. The coefficients for Fe, Co, Sn and Pb were converted to cross-sections per atom because of the dependence on the atomic weight. A cubic spline interpolation was carried out at each energy required. The mass energy absorption coefficients for Cs<sup>137</sup> ( $E_{\gamma} = 0.6616$  MeV) and Co<sup>60</sup> ( $E_{\gamma} = 1.17323$  MeV and 1.33248 MeV) were obtained from a cubic spline interpolation of the air, carbon and zirconium data. For Co<sup>60</sup> the mean value of the coefficients at the two energies was obtained. The calibration sheet is reproduced in Appendix A giving the gamma sensitivity (amps/rad hr<sup>-1</sup>) for each chamber. The standard deviation in the exposure-rate measured with the Farmer secondary standard dosimeter was 1.5%. In converting this to the absorbed dose-rate the standard deviation was 3.9%. This gave a 6.4% standard deviation in the ionisation chamber's sensitivity, the largest part of this uncertainty was due to the precision of the current measurement. This was quoted by the Instrument Section, AERE Harwell, as  $\pm 5\%$  in the range  $10 \times 10^{-10}$  to  $3 \times 10^{-11}$  amps and  $\pm 10\%$  in the

range  $10 \times 10^{-12}$  to  $3 \times 10^{-12}$  amps.

It was also necessary to obtain the neutron sensitivity of an ionisation chamber. This was carried out in ZEBRA using three carbon-walled chambers. The experiment, described in Appendix B, provided useful information on the neutron response of the IG8 chambers and decided the method of applying the correction for neutron interactions (sub-section 6.3).

### 3.2 Thermoluminescent Dosimeters

High sensitivity  $\text{Li}^7\text{F}$  (0.007%  $\text{Li}^6$  and 99.993%  $\text{Li}^7$ ), manufactured by the Harshaw Chemical Company under the name TLD-700 in the form of a solid rod 1 mm x 1 mm x 6 mm was chosen for this work. Thermoluminescent lithium fluoride has been investigated by many workers [12-16]. The  $\text{Li}^7\text{F}$  crystals are found to operate over a wide dose-range; exhibit high sensitivity; relatively low neutron sensitivity, and the reproducibility by manufacturers is established. Provided care is exercised when handling the crystals, accurate, reproducible results can be achieved, and the dosimeters can be utilised for several experiments following suitable annealing. The sub-sections below outline the mechanism and experimental technique for the  $\text{Li}^7\text{F}$  dosimeters and deal with the relationship, in the fast reactor environment, between the integrated thermoluminescent light output and the required gamma-ray energy deposition.

#### 3.2.1 The Mechanism of Thermoluminescence

The excitation of an atom is usually rapidly transferred to surrounding atoms and appears as heat. However, radiation can induce several changes in a solid and in some materials a minute fraction can be stored in metastable states. In the process of

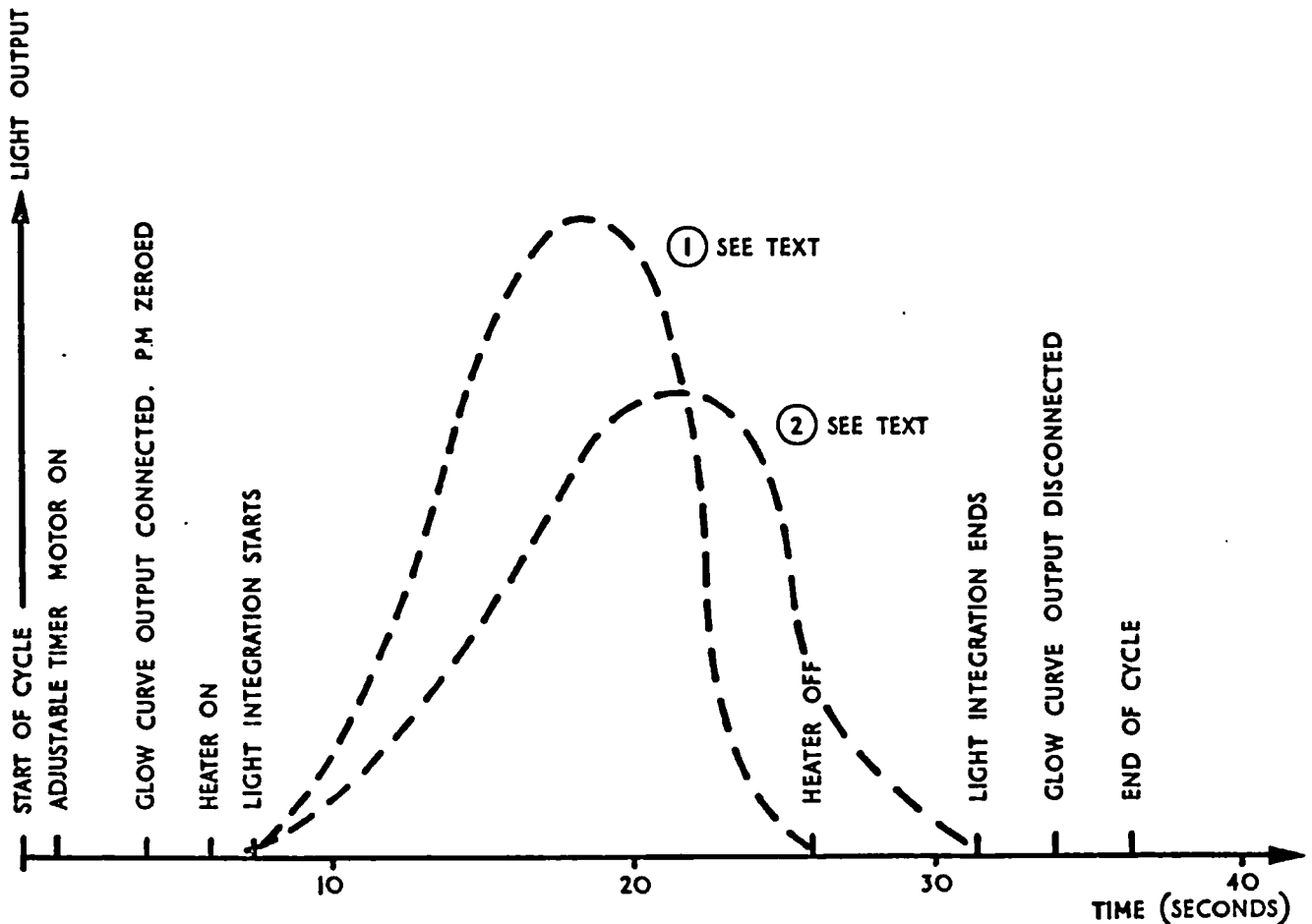
thermoluminescence some of this energy can be recovered if the material is heated.

The structure of LiF consists of two interpenetrating cubic lattices of alkali and halide ions. Real crystals are not an uninterrupted alternation of alkali and halide ions but contain many structural imperfections. These include ion vacancies and ions displaced from regular lattice positions into interstitial positions. Although the crystal must be electrically neutral the defects form localised regions of charge and metastable states are associated with these defects. The regions form "traps" for the charged particles generated by radiation. As the crystal is heated following irradiation the probability of releasing any particular particle from a trap is increased and at some temperature it is almost certain to be released. Upon recombination, a photon in the visible region of the spectrum is produced. Thus the light intensity from a crystal gradually builds up to a maximum and then decreases, giving a characteristic "glow curve". In order to control the emission spectrum and optimise the thermoluminescent process the LiF crystal is "doped" with activators such as Eu, Ca, Ti, Ag, Na, Ir, Si, Sm, La and their effect is enhanced when used with magnesium. In the reactor environment additional vacancies and interstitials may be produced by fast neutrons, the alpha-particles and tritons from the thermal  $\text{Li}^6(n,\alpha)t$  reaction and, to a much lesser degree fast electrons and photons themselves.

### 3.2.2 TLD Readout System

During this work the crystals were read out using an Isotopes/Con-Rad Model 7100 TLD Reader. In this particular reader the crystals were placed on a nichrome planchet which, when loaded into

the reader, became part of the electrical heating circuit (ie the current flowed through the planchet). The light output was measured with a photomultiplier tube operating in the current mode with an ADC circuit producing pulses which were fed to a 4-decade scaler. In addition to the integrated light output there was a glow curve output. The heating and reading cycle is illustrated by Figure 3.



THE TLD READOUT CYCLE  
FIGURE 3

The constant rate of heating was determined by the current through the planchet. This was chosen such that when the glow curve output had returned to zero (or at worst one third up the main peak), the heater current would switch off. Curves (1) and (2) in Figure 3 represent glow curves produced by the upper and lower limits of

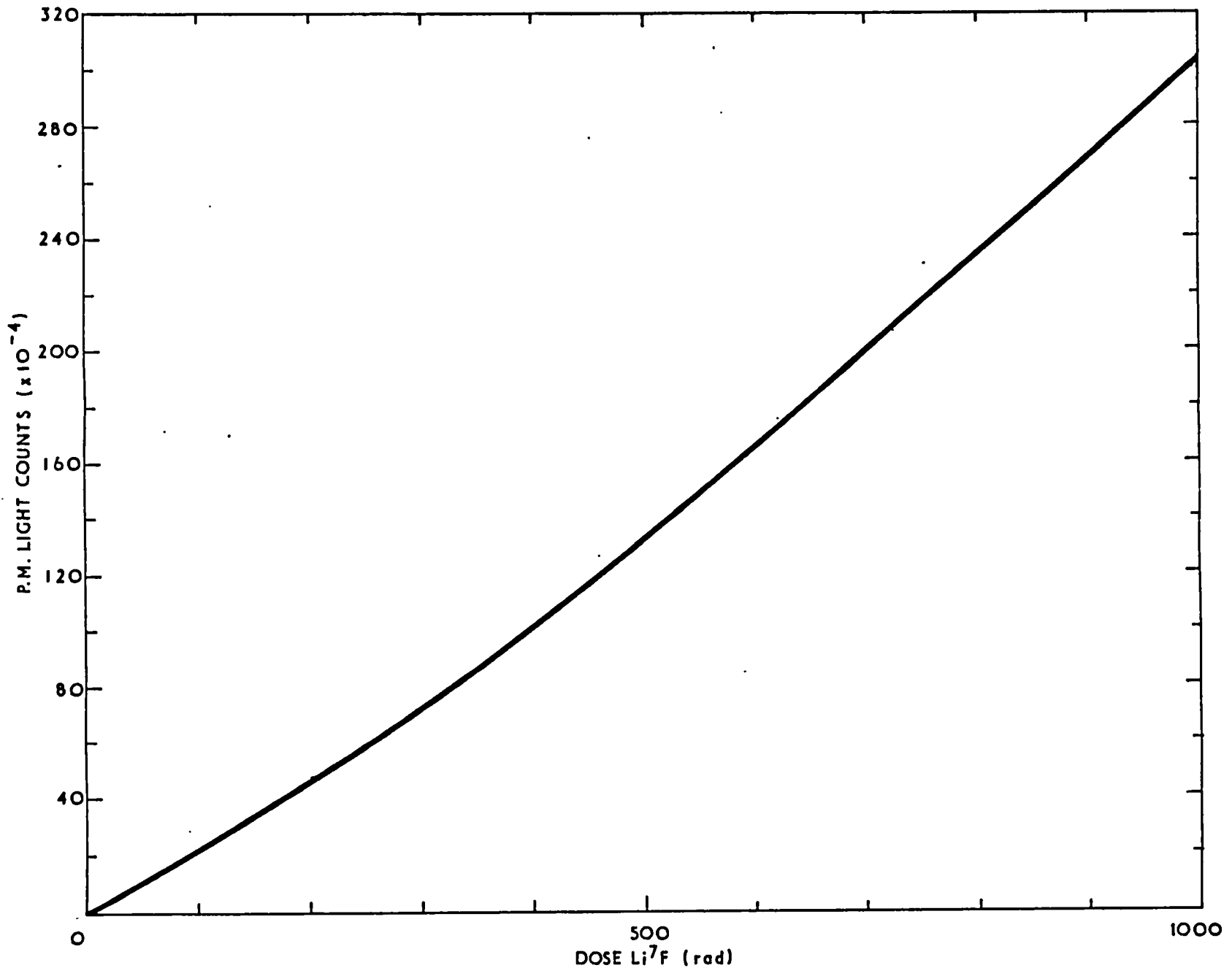
acceptable heater currents. A stable light source was substituted for the planchet at frequent intervals to check drifts in the photomultiplier gain and all readout counts were normalised to a standard light source reading. Prior to readout all the irradiated crystals were cleaned in chloroform and alcohol.

### 3.2.3 Energy Response

The energy dependence of lithium fluoride has been well studied up to  $\text{Co}^{60}$  energies (1.17 MeV and 1.33 MeV). The response per rad is constant down to approximately 100 KeV after which there is a significant increase [17, 18]. Several papers [19-22] discuss the energy dependence of lithium fluoride to high energy electrons. It was assumed in this work that the response in the energy region from  $\text{Co}^{60}$  up to the maximum gamma-ray energy of a fast reactor is constant. However, a recent paper by Liu and Bagne (page 937, Reference [15]) shows that the TL response is lower by approximately 5% relative to  $\text{Co}^{60}$  in this energy region.

### 3.2.4 Dose Response

Lithium fluoride TLD are dose-rate independent [23] but they are dose dependent. The non-linearity of the integrated light output with dose is shown in Figure 4, a typical dose response curve for TLD-700 crystals. Supralinearity begins at approximately 200 rad ( $\text{Li}^7\text{F}$ ), the response in this region being a function of gamma-ray energy. The post-irradiation annealing process used during this work, in order to utilise the crystals for several experiments, was one hour at  $400^\circ\text{C}$  followed by sixteen hours at  $80^\circ\text{C}$ . Annealing alters the dose response curve and therefore batch calibrations were essential after each experiment. Calibrations were carried out in a known  $\text{Co}^{60}$  radiation field, the length of the



TYPICAL Li<sup>7</sup>F (TLD-700) DOSE RESPONSE CURVE  
FIGURE 4



irradiation giving the desired dose. The TLD were surrounded by a lithium fluoride wall of equilibrium thickness during exposure.

As the ZEBRA core temperature was below 50°C there would be no change of response due to irradiation at an elevated temperature. In order to minimise corrections, reactor power and irradiation times were chosen to keep doses within the linear region of the response curve.

### 3.2.5 Fading of the Thermoluminescent Signal

Following irradiation there is a slow rate of loss of the stored energy ("fading" of the TL signal). There are several experimental [eg 24] and theoretical estimates [eg 25] of this rate of fading. For the present work the problem of uncertainties in the rate of fading was overcome by carrying out the readout process at a fixed time (seven days) after irradiation.

### 3.2.6 Neutron Sensitivity

There is evidence [26] that neutron exposure affects the photon response of  $\text{Li}^7\text{F}$ . More recent work [27, 28], however, shows that gamma-ray and neutron doses are additive. In TLD-700 the neutron reactions of importance are the  $\text{Li}^6(n,\alpha)t$  reaction and the elastic scattering of the Li and F nuclei. The contribution from the  $\text{Li}^6(n,\alpha)t$  reaction has been calculated assuming a 0.007%  $\text{Li}^6$  content and a 0.15 response [29] to alpha particles and tritons relative to  $\text{Co}^{60}$ . The dose-rate from thermal/epithermal neutron interactions was calculated to be  $1.75 \times 10^{-9} \phi \text{ rad sec}^{-1}$  where  $\phi$  is the neutron flux in  $\text{n.cm}^{-2} \text{ sec}^{-1}$ . The total energy deposited from this reaction was less than 0.1% in the ZEBRA MZB core and blanket regions, although this increased to about a percent in the

outer reflector.

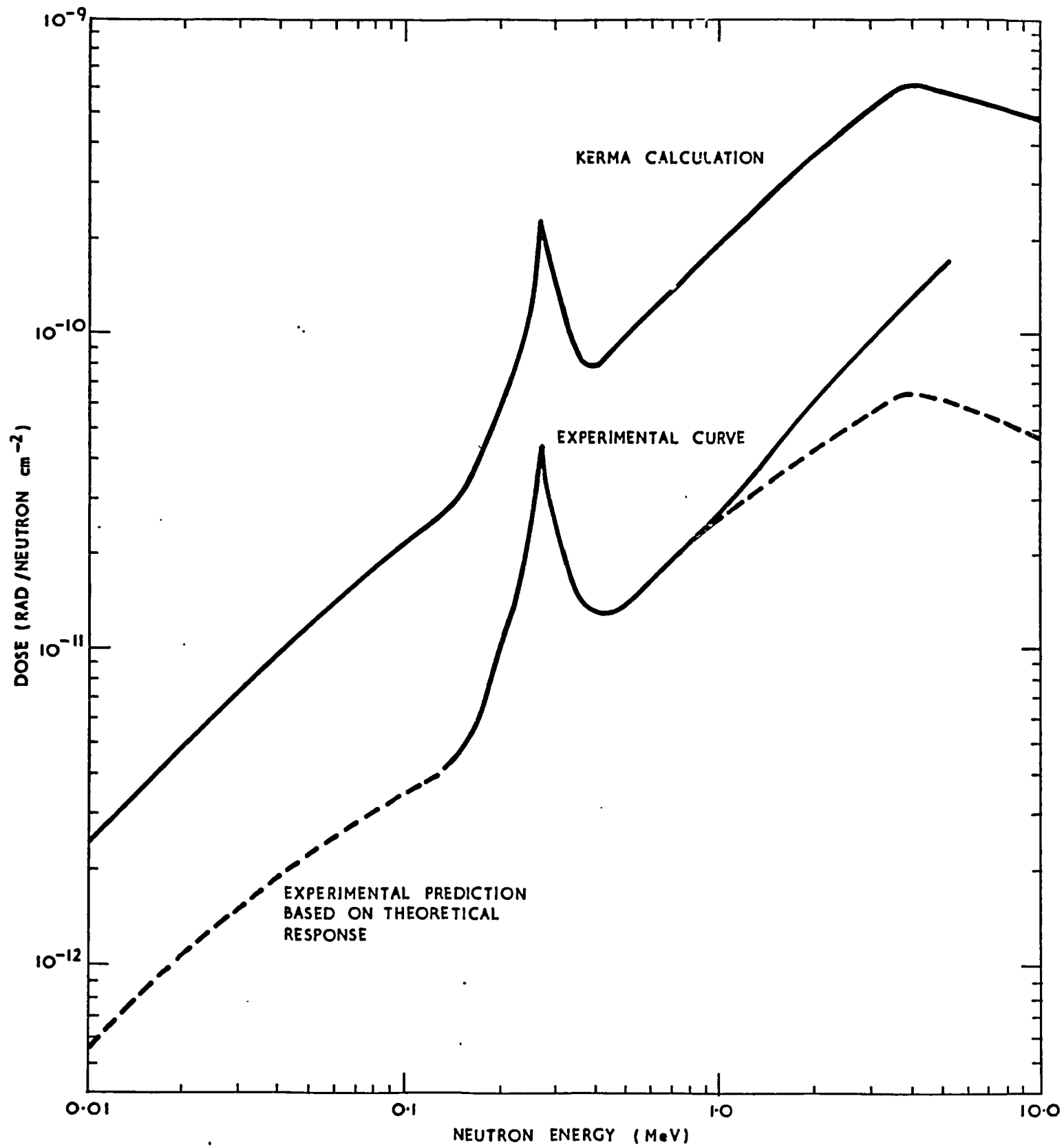
The major contribution to the TL signal was from the  $\text{Li}^7$  and F recoils and it was therefore necessary to know the sensitivity of the TLD to the recoil nuclei. The measured gamma-ray dose-rate in  $\text{rad hr}^{-1}$  (D) is related to the integrated light count ( $C_\gamma$ ) by  $D = C_\gamma/S_\gamma$  where  $S_\gamma$  is the crystal's photon sensitivity (counts per  $\text{rad hr}^{-1}$ ). Neutron dose-rates can be expressed in gamma equivalent  $\text{rad hr}^{-1}$  by applying the same sensitivity factor. For a measurement in a mixed gamma/neutron field the gamma dose-rate  $d_n$  is related to the measured dose-rate  $d_m$  by:

$$d_n = d_m - S_c N_c \quad - - - (10)$$

where  $N_c$  is the neutron recoil dose-rate in the TLD cavity and  $S_c$  is the relative sensitivity to the cavity recoils (ie  $S_c = S_{cr}/S_\gamma$  where  $S_{cr}$  is the sensitivity to the cavity recoils). The integrated light count due to neutron interactions  $C_n = S_{cr} N_c$ ,

$$d_n = \frac{C_\gamma + C_n}{S_\gamma} - \frac{S_{cr} N_c}{S_\gamma} \quad - - - (11)$$

The sensitivity to the recoil nuclei in TLD as a function of energy was obtained from a least-squares fit to the experimental data of Wingate et al [30] and Furuta and Tanaka [31]. As the energy range of the experimental data was limited, a theoretical sensitivity was calculated based on the assumption that the TL response to particles was a simple function of LET. From various stopping power tables  $\text{LET} = f(E_n)$  for  $\text{Li}^7$  and F recoils in  $\text{Li}^7\text{F}$  was obtained. Using the Two-Trap Theory curve of Jähner (page 1031, Reference [14])  $Q = g(\text{LET})$  was obtained (where  $Q$  is the response relative to  $\text{Co}^{60}$ ). Combining this data  $Q = g(f(E_n))$  was



THE NEUTRON SENSITIVITY OF Li<sup>7</sup>F (TLD-700)  
 FIGURE 5

obtained at the mid-energies of the 37 fast reactor group scheme. The kerma-rate in  $\text{Li}^7\text{F}$  for unit neutron fluence was also calculated at these energies as described in Appendix B (Equation B10). The product of the kerma values and the response values should result in the experimental data. It can be seen in Figure 5, where an "eye-guide" fit has been made through the calculated values (hence the absence of several peaks in the curve), that agreement is excellent up to 1 MeV, above which the calculated curve slowly departs from the experimental curve. Above 4 MeV, when scattering becomes non-isotropic in the centre-of-mass system, the calculated dose begins to decrease whereas the experimental curve continues to rise. It appears therefore that the response is not a simple function of LET. In the calculated of the neutron corrections to the MOZART measurements the theoretical response was used only where no experimental data was available. Further work on neutron responses has been carried out by Tanaka and Furuta and is reported in Volume 3 of Reference [15] and Reference [32].

### 3.2.7 The Cavity Correction

In order to measure the gamma-ray energy deposition in a medium it is necessary to probe the charged particle spectrum generated by the photon interactions. The "cavity" detecting medium, introduced as a probe into the "wall" medium, usually constitutes a discontinuity which affects the equilibrium particle spectrum. The relationship between the energy deposition in the cavity and the wall is a function of photon energy, cavity size, and the composition of the medium. The problem is the form of this relationship [3].

If the cavity size is small compared with the range of the particles generated in the wall, the energy deposition for a monoenergetic photon source is in the ratio of the mass stopping powers for the media (ie the Bragg-Gray equation discussed in 3.1.1). For a large cavity, where the range of particles is small compared with cavity dimensions, and the majority of the energy deposition is from photon interactions in the cavity itself, the energy deposition is now in the ratio of the mass energy absorption coefficients. With the intermediate case the energy absorbed in the cavity is from particles generated in both wall and cavity. T E Burlin [33] derived an expression for the situation where the cavity dimensions are comparable with the electron range. This was attained by combining the dose due to electrons produced within the cavity, and externally produced electrons, by means of a weighting factor which was a function of the maximum electron energy. It was assumed that the electron spectrum generated in the wall had the same maximum energy as that of the cavity. This would not be valid when the majority of interactions are photoelectric in a high-Z wall and Compton in the detecting medium. The method of calculating the weighting factor is based on evidence from experimental studies of  $\beta$ -rays and electron absorption. To a first approximation in a thin absorber, the electron spectrum is attenuated exponentially with no change in the spectral distribution. It is thus possible to define an effective electron mass absorption coefficient ( $\mu_e/\rho$ ) which is a function of the maximum energy. Several expressions for the effective electron mass absorption coefficient have been employed; the most common method being to relate it to an electron range ( $R_e$ ) corresponding to a fixed attenuation. Thus, for a

99% reduction in intensity:

$$\frac{\mu_e}{\rho} = \frac{-\ln 0.01}{R_e} \quad - - - (12)$$

Apart from the inherent difficulty in defining an electron range [34] it is necessary to rely on simplified empirical energy-range formulae such as those given by Katz and Penfold [35]. The restriction of a single effective mass absorption coefficient does not allow the use of more accurate expressions for electron range which are a function of energy, atomic number and atomic weight [36].

The shape of the external spectrum is assumed constant throughout the detecting medium but with its intensity decreasing exponentially with distance into the cavity. In order to reduce the problem to one-dimension Burlin averages the spectrum over the mean chord length across the cavity ( $q$ ); given by four times the cavity volume divided by the surface area. The weighting factor  $d$  is therefore the average intensity over the mean chord length.

$$d = \frac{\int_0^q e^{-\frac{\mu_e}{\rho}x} dx}{\int_0^q dx} = \frac{1 - e^{-\frac{\mu_e}{\rho}q}}{\frac{\mu_e}{\rho}q} \quad - - - (13)$$

During attenuation the external spectrum obviously changes in shape. For the situations studied by Burlin the deficiency in the highest energy electrons was compensated by the excess of these electrons in the cavity spectrum. This, however, will not be particularly effective for a high-Z wall around a low-Z cavity. The ratio of the energy deposited per unit mass in

the cavity ( $\epsilon_c$ ) to the energy deposited per unit mass in the wall ( $\epsilon_w$ ) is a combination of the "external contribution" and the "internal contribution":

$$\frac{\epsilon_c}{\epsilon_w} = d \frac{\left(\frac{S}{\rho}\right)_c}{\left(\frac{S}{\rho}\right)_w} + (1 - d) \frac{\left(\frac{\mu_{en}}{\rho}\right)_c}{\left(\frac{\mu_{en}}{\rho}\right)_w} \quad - - - (14)$$

An expression for the mass stopping power of an electron of initial energy  $T_m$  is given in Appendix C (equation C8). It is necessary to average this over the equilibrium spectrum resulting from the slowing down of electrons of the single energy, and then to average over the range of source electrons generated by a monoenergetic photon. For a spectrum of photon energies the cavity correction is usually a flux weighted value although the more correct averaging is given by equation (C39) in Appendix C. There have been experimental examinations of the theory [37, 38] and several workers have applied it to the analysis of TLD measurements in reactors [39, 40]. Although the Burlin theory had shown no serious defects in these studies the various assumptions and approximations require further investigation. For the ZEBRA type of work, where experiments are performed to check the accuracy of calculational techniques and data sets, the ideal approach would be to include charged particle tracking in the standard gamma-ray Monte Carlo programs. This would allow the accurate calculation of energy deposition close to material boundaries and in small regions where charged particle migration is significant. Photon-electron transport codes do exist [eg 41] but they are difficult to adapt for the efficient solving of the cavity problem. The approach adopted for the present work was to write a Monte Carlo electron tracking program, separate from the

standard gamma-ray codes, that would operate from calculated photon spectra. The program, PROCEED, is described in Appendix C. The basic concept of the program is the calculation of the energy deposited in the cavity whilst containing the wall medium ( $\epsilon_w$ ) and the energy deposited in the cavity whilst containing the detecting medium ( $\epsilon_c$ ). The resulting ratio ( $\epsilon_w/\epsilon_c$ ) gives the required cavity correction. Thus, the energy deposition in a material is calculated using standard methods and PROCEED relates this value to the experimental result. Results for monoenergetic sources are given in Appendix C for various materials of interest. Comparison of results with Burlin's theory and details of a benchmark experiment carried out to validate the TLD technique are described in the following section.

---



#### 4 THERMOLUMINESCENT DOSIMETER IRON BLOCK BENCHMARK

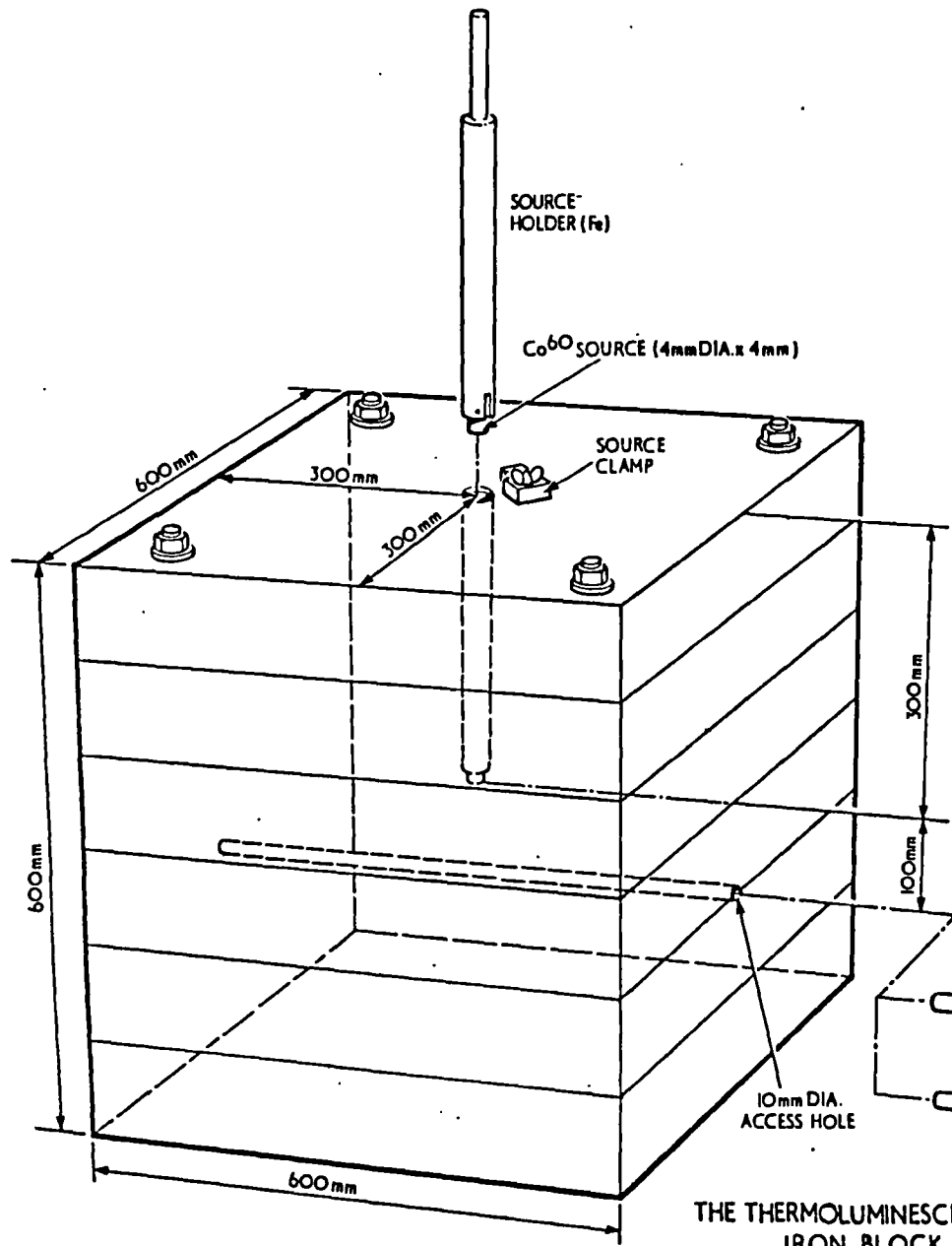
A benchmark experiment was designed to investigate the cavity correction in the absence of reactor environment complications. A  $\text{Co}^{60}$  source was housed in the centre of a large iron block and the energy deposition in TLD-700 crystals, surrounded by different materials, was obtained. Although this provided a well defined and reproducible environment, the shortcomings of gamma-ray computational methods made the calculation of energy deposition and spectra at the measurement positions in the seemingly simple geometry a difficult task.

##### 4.1 Description of the Experiment

The experimental arrangement is illustrated in Figure 6. A 22 Ci  $\text{Co}^{60}$  source (4 mm diameter x 4 mm) was sealed in the centre of an iron cube of side 600 mm. A 10 mm diameter access hole ran 100 mm below the source plane. The crystals were located in cavities within the various test materials (LiF, C, Fe,  $\text{Eu}_2\text{O}_3$ , Ta). Some of these wall materials were the actual control rods and structural test pins used for energy deposition measurements within the ZEBRA core. For comparison of wall materials the crystals were loaded directly below the source in holder A (Figure 6). To measure the attenuation in iron, several crystals were loaded along the access hole in an iron holder (B). An irradiation time of 30 minutes was chosen in order to restrict the TL light output to the linear region of the dose response curve and each experiment was repeated several times. The crystals were read out seven days after irradiation using the procedure described in subsection 3.2.2.

##### 4.2 The Benchmark Calculations

The uniform iron block was the simplest case to analyse and the calculations were carried out using the Monte Carlo program McGID [42].

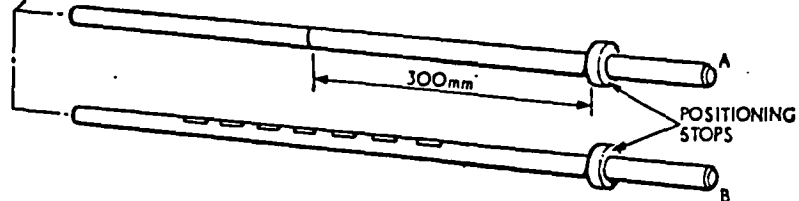


IRON BLOCK ASSAY:

MANGANESE	0.95%
SILICON	0.03%
PHOSPHORUS	0.01%
SULPHUR	0.02%
CARBON	0.1%

CRYSTAL HOLDERS (Fe)

- (A) THE CENTRE PORTION AROUND THE CAVITY CAN BE REPLACED BY LiF, C, T<sub>2</sub>, Eu<sub>2</sub>O<sub>3</sub>
- (B) CAVITIES AT 40mm INTERVALS



THE THERMOLUMINESCENT DOSIMETER  
IRON BLOCK BENCHMARK  
FIGURE 6

In RZ geometry the source was represented as a ring around the detector region. McGID obtained the photon interaction cross-section from a modified version of the HEITLER subroutine [43]. The energy deposition at the appropriate points was obtained by scoring interactions which took place in a 10 mm diameter region around the position of interest and the group fluxes were scored by using track length estimation over this region. Splitting and Russian roulette were employed for variance reduction and to obtain 6% standard deviation on the energy deposition required 130 minutes computing time. For the calculations involving the different materials around the region of interest the above methods of scoring were not suitable. This especially applied to the high-Z materials where the energy deposition at the centre of the cylinder would be appreciably different from the average value obtained by scoring over the 10 mm region.

A discrete ordinate calculation appeared to be the most suitable method for solving the problem. The first task was to generate multigroup cross-sections in the fine energy structure scheme needed to examine the subsequent electron migration effects. The Oak Ridge program MUG [44], which produces photon cross-sections in a form suitable for direct input into the discrete ordinate transport codes ANISN [45] and DOT [46], and the multigroup Monte Carlo code MORSE [47], was adapted to read point cross-section data from the UKAEA Nuclear Data Library. Several of the elements required were not contained in the existing library and so the opportunity was taken to update and extend the library for all elements up to atomic number 94 by interpolating the data of Hubbell [11]. Cross-sections for the photoelectric effect, Compton scattering, pair production, and the total cross-section are stored at 40 energy points in the range 0.01 MeV to 20 MeV. The

angular distribution for Compton scattering was also included in the library. The processing methods and cross-section data are described in Reference [48].

MUG was used to produce the necessary 27 group  $P_5$  multigroup cross-section sets. A DOT III calculation was performed with 21 radial intervals and 15 axial intervals, and a standard  $S_{10}$  symmetric angular quadrature set [49]. (However, an error was later discovered in the input data which caused the program to ignore the angular distribution data and treat the cross-section data as  $P_0$ .) The detector was represented by a cylinder on the Z-axis and the source was treated as an annular ring of small dimensions at a radius of 100 mm. Unfortunately, the geometry of this calculation - 2D with a small source, and small mesh intervals to represent the detector - provided an ideal demonstration of a main defect of discrete ordinate calculations - the "ray effect". In the discrete ordinate approximation the partial differential operator which gives a continuous angle variation is replaced with discrete angular variables. This results in discrete directions and it is therefore possible for particles emitted from an isotropic source to miss the region of interest. The effect was seen in the iron block calculation as an oscillation of the flux in the axial direction in each energy group. A minimum in the axial variation at the central region of interest where the fluxes should show maxima was due to the absence of the uncollided component. The use of an analytic first-collision source would have provided a solution to this problem but the routines available in DOT could not treat off-axis sources and material variations. Although it would have been possible to write a first-collision source routine for the benchmark geometry, this was considered at the time to involve too much extra

programming. A higher order of quadrature was another possible solution, but apart from the fact that sets are not readily available, the increase in computing cost would have been unacceptable (the original calculation required 330 K-bytes of store and 60 minutes computing time). The use of specially tailored quadrature sets appeared to be a promising compromise. Although a few asymmetric sets were available there was nothing suitable for this geometry. An initial attempt was made to combine two symmetric sets to produce an asymmetric set which was forward peaked in the radial direction and the  $90^\circ$  polar direction. This did not eliminate the ray-effect although it did succeed in predicting the maximum flux at the central region. Variations of mesh size, source size and detector size were tried. The difficulties in using DOT III for this problem were apparent when it was found that changes of quadrature set produced a wide range of answers. Avery [50] developed a set from first principles which was tailored for the specific spatial mesh of this problem. By choosing the polar angles to ensure that each axial mesh at the centre axis ( $R=0$ ) was intersected by one ray from the source, the ray-effect was eliminated and the axial shape appeared to be acceptable. However, examination of the angular currents in the results showed a marked asymmetry in the polar direction whereas the use of a reflecting boundary at the  $Z=0$  plane passing through the source and detector should ensure symmetric values. This problem appeared to be due to the extrapolation procedure for obtaining the currents at the faces of a phase space cell when these showed the rapid variation associated with a point source. The use of the discrete ordinate method for this problem was therefore abandoned.

In an attempt to produce answers within a reasonable time from a Monte

Carlo code the multigroup program MORSE with its point flux estimator was used. The combinatorial geometry version of the code allowed the geometry of the iron block experiment to be represented exactly. Initial calculations produced a high incidence of negative fluxes. The cause of the difficulty was traced to the use of the Legendre expansions to give the probability of scatter through a given angle to reach the dose point. Ranges of the scatter angle for which the probability is zero are poorly represented by the Legendre expansion and negative values occurred frequently. Figure 7 shows the probability of scattering from group 1 to group 10 (energy limits can be obtained from Figure 8), through an angle  $\theta$  whose cosine is  $u$  using the input Legendre coefficients as in MORSE.

$$P^{i-j}(u) = \frac{P_s^{i-j}}{4\pi} \left[ 1 + \sum_{l=1}^M (2l+1) f_l^{i-j} P_l(u) \right] \quad \text{--- (15)}$$

where  $M$  is the number of coefficients;

$P_s^{i-j}$  is the probability of scattering from group  $i$  to group  $j$ ;

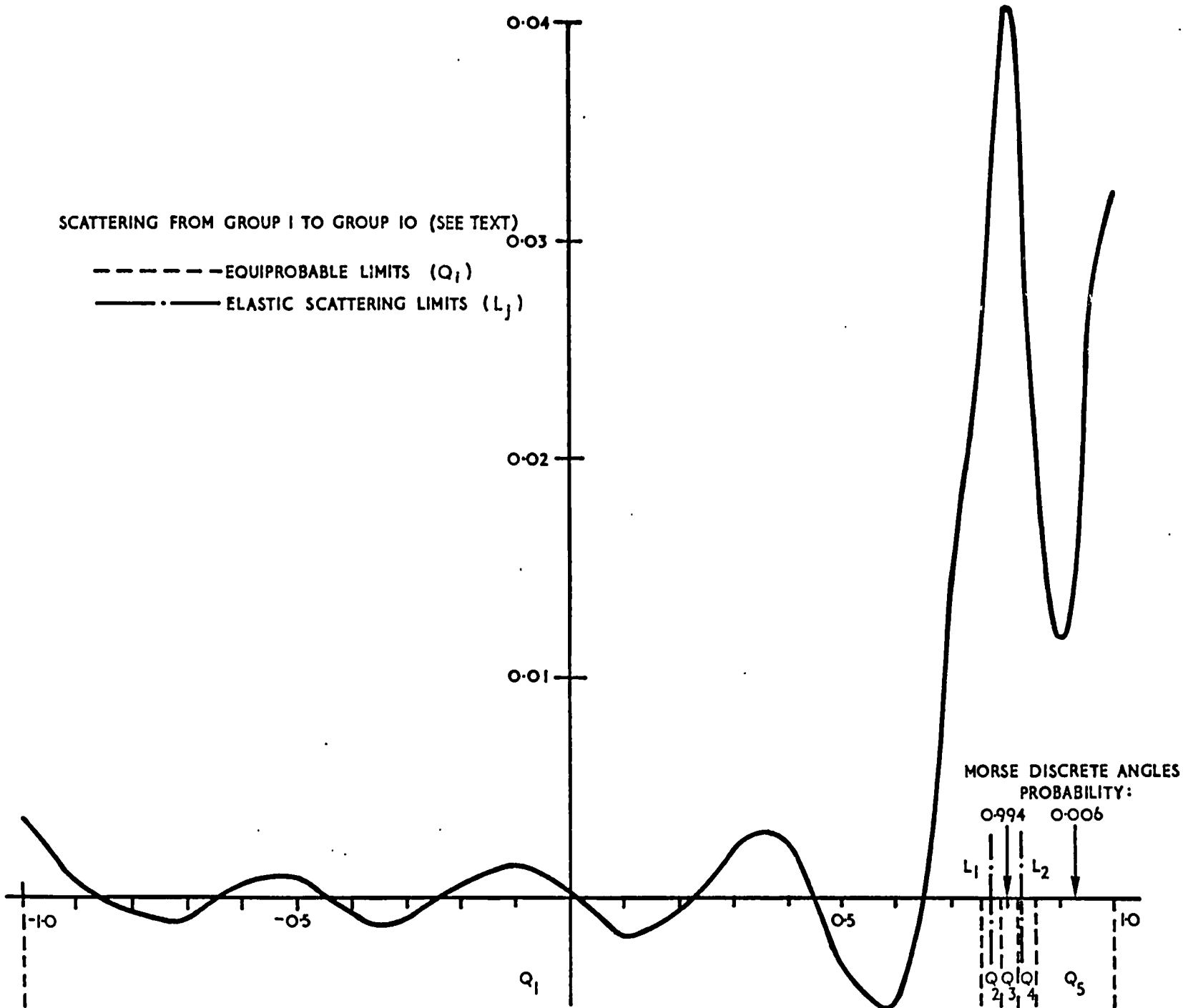
$f_l^{i-j}$  is the  $l$ th Legendre coefficient for scattering from group  $i$  to group  $j$ ;

$P_l(u)$  is the value of the  $l$ th Legendre polynomial for  $u$  calculated from the following recursion relation:

$$P_{l+1}(u) = (2l+1)u P_l(u) - lP_{l-1}(u)/l+1 \quad \text{--- (16)}$$

$$(P_0(u) = 1; \quad P_1(u) = u)$$

The majority of scatterings in the iron block calculation were due to Compton interactions and therefore for a given photon energy and angle of scatter it was a simple matter to calculate the probability per steradian of scattering using the Klein-Nishina formula. The angular distribution function per steradian of solid angle  $\Omega$  is given by:



EXAMPLE OF THE CALCULATED PROBABILITY OF SCATTER USING LEGENDRE EXPANSION  
FIGURE 7

$$\frac{d\sigma_{KN}(\theta)}{d\Omega} = \frac{1}{2} r_o^2 \left[ (1 + u^2) + \frac{E_{\gamma m}^2 (1-u)^2}{1 + E_{\gamma m} (1-u)} \right] / \left[ 1 + E_{\gamma m} (1-u) \right]^2 \frac{\text{cm}^2/\text{electron}}{\text{steradian}} \quad \text{--- (17)}$$

Integrating equation (17) over all angles gives the total Klein-Nishina collision cross-section:

$$\sigma_{KN} = 2\pi r_o^2 \left[ \frac{1 + E_{\gamma m}}{E_{\gamma m}^3} \left( \frac{2E_{\gamma m} (1 + E_{\gamma m})}{1 + 2E_{\gamma m}} - \ln(1 + 2E_{\gamma m}) \right) + \frac{\ln(1 + 2E_{\gamma m})}{2E_{\gamma m}} - \frac{1 + 3E_{\gamma m}}{(1 + 2E_{\gamma m})^2} \right] \frac{\text{cm}^2}{\text{electron}} \quad \text{--- (18)}$$

where  $E_{\gamma m}$  is the photon energy in  $m_o c^2$  units and  $r_o$  is the classical electron radius.

Hence, the probability that a photon of energy  $E_{\gamma}$  is scattered through an angle between  $\theta$  and  $\theta + d\theta$  is:

$$P(\theta, E_{\gamma}) = \frac{d\sigma_{KN}(\theta)}{d\Omega} / \sigma_{KN} \quad \text{--- (19)}$$

A special version of the MORSE subroutine PTHETA was written which ignored the multigroup parameters and calculated the probability using equation (17). The initialisation entry to PTHETA calculated the cross-sections for the mid-energy of each input group. Then for an incoming photon the mid-energy of the group was used to compute

$$\frac{d\sigma_{KN}(\theta)}{d\Omega} \text{ for the angle } \theta. \text{ The scattered photon energy } E_{\gamma}' \text{ is given by:}$$

$$E_{\gamma}' = \frac{E_{\gamma m} m_o c^2}{1 + E_{\gamma m} (1-u)} \text{ eV} \quad \text{--- (20)}$$

Thus, whereas the energy group probability table calculated using the Legendre coefficients contained small negative probabilities and gave scores in a number of final groups, the new version gave the actual probability of scattering into a single final group, with zero



probabilities in the remaining groups. The use of the mid-energy to represent the group introduced little error in this calculation.

The point-flux estimator in MORSE is known as the "next-event" estimator. This method scores, from each collision point, the probability of the next event being a distance  $r$  away at the detector point. The probability that a photon will travel a distance  $r$  without a collision is  $e^{-r/\lambda}$  where  $\lambda$  is the mean free path (reciprocal of the macroscopic cross-section). The uncollided flux from the source point to the detector is given by:

$$\Phi_{\text{uncol}} = \frac{w e^{-r/\lambda}}{4 \pi r^2} \quad - - - \quad (21)$$

where  $w$  is the weight of the source particle.

The flux estimate from each "real collision" (ie a collision which actually occurs during the particle's random walk) is given by:

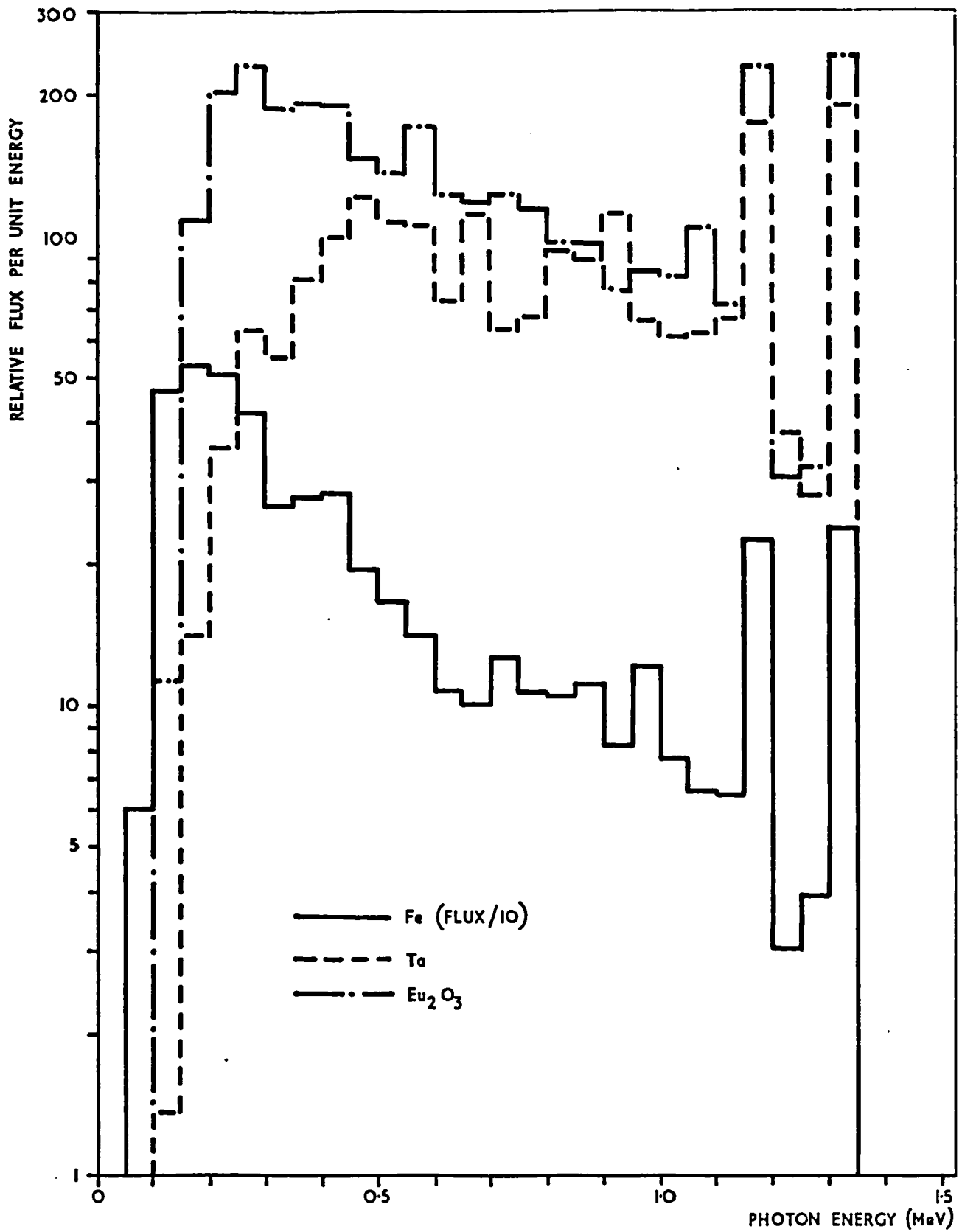
$$\Phi_{\text{col}} = \frac{w e^{-r/\lambda}}{r^2} P(\theta, E, \gamma) \quad - - - \quad (22)$$

where  $w$  is the weight of the particle adjusted at each collision by the non-absorption probability. The method of choosing the angle of scatter from the Legendre representation should be mentioned. Each group-to-group transfer has its own angular distribution. Numerically selecting from a distribution such as in Figure 7 produces cross-sections that will frequently be negative. Dividing the angular range into equiprobable angles ( $Q_1$  to  $Q_5$ ) would not satisfactorily represent the true distribution as shown in the figure, where equation (20) gives the actual limits of elastic scatter ( $L_1$  and  $L_2$ ). MORSE uses a scheme by which the Legendre coefficients for each group-to-group transfer are converted to angles, and probabilities of scattering at those angles, by the use of a generalised Gaussian quadrature using the angular

distribution as a weight function. The method is described fully in Reference [47]. By this scheme the maximum numbers of discrete angles chosen is half the number of coefficients (ie  $M/2$ ). For the example given in Figure 7 two angles were possible and these are given with their associated probability. Provided enough collisions occur the method should be quite satisfactory.

Each of the iron block calculations required approximately 90 minutes computing time to achieve 3% accuracy for the energy deposition. There is however one outstanding problem with the method used to obtain the flux at a point. Due to the  $1/r^2$  term an infinite variance, and therefore a slow convergence, was produced. The situation arose in the benchmark analysis during a run of 100,000 source particles for the Ta case when a single collision 0.66 mm from the detector more than doubled the total energy deposition at the point. The problem was overcome in these calculations by only applying the point flux estimator for collisions which took place at least 2 mm from the dose point. On the assumption that the flux was uniform within the 2 mm sphere, group-to-group transfer cross-sections were used with the group fluxes, calculated excluding this volume, to attain the neglected contribution. This method is not particularly satisfactory and in a new multigroup Monte Carlo program that is in the process of being written a finite variance method will be incorporated [eg 51].

The calculated spectra used as input data to PROCEED are given in Figure 8. Additional data were the cavity dimensions, material densities, atomic weights [11] and the average excitation-ionisation potentials [34, 39]. The correction for the polarisation of a medium by a charged particle (C 2.1.3 Appendix C) was not included in this work as its effect was considered negligible. The input data is given



PHOTON SPECTRA 100 mm FROM  $^{60}\text{Co}$  SOURCE IN THE IRON BLOCK BENCHMARK  
 FIGURE 8

in Table C4 of Appendix C along with that for other media. The photon interaction cross-sections were again obtained from the Hubbell data via the HEITLER subroutine.

#### 4.3 Discussion of Results

The results from the Iron Block Benchmark are summarised in Table 1. MORSE calculations were not carried out for the carbon wall situation or the iron attenuation experiments.

Table 1

Results from the Iron Block Benchmark

Wall	Experimental Result (rad hr <sup>-1</sup> )	PROCEED $\epsilon_w/\epsilon_c$	Corrected Expt. Result (rad hr <sup>-1</sup> )	MORSE Calculation (rad hr <sup>-1</sup> )	C/E
LiF	187.7 $\pm$ 0.7%	1.000	187.7	190.0 $\pm$ 3%	1.01
C	184.3 $\pm$ 0.7%	-	-	-	-
Fe	179.0 $\pm$ 1.0%	1.328 $\pm$ 2%	237.7	243.0 $\pm$ 3%	1.02
Ta	159.7 $\pm$ 0.5%	1.512 $\pm$ 2%	241.5	239.1 $\pm$ 3%	0.99
Eu <sub>2</sub> O <sub>3</sub>	203.0 $\pm$ 3.8%	1.708 $\pm$ 2%	346.7	349.0 $\pm$ 3%	1.01

The C/E values in Table 1 show excellent agreement between the PROCEED corrected measurements and the MORSE calculations. The McGID result for iron, obtained by scoring over a 10 mm cylinder, was 8.5% lower than that obtained by MORSE. This was, however, within the Monte Carlo statistics. Tanaka et al [32] have completed a similar iron benchmark. The value obtained using the one-dimensional option of the transport code PALLAS for iron, correcting for the different source strength, was 236.8 rad hr<sup>-1</sup>. It is concluded that the Iron Block Benchmark validates the TLD technique and the cavity Monte Carlo code PROCEED in the Co<sup>60</sup> spectrum energy range. However, there remain some aspects of the benchmark which require further investigation. The suitability of

the discrete ordinate code DOT and the evaluation of special quadrature sets requires further study. In addition, a reliable point-flux estimator must be devised for multigroup Monte Carlo codes.

As mentioned in the previous section, the cavity correction for monoenergetic sources in various materials has been calculated with PROCEED. There is little direct experimental evidence with which to compare results and usually insufficient detail to repeat calculations. Therefore most comparisons have been with predictions from Burlin's theory and, in general, agreement is excellent. For energies less than 50 KeV in high-Z materials where multiple scattering theory cannot predict the excessive scattering PROCEED assumes isotropic scattering and this introduces some uncertainty into results in this region. A significant discrepancy exists in the high energy region for low Z cavities surrounded by high-Z walls. Results from the Monte Carlo in this energy region in Ta are at least 20% greater than the values obtained from the Burlin theory. It appears that the Burlin weighting factor  $d$  biases the cavity correction to the small-cavity value at energies lower than that predicted by the Monte Carlo. Examination of the Monte Carlo predictions of a 5 MeV electron path showed it to be initially straight until it had lost approximately 70% of its energy. The angle of scattering then rapidly increased. If multiple scattering is neglected and particles are assumed not to deviate over their entire path length the PROCEED values agree with those from Burlin's theory. The Monte Carlo method employed by PROCEED should be the more rigorous approach to the cavity problem. Measurements are essential to establish the cavity correction in the high energy region where PROCEED does not corroborate the Burlin theory.

## 5 THE ZEBRA MEASUREMENT PROGRAM

The MZB and MZC assemblies in ZEBRA were part of a collaborative experimental program between the UKAEA and PNC of Japan related to the physics performance of large plutonium cores. This was of mutual interest to the PFR and CFR projects in the UK and the MONJU fast reactor prototype in Japan. The program was given the title MOZART (MOnju Zebra Assembly Reactor Test). The objectives and scope of the MOZART program are described in the Proceedings of the International Symposium on Physics of Fast Reactors, Tokyo, 1973 [4] and details of some experiments appear in subsequent papers.

The overall purpose of the Assembly 13 measurements was to test calculational methods, previously applied to relatively uniform core loadings, in more complex situations. The core was a close mock-up of the anticipated equilibrium configuration of the PFR with its numerous singularities such as part-inserted control rods, shut-off rod guide tubes and demountable sub-assemblies. From the point of view of gamma-ray energy deposition the discontinuities in materials required an accurate treatment of photon migration.

### 5.1 The ZEBRA Facility

ZEBRA (Zero Energy Breeder Reactor Assembly) is a versatile zero power facility for the physics study of plutonium-fuelled sodium-cooled fast reactors. Since first criticality in December 1962, experiments have been made on thirteen systems. These range from small test regions to investigate the accuracy of fundamental cross-section data, to full-scale mock-ups of the UK Prototype Fast Reactor (PFR) and the MONJU fast reactor prototype.

To obtain the required flexibility of core and blanket compositions the

assemblies are constructed from small plates of fast reactor constituents 51 mm square and of various thicknesses. The plates are stacked in stainless steel tubes and these elements are mounted vertically on a base plate. They are laterally supported by three lattice plates at different heights, each square accommodating 25 elements (5 x 5). Smaller size plates, 43 mm square, are used in nine moveable tubes which form the reactor control rods. The whole array makes a cubical assembly of side three metres.

## 5.2 The MZB Assembly

The MZB assembly was designed to provide the optimum representation of the clean MONJU reactor consistent with the various constraints imposed by the plate structure of the ZEBRA fuel. The inner core cell was constructed of plutonium metal and  $\text{PuO}_2/\text{UO}_2$ , together with  $\text{UO}_2$ , Na, and steel to obtain the required enrichment. The outer core cell contained plutonium metal,  $\text{UO}_2$ , Na, C, and steel plates, giving a total plutonium loading of 960 Kg (17%  $\text{Pu}^{240}$ , 3%  $\text{Pu}^{241}$ ). Because of inventory limitations it was not possible to mock-up the radial blanket exactly over the whole  $360^\circ$  and therefore a sector arrangement was chosen. The blanket over  $270^\circ$  remained in position throughout and contained cells constructed from natural U-metal, Na and C plates, the carbon content being chosen to simulate the oxide of the MONJU blanket. A closer representation was achieved in the  $90^\circ$  sector where three compositions were loaded in turn. The first (MZB(1)) contained natural  $\text{UO}_2$  and Na plates, the second (MZB(2)) depleted (0.2%)  $\text{UO}_2$  and Na plates, while the third (MZB(3)) had the same composition as the  $270^\circ$  sector. Beyond the  $90^\circ$  sector a steel region and graphite region were loaded; a graphite stack extending into the Shield Room facility of ZEBRA. This provided the boundary conditions for the breeder and radiation

penetration measurements. Figure 9 illustrates the core and breeder cell types, and Figure 10 and Figure 11 give the loadings and dimensions of MZB.

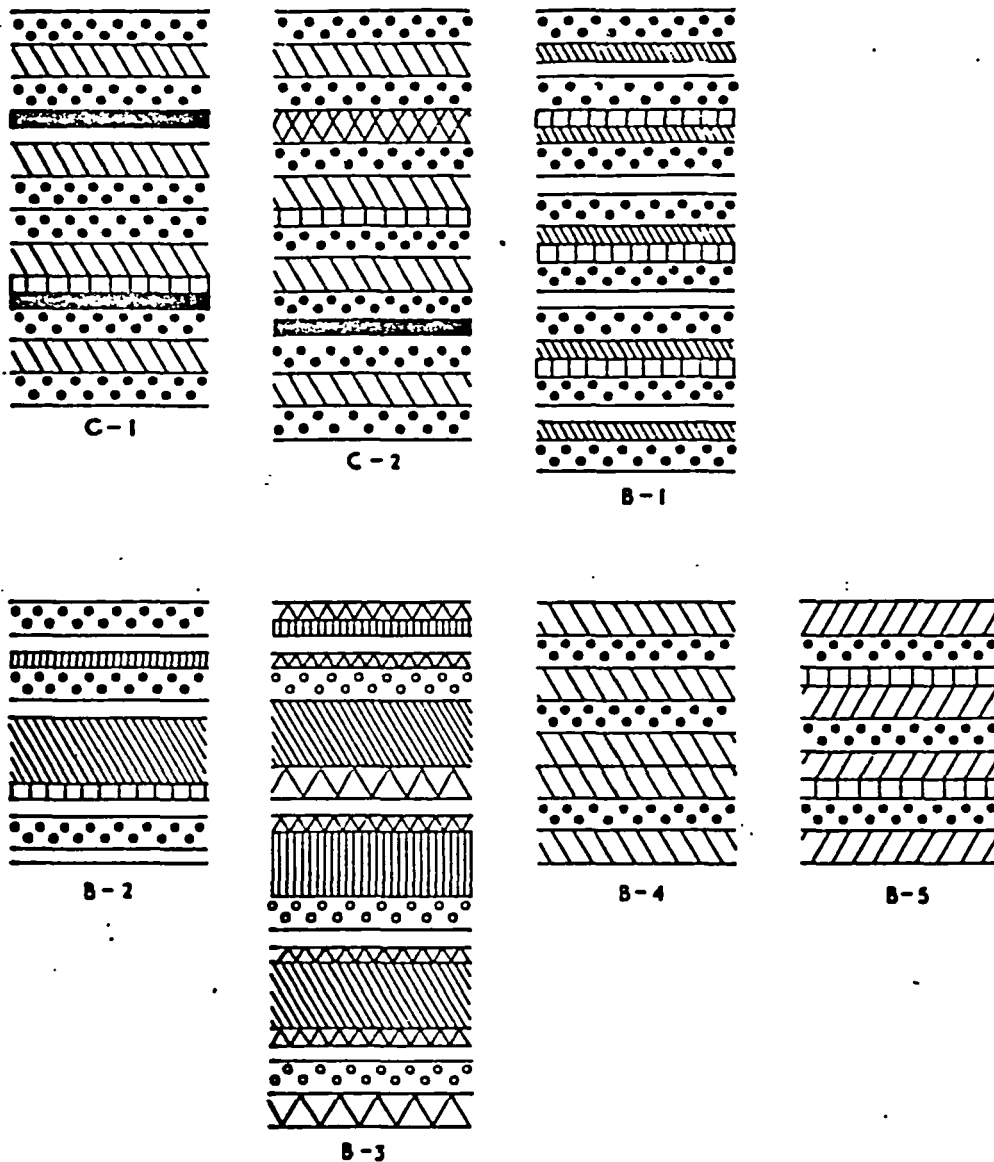
Table 2 summarises the gamma-ray energy deposition experiments made in the MZB assembly that are discussed in this thesis. There were twelve axial ionisation chamber scans and four SSCD scans made along the major axis. The element positions refer to Figure 10 and are given in the conventional x-y notation. Two radial scans were also made along the major axis using the SSCD.







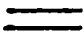




Table 2

The MZB Measurement Program

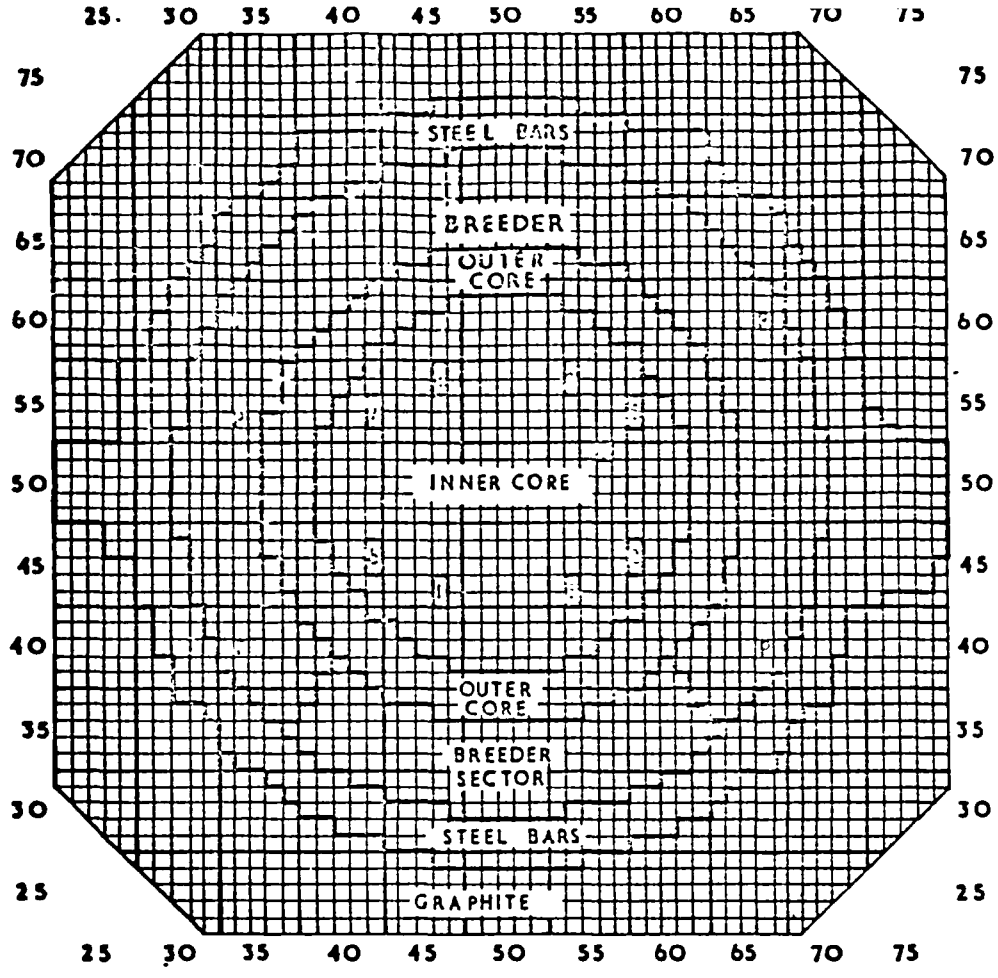
Scan Position	Radial Distance from Core Centre (mm)	Region	Measurement Technique	Ionisation Chamber Neutron Sensitivity Experiments on Centre Plane
Axial 50-50	0.0	Inner Core	ZrIG8/SSCD	CIG8 with 3 different gas fillings
Axial 50-48	107.4	Inner Core	ZrIG8	-
Axial 50-46	217.5	Inner Core	ZrIG8	-
Axial 50-44	325.0	Inner Core	ZrIG8	-
Axial 50-42	435.0	Inner Core	ZrIG8/SSCD	CIG8 with 3 different gas fillings
Axial 50-40	542.5	Inner Core	ZrIG8	-
Axial 50-37	706.3	Outer Core	ZrIG8/SSCD	-
Axial 50-35	813.7	Depleted	ZrIG8	-
Axial 50-32	977.5	UO <sub>2</sub> Breeder Depleted	ZrIG8/SSCD	CIG8 with 3 different gas fillings
Axial 50-32	977.5	UO <sub>2</sub> Breeder Natural	ZrIG8	-
Axial 50-68	977.5	UO <sub>2</sub> Breeder	ZrIG8	-
Axial 50-30	1085.0	Metal U Breeder Depleted	ZrIG8	-
Radial (Major axis)	-	UO <sub>2</sub> Breeder Through Depleted Sector	SSCD	-
Radial (Major axis)	-	Through Metal Sector	SSCD	-





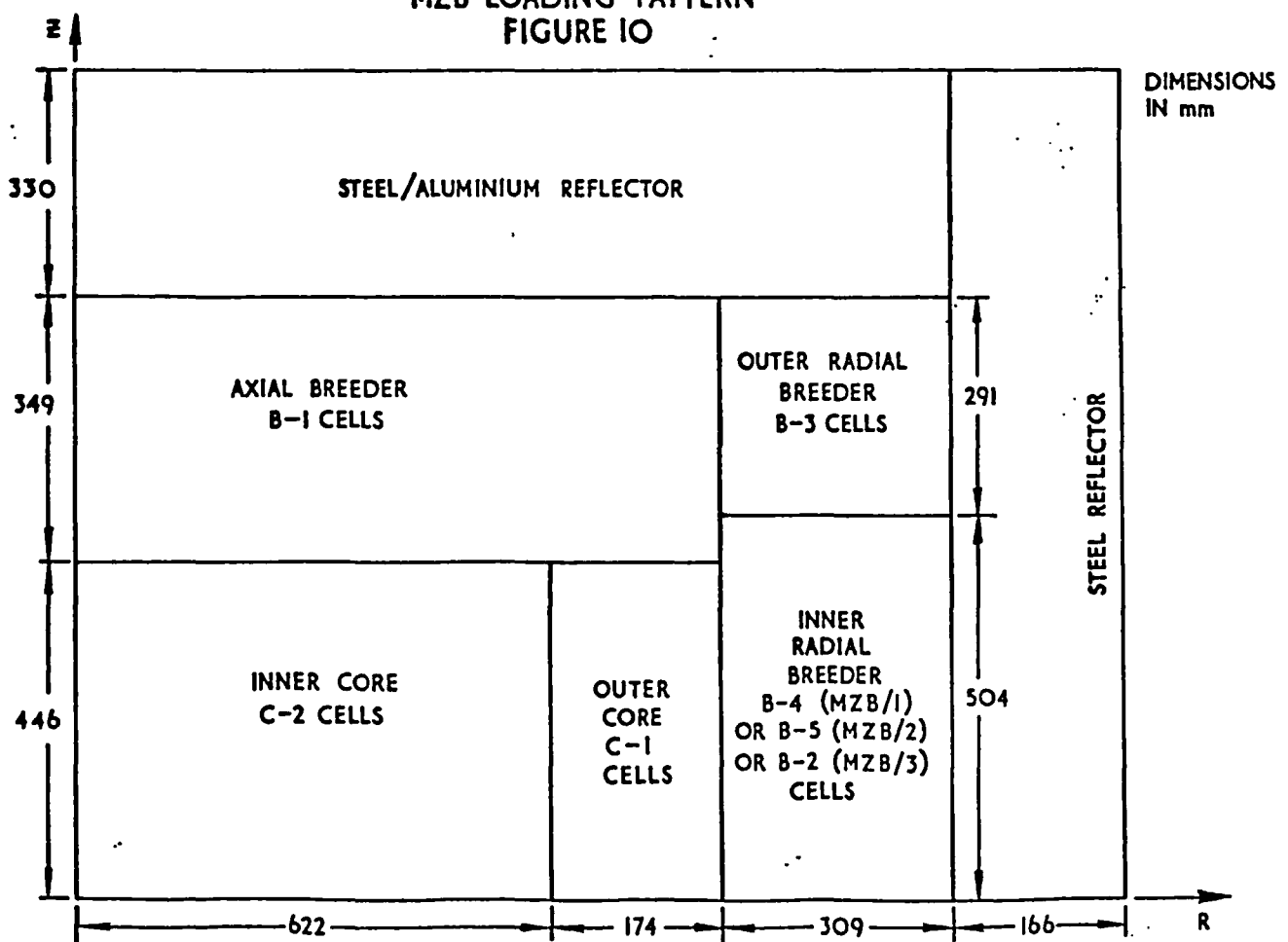
- |   |  |  |                           |
|---|--|--|---------------------------|
|  | STAINLESS STEEL CANNED SODIUM                        |  | URANIUM METAL (NATURAL)   |
|  | STAINLESS STEEL CANNED URANIUM OXIDE (NATURAL)       |  | MILD STEEL                |
|  | STAINLESS STEEL CANNED PLUTONIUM METAL               |  | ALUMINIUM                 |
|  | GRAPHITE   |  | ALUMINIUM OXIDE           |
|  | STAINLESS STEEL                                      |  | URANIUM OXIDE. (DEPLETED) |
|  | STAINLESS STEEL CANNED PLUTONIUM OXIDE/URANIUM OXIDE |  |                           |

CORE AND BREEDER CELL TYPES  
FIGURE 9



- P** PULSE COUNTERS
- N** CONTROL RODS (1-9)

MZB LOADING PATTERN  
FIGURE 10



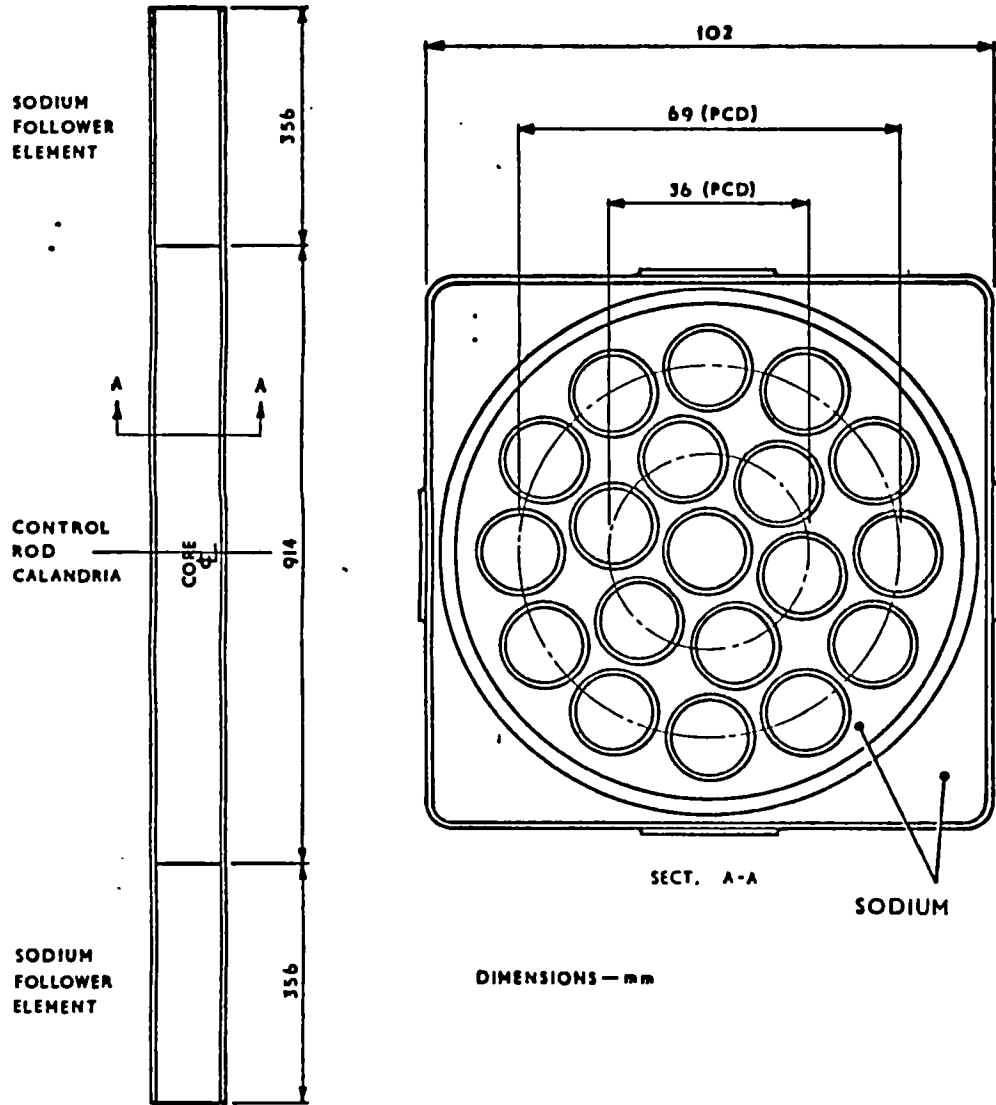
DIMENSIONS AND CELL LAYOUT OF MZB RZ MODEL  
FIGURE II

### 5.3 The MZC Assembly

The MZC program was comprised of experiments on a range of MONJU mock-up control rods installed in the MZB inner and outer core regions. The criticality of the assembly was maintained by the addition of fuel at the outer core/blanket boundary (Paper A17 [4]). The mock-up rods consisted of a 19 pin cluster of absorber pins contained in a sodium-filled stainless steel calandria, with follower elements also sodium-filled. Eight mock-up assemblies, each occupying a 2 x 2 array of ZEBRA elements, were constructed, comprised of four natural  $B_4C$ , and one each of 30%, 80%, 90% enriched  $B_4C$ , and a tantalum assembly. The basic dimensions of an assembly are given in Figure 12. Each  $B_4C$  pin consisted of 20 pellets of approximately 45 mm in length and 10.9 mm in diameter. These were contained in a stainless steel pin 11.1 mm inside diameter and 1 mm wall thickness. The tantalum pins had a diameter of 13.1 mm and were loaded directly into the calandria. Measurements of gamma-ray energy deposition within absorber pins were carried out with the natural  $B_4C$ , 80% enriched  $B_4C$  and Ta assembly in position 0 at the centre of the core (Figure 13), and with the Ta assembly at position S in the outer core. Axial and radial scans were made over the entire control rod mock-up with TLD, although the subsequent calculations were concerned only with the central rod centre-plane measurements because of the complicated geometry.

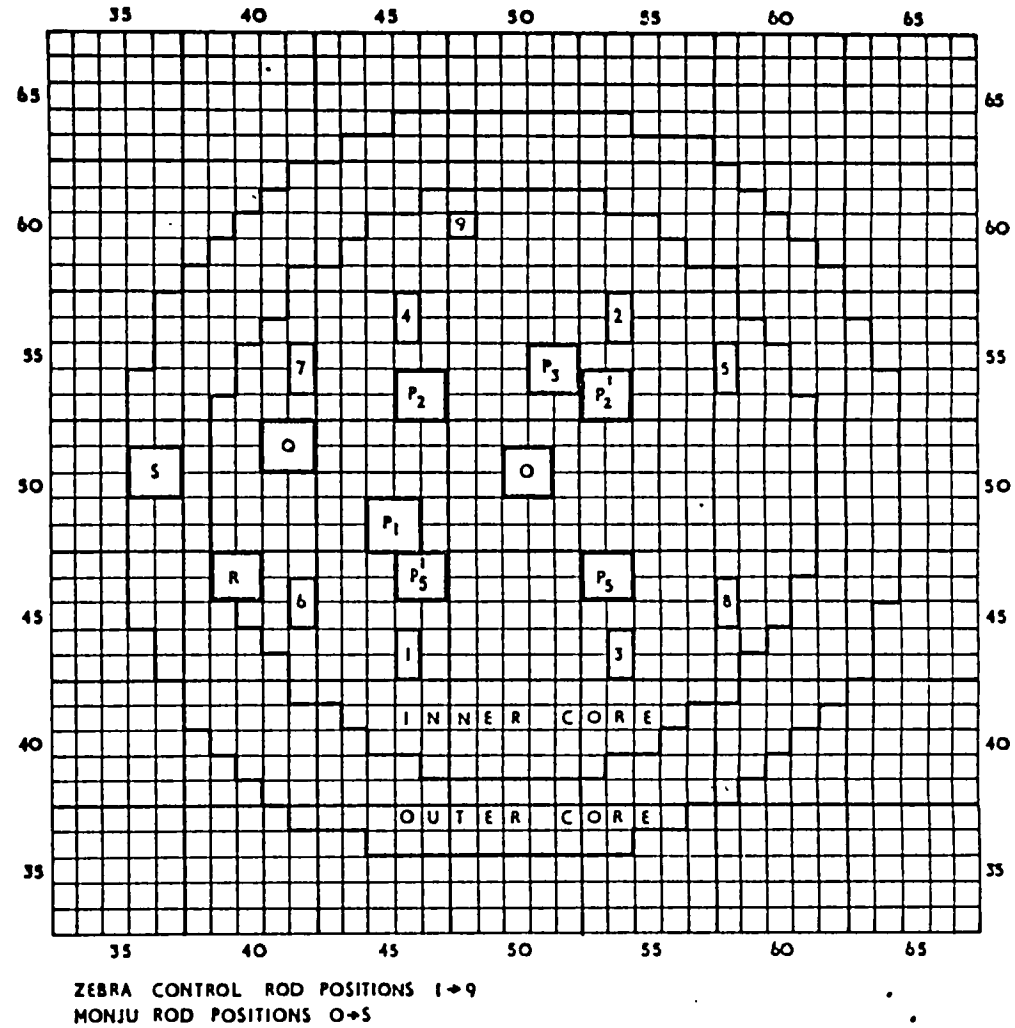
### 5.4 Assembly 13/3

The core 13/3 plan used during the gamma-ray measurements is shown in Figures 14 and 15. Five special control rod assemblies were placed in positions C1 to C5, corresponding to the control rod positions in PFR. The outer square sodium calandrias contained  $PuO_2/UO_2$  in the inner core region and  $UO_2$  pins in the outer core region. Inside a hexagonal



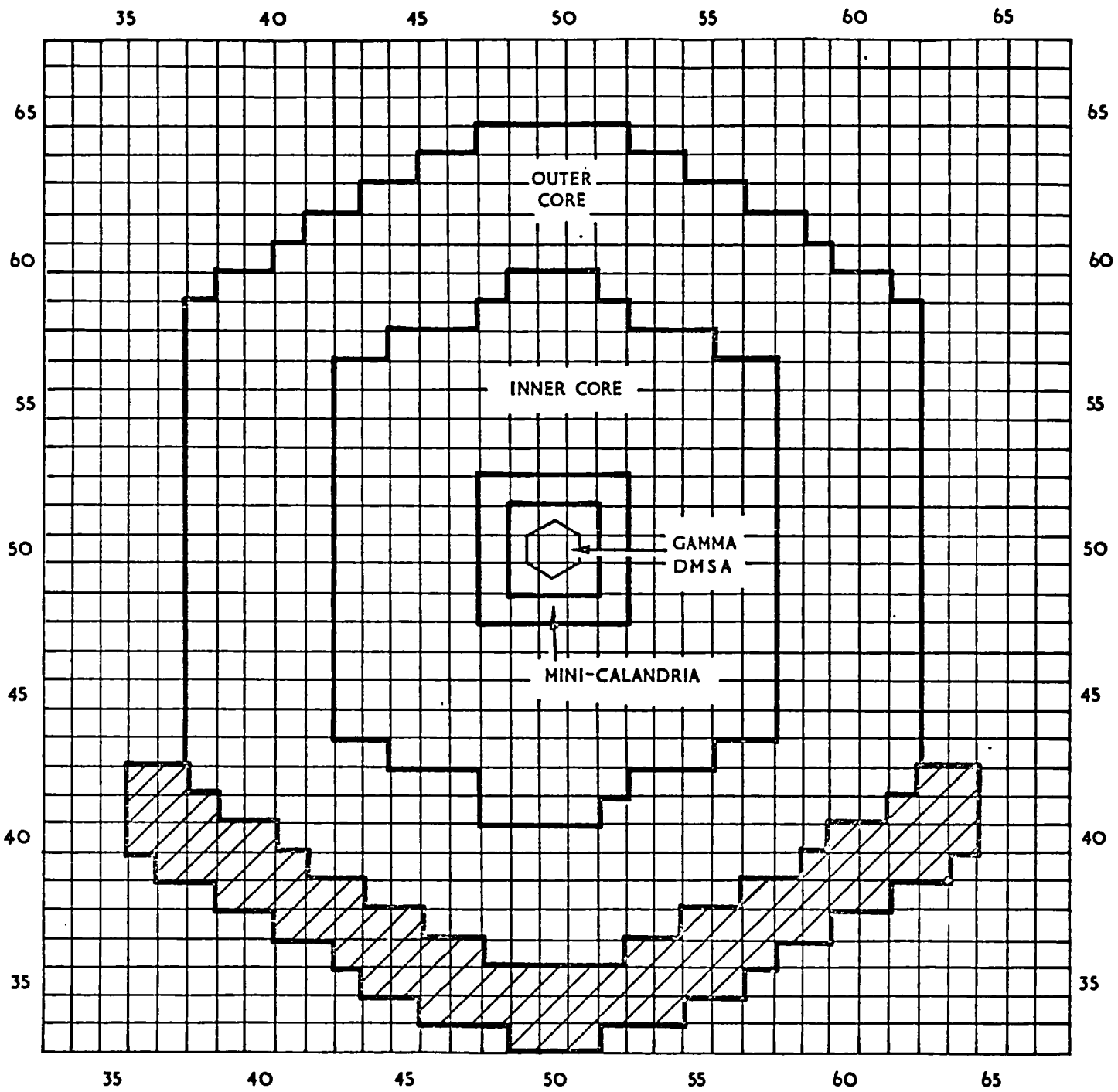
GENERAL ARRANGEMENT OF THE MONJU MOCK-UP CONTROL RODS

FIGURE 12



THE MZC MONJU MOCK-UP ROD POSITIONS

FIGURE 13

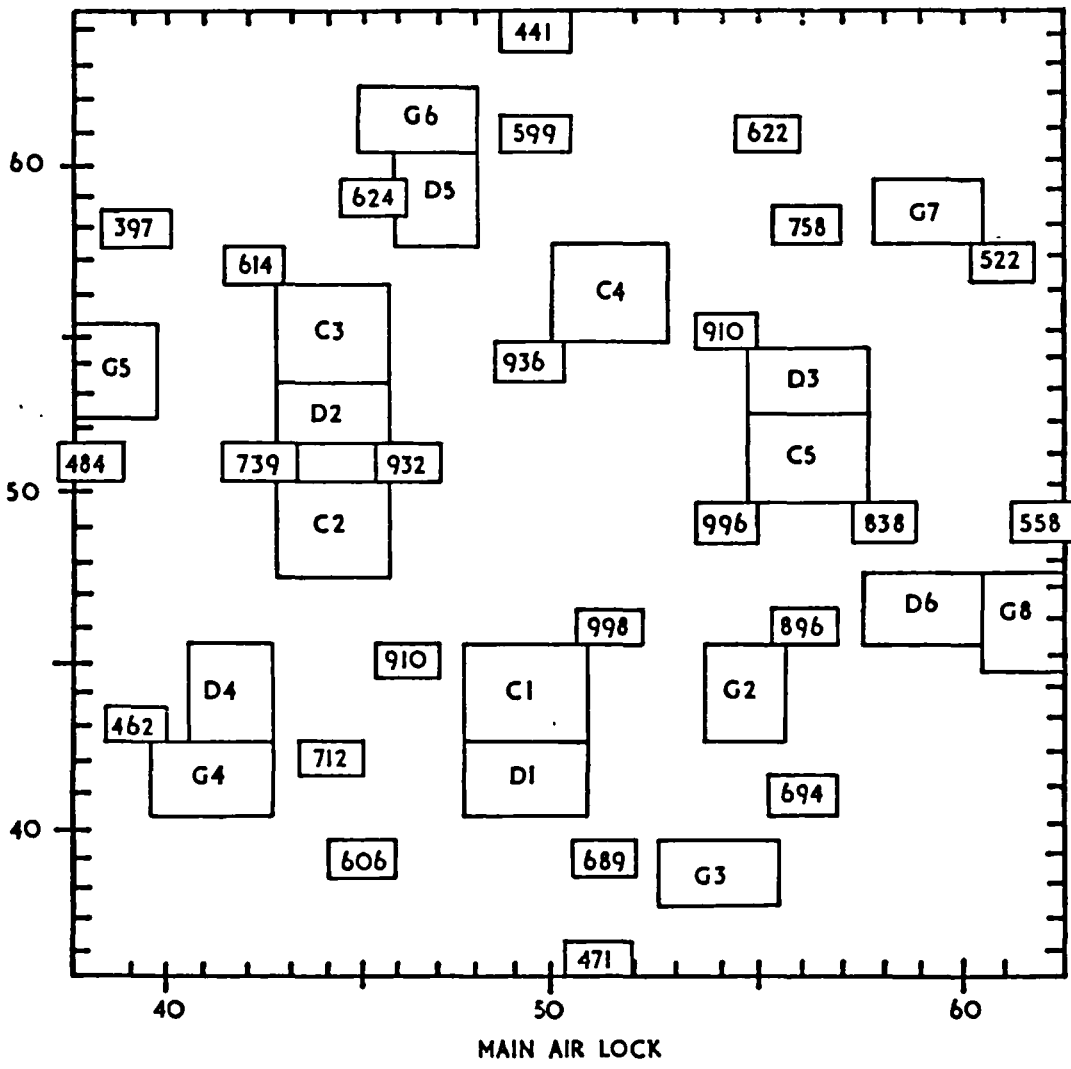


ASSEMBLY 13/3 CORE PLAN  
 FIGURE 14

CI-C5 CONTROL ROD ASSEMBLIES

DI-D6 DMSA

GI-G8 GUIDE TUBES



FOR ABSOLUTE  $\text{Pu}^{239}$  FISSION RATE SCALE BY  $7.80 \times 10^{-19}$

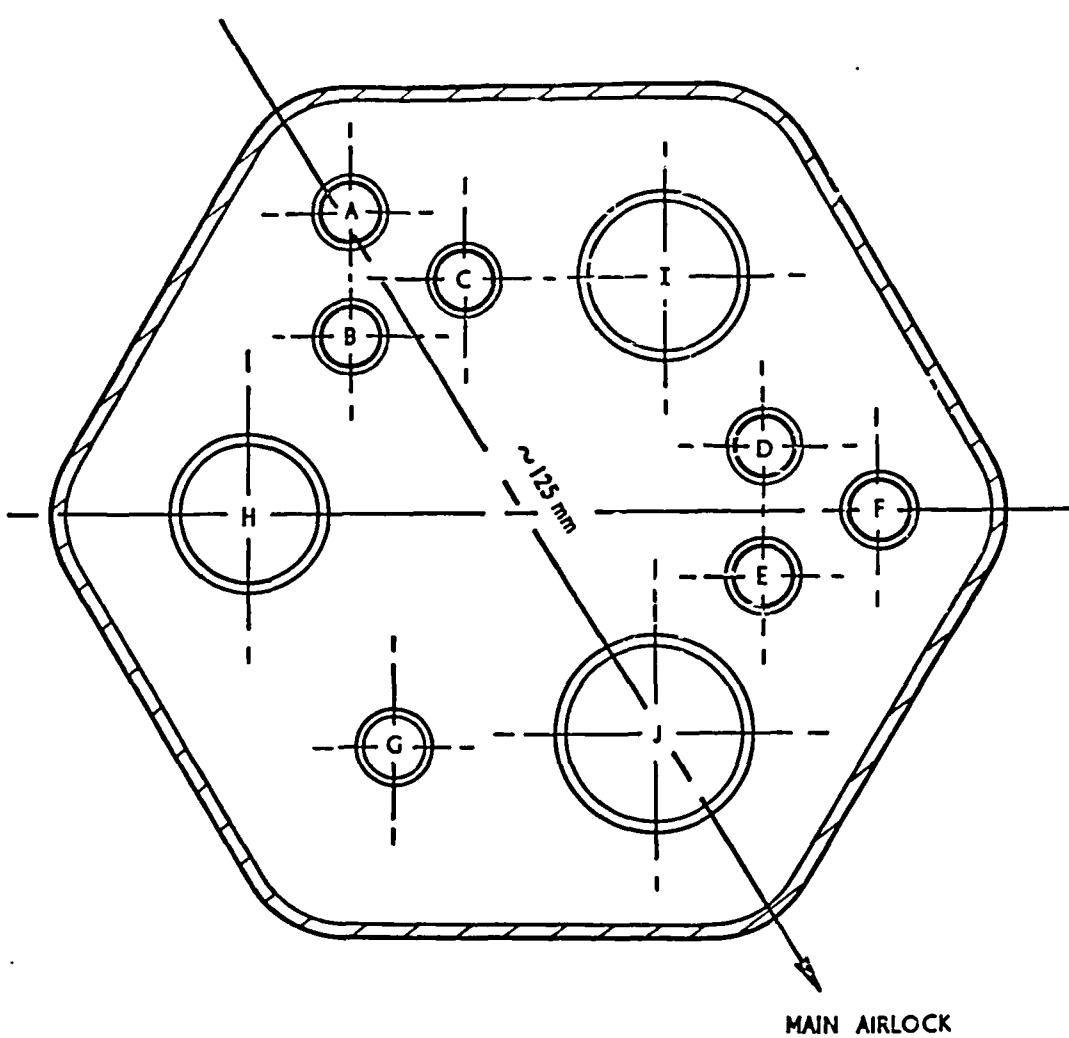
AN EXAMPLE OF RESULTS FROM THE ZEBRA MULTI-CHAMBER SCANNING SYSTEM IN ASSEMBLY 13/3

FIGURE 15

calandria were 19 natural boron carbide pins representing an absorbing control rod. This was approximately one third inserted into the core region, the remaining space being filled with hexagonal sodium-filled calandrias. Positions D1 to D6 are normal elements within the core filled with a lower density fuel representing demountable sub-assemblies (DMSA). Positions G1 to G8 represent guide tubes and were in fact normal ZEBRA elements filled with Na plates. Elements representing PFR radial oxide breeder sub-assemblies occupied a sector of approximately  $120^\circ$ , the remainder being made up with MZB natural metal blanket elements.

The gamma-ray energy deposition experiments consisted of scans within a single element using TLD in both oxide and metal breeders, TLD/chamber measurements in a 3 x 2 element PFR oxide breeder sub-assembly at the core centre, and TLD/chamber measurements within a special gamma-ray energy deposition demountable sub-assembly (gamma DMSA). The DMSA contained C,  $\text{Eu}_2\text{O}_3$ ,  $\text{B}_4\text{C}$ , Ta and stainless steel absorber pins of demountable construction. The location of the pins within the hexagonal DMSA is shown in Figure 16.

The gamma DMSA was located at the centre of a calandria which occupied 3 x 3 ZEBRA elements as illustrated in Figure 17. The region around the DMSA contained pin type fuel and when situated at the core centre the pin fuel region was extended to give a 5 x 5 array with mini-calandria in order to simplify subsequent analysis. Various combinations of the absorber pins were possible and two patterns (A and B) were chosen for the experiments. These are given in Tables 13 and 14, although the  $\text{Eu}_2\text{O}_3$  pins in positions D, E and F have been omitted for reasons explained in sub-section 5.5.3.



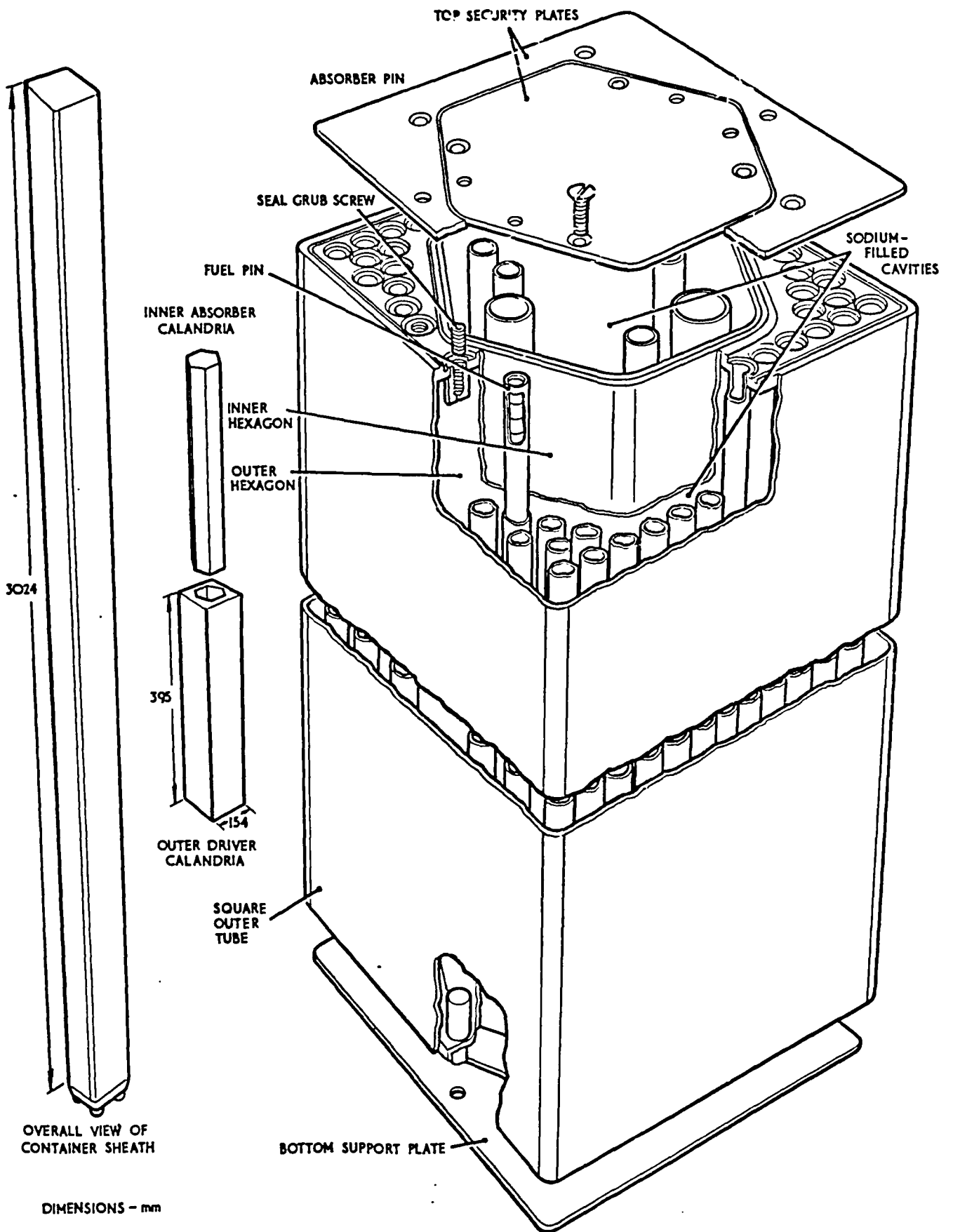
SCALE: FULL SIZE

PIN LOCATIONS:

- A,B,C CARBON
- D,E,F EUROPIUM OXIDE
- G STAINLESS STEEL
- H STAINLESS STEEL / TANTALUM
- I TANTALUM / BORON CARBIDE
- J CARBON / IONISATION CHAMBER

THE GAMMA - RAY ENERGY DEPOSITION DMSA  
FIGURE 16





PIN FUELLED CALANDRIA CONTAINING THE GAMMA DMSA  
 FIGURE 17 - 56 -

## 5.5 Experimental Methods Within ZEBRA

### 5.5.1 Access to Measurement Positions for the Ionisation Chambers

Axial scans were made in the normal ZEBRA elements constructed with plates containing a 23.6 mm diameter hole. The unlined access hole extended from a special aluminium plug, which secured an aluminium guide tube, through to the top shield doors, to approximately two cells below the centre plane. Slight modifications in the cell construction of these elements were necessary due to the availability of plates with holes. To locate the ionisation chamber during a scan it was secured to a calibrated aluminium tube which extended up through the guide tube. The calibrated tube, with chamber attached, could be lowered and raised within the core, a split collar at the mouth of the guide tube clamping it into position for each measurement. The calibrations were at 2 mm intervals and a datum was obtained by lowering the chamber until it rested on the solid plates. The cable from the chamber came through the calibrated tube mouth to the electrometer which was usually positioned at the edge of the top shield doors.

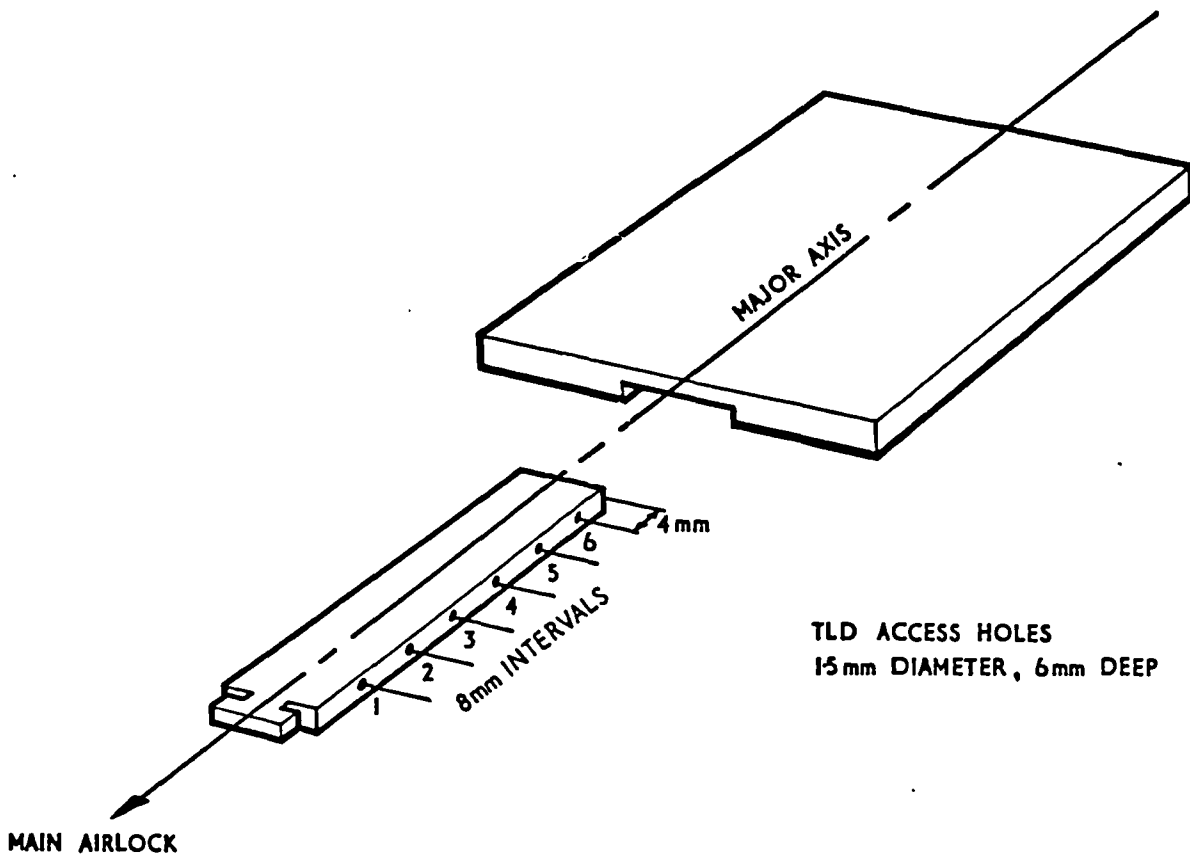
### 5.5.2 Access to Measurement Positions for the Thermoluminescent Dosimeters

A method of dose-mapping ZEBRA while at power was required, if possible utilising the ionisation chamber access holes for comparative measurements with the zirconium-walled chamber. A Solid State Cavity Dosimeter (SSCD) was devised capable of making an axial or radial scan during a single 15 minute irradiation. The SSCD consisted essentially of a zirconium rod, 8.9 mm diameter and 1.2 metres in length, with twenty 1 mm x 1 mm x 6 mm cavities at 50 mm intervals down the longitudinal axis of the rod ("major scan"

cavities). A further twelve "minor scan" cavities, identical with above, were equally spaced between the first and third major scan cavities. The calibrated tube used in the ionisation chamber measurements was adapted to lower the SSCD into the reactor. The radial scans were made in a 10.9 mm diameter stainless steel tube that went along the major axis on the core centre plane. A PTFE cable was used to drive manually the SSCD into the core. The cable was part of the ZEBRA automatic flux scanning system (Paper A16 [4]) and this equipment was adapted to position accurately the SSCD.

During the Assembly 13/3 program TLD were incorporated within elements with the object of accurately mapping the rapid dose change in the breeder region. A special stainless steel plate, containing a drawer with access for six TLD (Figure 18) was located between two 3.2 mm thick stainless steel plates near the core centre plane. A slight modification in cell construction was usually required to accommodate these plates.

Several methods of access were tried for the TLD measurement of energy deposition within pins. For the MZC Ta experiments the TLD were loaded into radial holes (1.5 mm diameter) down the length of the pins, Ta screw plugs keeping the crystals in position. This procedure was not particularly satisfactory because of the difficulties in loading and unloading, and resulted in many damaged crystals. In the MZC  $B_4C$  situation the TLD were loaded in an axial hole of 4 mm diameter in the centre pellet of the stack. In this case the crystals were grouped together, four in the natural  $B_4C$  and two in



**ZEBRA ELEMENT DRAWER ARRANGEMENT  
FIGURE 18**

the enriched  $B_4C$ , and surrounded by aluminium foil in order to shield them from alpha-particles and recoil atoms. Within the program of irradiations it was not possible to repeat these experiments and grouping TLD in this way provided a check on the crystals. The most effective procedure, for the care of crystals and simplicity of loading, was axial holes 1.5 mm in diameter and 6 mm deep in demountable pins. This was the method adopted for the Assembly 13/3 DMSA experiments, the size of the pellets chosen determining the axial positions of the TLD.

### 5.5.3 Reactor Environment Considerations

Several preliminary experiments were performed in ZEBRA to

investigate possible sources of measurement error. To ensure that the chamber wall thickness was adequate for the high energy gamma-rays produced in ZEBRA, experiments were carried out at an inner core position. Additional wall material around the chamber demonstrated that the IG8 chamber wall was suitable. The streaming of particles in the experimental access holes is often a problem in this type of measurement. In this work, however, no measured change in current was found when the depth of the access holes was varied. A final consideration was the possible activation of the materials comprising the chamber. The materials used in the construction of the IG8 chambers (graphite, zirconium, aluminium, magnesium) were chosen for their low neutron cross-section. To ensure that activation was not contributing to the measured signal the current was measured before positioning the chamber in the reactor and again immediately on removal after a long irradiation period. No significant change could be found although the outer aluminium case was emitting approximately  $200 \text{ mR hr}^{-1}$ , which decayed to  $10 \text{ mR hr}^{-1}$  within 15 minutes (measured with Type 1349 AEA Beta-Gamma Monitor, window open). Activation of the media surrounding TLD can cause considerable difficulties. The results from TLD within  $\text{Eu}_2\text{O}_3$  pins during the gamma DMSA Pattern B run were not consistent amongst themselves and were up to 20% greater than the first experimental run. This was probably due to the  $\text{Eu}_2\text{O}_3$  pellets being reloaded at various times after the first run, making the activation contribution vary between the TLD in the Pattern B run. It was not possible to eliminate the contribution to the measured signal from wall and cavity recoil nuclei for the IG8 chambers and TLD. The method of correction is discussed in Appendix B and 6.3.4.

From the initial start-up of a reactor there is a build-up of fission product activity which tends to a saturation value. If measurements of gamma-ray dose-rates are made only a few hours after start-up it is necessary to make a correction for the non-saturation of fission product photons. In experiments where the TLD are loaded into the core before start-up and unloaded after shut-down it was also necessary to make corrections for any contribution during these periods. These are necessarily calculated corrections because although the build-up to the time of measurements can be monitored, extrapolation to a saturation value is difficult. The calculation of this correction is described in sub-section 6.3. The ionisation chamber measurements were all carried out at full power in order to give the largest possible chamber current. The SSCD measurements were also made at full power to give a direct comparison with the chamber results. A 15 minute irradiation gave the TLD a sufficiently large dose yet kept the light counts in the linear region of the calibration curve. The MZC and Core 13/3 assemblies required that the TLD were loaded before reactor start-up. Therefore irradiations were carried out at a low power (usually 10% FP) in order to give a long irradiation time compared with the build-up time to power and post shut-down irradiation. Due to the plate construction of ZEBRA there is a "fine-structure" effect which can be seen for example in Figure 24. This made it essential for measurements to be taken at close intervals. The "pitch" of the fine structure is one cell length, the maxima occurring at the high photon source plates.

As already described, the  $B_4C$  crystals in the MZC experiments were surrounded by aluminium foil to shield from alpha-particles

and recoil atoms. It was not possible in the MZC program to repeat the experiment without the shield in order to check its effect. In the DMSA  $B_4C$  rod measurements the TLD were surrounded by a thin stainless steel wall and it was found that the energy deposition measured did not increase when the shield was removed. This was attributed partly to the low sensitivity of  $Li^7F$  to alpha-particles and wall recoils (less than 0.15 relative to  $Co^{60}$  gamma-rays for alpha-particles, probably less for the wall (B,C) recoils) and partly to the enhancement effect of the shield material.

In support of all the gamma-ray energy deposition measurements it was essential to make accurate neutron reaction-rate measurements and this was done by a combination of fission chamber and foil measurements. During the 13/3 core experiments the ZEBRA multichamber scanning system [52] was operational. This consisted of parallel-plate fission chambers of the same square geometry as the ZEBRA fuel plates incorporated within the fuel elements themselves. 150 chambers were distributed over the assembly, with an average plutonium-239 content of  $148 \mu g$ . Plutonium-239 foils were incorporated around the DMSA to give local power distributions. In addition, various foils such as  $Eu^{151}(n,\gamma)Eu^{152m}$  and  $Ta^{181}(n,\gamma)Ta^{182}$  were located within selected absorber pins of the DMSA and fuelled regions. The absolute fission-rates provided a comprehensive range of measurements with which to normalise the neutron flux calculations and check computed capture-rates. An example of results from the multichamber scanning system is given in Figure 15 (page 53) for the centre plane fission-rates during the DMSA Pattern A experiment.

## 6 THE ZEBRA CALCULATIONS

### 6.1 The MZB Assembly Calculations

Monte Carlo calculations were carried out to predict the flux spectra and dose-rate along the mid-plane major axis and the central vertical axis in the MZB(2) assembly. The radial calculations are described in some detail in this section to demonstrate the derivation of sources and their relative importance; although both sets of results are compared with the measurements.

The calculations were performed with the McGID program [42] in one-dimensional plane geometry. The program has access to a library of photon interaction data prepared from the UK Nuclear Data Library.

#### 6.1.1 Geometry and Materials

The co-ordinates of the plane region boundaries coincided with those of the radial boundaries used in the core calculation performed in RZ geometry with the diffusion theory program GOG (Paper A15, [4]). The RZ calculations were used in preference to the XY calculations in order to be consistent with the equivalent neutron calculations. A comparison of the two geometries showed that the maximum uncertainty in the gamma-ray sources due to the geometrical representation of the GOG calculations was approximately 5%. However, the comparison with experiments showed no evidence that the RZ geometry representation performed significantly worse overall. Details of the boundaries and compositions of regions are set out in Table 3. Smeared compositions for each cell type were used and it was necessary to average slightly different cell types in the inner and outer core regions. However, the neutron reaction-rates from which the gamma-ray sources were



Table 3

Region Compositions for the MZB(2) Assembly

	Inner core	Outer core	Breeder	Steel region	Graphite region	Spacer	Graphite stack
Outer boundary (mm)	622.06	796.43	1105.76	1271.30	1488.33	1495.79	1825.99
Density (g cm <sup>-3</sup> )	5.1744	5.2138	6.121	6.706	1.812	0.43	1.670
Proportion by nuclei							
H		.004815					.011787
C	.002264	.064369	.001598	.008285	.944364		.988213
O	.264120	.222311	.378582				
Na	.190426	.176998	.116785				
Al	.000573	.000535	.000264			1.0	
Si	.004215	.003988	.003190	.003744	.000195		
P				.000516			
S				.000446			
Ca	.000030	.000024					
Ti	.000552	.000547	.000445				
V	.000104	.000102					
Cr	.073495	.069714	.045603				
Mn	.005403	.005419	.003370	.008565	.000033		
Fe	.259391	.252254	.238636	.978444	.055407		
Ni	.038768	.035168	.021961				
Cu	.004907	.011162	.000112				
Ga	.000992	.002039					
Nb	.000546	.000424	.000118				
Mo	.000237	.000236	.000148				
Ag		.001418					
U	.125607	.111068	.188976				
Pu	.028345	.037407					

derived were obtained using the number densities appropriate to the local cell type. The outer boundary of the graphite region was chosen to give the correct thickness along the major radius and the void region was inserted to adjust the co-ordinates in the outer region to coincide with those of the physical system. The initial boundary was a reflecting boundary to ensure symmetry about the core centre. A black boundary condition was imposed after a region representing the first 330 mm of the graphite stack.

### 6.1.2 Sources

The McGID program can sample from only one source energy spectrum during a run. It was therefore necessary to divide the source into components for which the spectrum could be assumed constant throughout the source region, and to perform a separate calculation for each component. Such a division was also desirable so that the relative importance of the various sources could be assessed. The 13 energy groups in which the source spectra were expressed are those used by Sidebotham [53] and are given in Table 5. Gamma-ray flux spectra were calculated in 15 groups, which were constructed by adding two extra boundaries at 0.1 MeV and 0.2 MeV to those of the source group scheme. The calculation of the sources from the nine neutron reactions selected are now discussed.

#### (i) Fission in Plutonium and Uranium

Both prompt gamma-rays and those produced by the decay of fission products from fissions in uranium and plutonium in the core and breeder were considered. Fission-rates per atom for  $U^{235}$ ,  $U^{238}$ ,  $Pu^{239}$ ,  $Pu^{240}$ ,  $Pu^{241}$  were obtained from the GOG calculations via a processing program. These were multiplied by the appropriate atomic concentrations and summed to give total fission-

rates  $\text{cm}^{-3} \text{sec}^{-1}$  (Table 4). The energy spectrum was based on the experimental fits given by Goldstein [54] for thermal fission in  $\text{U}^{235}$ . These were renormalised to give a total energy release of 15 MeV per fission and used to calculate the total energy in each source group, expressed as the number of photons per group (Table 5).

(ii) Capture in Plutonium and Uranium in the Core

Values of the capture-rate per atom for  $\text{U}^{235}$ ,  $\text{U}^{238}$ ,  $\text{Pu}^{239}$  and  $\text{Pu}^{240}$  through the core were again obtained from the GOG calculations via a processing program. These were multiplied by the appropriate atomic concentrations, summed, and interpolated to give values of the total capture-rates at a uniform mesh in each region (Table 4).

The calculation was carried out using the energy spectrum from thermal capture in  $\text{U}^{238}$  given by Sidebotham [53].

(iii) Capture in Uranium in the Breeder

The capture-rates in the breeder region were calculated as in the core. In the breeder region the largest contribution to the total dose-rate is provided by neutron capture in uranium. A possible source of error in the calculation of this component is the use for all neutron energies of a capture gamma spectrum measured for thermal capture. In addition to using the Sidebotham energy spectrum, a spectrum was derived from energy dependent spectra for  $\text{U}^{238}$  calculated at ORNL [55]. Values of the neutron capture-rate in  $\text{U}^{238}$  at a mid-breeder position were calculated as a function of energy. Using these as weighting factors the energy dependent spectra were averaged to produce a single spectrum throughout the breeder. The lowest gamma-ray energy considered in the ORNL set

Table 4

Reaction Rates and Source Strengths (MZB McGID Calculation)

Region	Co-ord (cm)	Reaction rate (per cm <sup>3</sup> per sec)			Source (photons per cm <sup>3</sup> per sec)	
		Fission	Capture		Inelastic scatter	
			U and Pu	Steel	U and Pu	Steel
Inner core	0.0	7.16,6	7.03,6	6.83,5	1.14,7	1.19,7
	5.184	7.13,6	7.01,6	6.82,5	1.14,7	1.18,7
	10.368	7.07,6	6.95,6	6.77,5	1.13,7	1.17,7
	15.551	6.99,6	6.86,6	6.67,5	1.11,7	1.16,7
	20.735	6.85,6	6.72,6	6.54,5	1.09,7	1.14,7
	25.919	6.68,6	6.56,6	6.37,5	1.06,7	1.12,7
	31.103	6.47,6	6.35,6	6.17,5	1.03,7	1.08,7
	36.287	6.24,6	6.08,6	5.93,5	9.93,6	1.04,7
	41.471	5.95,6	5.80,6	5.66,5	9.54,6	1.00,7
	46.654	5.65,6	5.47,6	5.35,5	9.15,6	9.57,6
	51.838	5.33,6	5.12,6	5.02,5	8.73,6	9.06,6
	57.022	4.98,6	4.71,6	4.66,5	8.33,6	8.60,6
	62.206	4.59,6	4.26,6	4.24,5	8.03,6	8.38,6
	Outer core	62.206	6.48,6	4.52,6	4.10,5	8.27,6
65.693		6.05,6	4.20,6	3.84,5	7.83,6	8.06,6
69.181		5.59,6	3.89,6	3.54,5	7.27,6	7.52,6
72.668		5.05,6	3.57,6	3.24,5	6.45,6	6.69,6
76.156		4.50,6	3.35,6	2.93,5	5.43,6	5.56,6
79.643		3.93,6	3.14,6	2.63,5	4.24,6	4.27,6
Breeder	79.643	5.86,5	3.46,6	2.42,5	5.19,6	3.40,6
	82.736	4.09,5	3.16,6	2.20,5	3.66,6	2.42,6
	85.830	2.91,5	2.86,6	1.96,5	2.57,6	1.68,6
	88.923	2.13,5	2.57,6	1.75,5	1.79,6	1.17,6
	92.016	1.58,5	2.27,6	1.54,5	1.27,6	8.11,5
	95.109	1.18,5	1.97,6	1.33,5	8.96,5	5.72,5
	98.203	8.96,4	1.70,6	1.15,5	6.37,5	4.06,5
	101.296	6.86,4	1.47,6	9.95,4	4.53,5	2.88,5
	104.389	5.31,4	1.27,6	8.74,4	3.23,5	2.02,5
	107.483	4.31,4	1.11,6	7.63,4	2.30,5	1.45,5
110.576	3.54,4	9.73,5	6.86,4	1.66,5	1.02,5	
Steel reflector	110.576			2.88,5		7.43,5
	112.231			2.90,5		5.84,5
	113.887			2.91,5		4.47,5
	115.542			2.92,5		3.42,5
	117.198			2.92,5		2.65,5
	118.853			2.96,5		2.07,5
	120.509			3.06,5		1.63,5
	122.164			3.34,5		1.28,5
	123.820			3.98,5		1.02,5
	125.475			5.53,5		8.14,4
127.131			9.30,5		6.57,4	
Graphite reflector	127.131			5.32,4		3.86,3
	130.748			7.98,4		2.60,3
	134.365			9.67,4		1.74,3
	137.982			1.05,5		1.17,3
	141.599			1.08,5		7.93,2
	145.216			1.09,5		5.33,2
148.833			1.09,5		3.54,2	

Table 5

Source Energy Spectra for the MZB Radial Calculations

Source Energy Groups			Photons per Reaction						Photon fraction		
			Fission	Capture					Inelastic Scatter		
			U & Pu	U & Pu (Sidebotham)	U (ORNL)	Steel			U & Pu	Steel	
Group Number	Upper Energy (MeV)	Lower Energy (MeV)	Core and Breeder	Core and Breeder	Breeder	Core	Breeder	Reflector	Core and Breeder	Core and Breeder	Reflector
1	7.4	6.6	0.0039	0.0	0.0	0.7574	0.7156	0.6387	0.0022	0.0068	0.0024
2	6.6	5.8	0.0157	0.0	0.0	0.1369	0.1476	0.1658	0.0029	0.0051	0.0018
3	5.8	4.95	0.0414	0.0	0.0	0.0297	0.0266	0.0249	0.0041	0.0062	0.0022
4	4.95	4.0	0.1249	0.0185	0.0248	0.0897	0.0986	0.1147	0.0172	0.0051	0.0018
5	4.0	3.2	0.2726	0.0583	0.0603	0.0949	0.1043	0.1166	0.0180	0.0053	0.0019
6	3.2	2.7	0.3444	0.0414	0.1168	0.0763	0.0828	0.0898	0.0367	0.0090	0.0035
7	2.7	2.35	0.3836	0.0752	0.1614	0.0542	0.0577	0.0592	0.0426	0.0101	0.0039
8	2.35	1.875	0.8198	0.3550	0.3130	0.0955	0.0985	0.0874	0.0692	0.0163	0.0064
9	1.875	1.275	1.8609	0.6451	0.5082	0.1757	0.1960	0.2444	0.1170	0.0276	0.0107
10	1.275	0.88	2.1457	0.5708	0.4423	0.0753	0.0844	0.0987	0.1158	0.0734	0.0664
11	0.88	0.635	2.2415	0.6376	0.6376	0.1550	0.1633	0.1846	0.1100	0.1598	0.1721
12	0.635	0.39	3.5570	1.2371	1.2371	0.0558	0.0478	0.0386	0.1625	0.2362	0.2543
13	0.39	0.15	2.3385	2.1222	2.1222	0.1233	0.1074	0.1237	0.3019	0.4391	0.4726

is 1 MeV and the spectrum below this energy was therefore taken from the data of Sidebotham. The whole spectrum was renormalised to make the total energy the same as that of the Sidebotham spectrum so that the exercise was a test of the spectrum shape only. A condensed version of the ORNL spectrum is given in Table 5 for comparison with the 13 group Sidebotham spectrum.

(iv) Capture in Steel in the Core

The total capture-rates in the stainless steel of the core were calculated by combining the rates for iron, chromium and nickel in a manner similar to that for the plutonium and uranium contribution (Table 4). At the same time, the proportion of captures occurring in each element were calculated at various points and representative values were chosen. These were used as weighting factors to combine the 13 group capture gamma spectra given by Sidebotham. The proportions for the iron, chromium and nickel were 0.655, 0.123, 0.222 respectively and the spectrum obtained is given in Table 5.

(v) Capture in Steel in the Breeder

The method of obtaining the source is as in (iv) and the corresponding weighting factors were 0.769, 0.112 and 0.119 respectively.

(vi) Capture in Steel in the Reflector

Capture-rates in iron and manganese in the reflector were calculated with the REDIFFUSION program [56]. This was run in plane geometry starting at the breeder edge and using the GOG calculations to supply the fission sources, starting spectrum and axial buckling values in the reflector. The capture-rates for steel are set out in Table 4. Values of the proportion of captures occurring in iron

and manganese were also calculated at various points and the representative values of 0.97 and 0.03 were chosen respectively. These were used as weighting factors to combine the Sidebotham capture gamma spectra for iron and manganese (Table 5).

(vii) Inelastic Scatter

The sources were calculated using the gamma-ray production cross-sections for  $U^{238}$  and Fe which are reproduced in Table 6. Flux values from the GOG calculations were used to obtain the source strengths (photons  $cm^{-3} sec^{-1}$ ) at each point (Table 4) and the 13 group spectrum is given in Table 5.

Table 6

Cross-Sections for Gamma-Ray Production from Inelastic Scatter

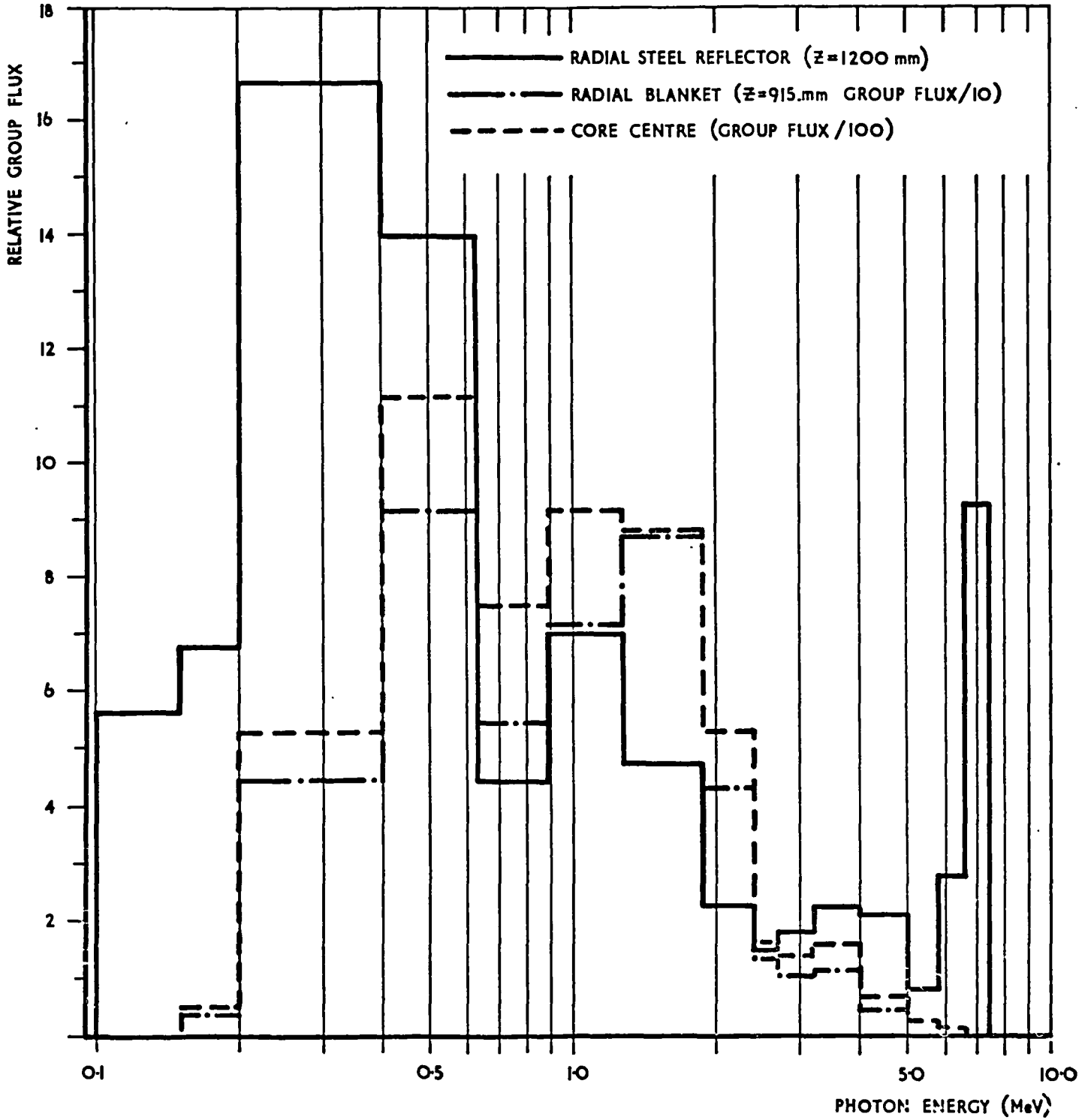
Neutron Energy Range (MeV)	Cross-Sections for U238				
	Gamma-Ray Energy Range (MeV)				
	0.0-1.0	1.0-3.0	3.0-5.0	5.0-7.0	7.0-9.0
10.0 - 7.5	1.226	0.307	0.020	0.209	0.293
7.5 - 6.5	2.432	0.610	0.093	1.152	0.0
6.5 - 5.5	3.086	0.787	0.631	1.121	0.0
5.5 - 4.5	2.672	0.751	1.966	0.0	0.0
4.5 - 3.5	2.130	1.044	1.334	0.0	0.0
3.5 - 2.5	1.548	2.724	0.0	0.0	0.0
2.5 - 1.5	1.212	1.715	0.0	0.0	0.0
1.5 - 0.85	1.673	0.052	0.0	0.0	0.0
0.85 - 0.5	0.418	0.0	0.0	0.0	0.0
Neutron Energy Range (MeV)	Cross-Sections for Iron				
	Gamma-Ray Energy Range (MeV)				
	0.0-1.0	1.0-3.0	3.0-5.0	5.0-7.0	7.0-9.0
10.0 - 7.5	2.313	0.578	0.037	0.395	0.552
7.5 - 6.5	2.082	0.522	0.079	0.986	0.0
6.5 - 5.5	1.775	0.453	0.363	0.644	0.0
5.5 - 4.5	1.076	0.718	0.144	0.0	0.0
4.5 - 3.5	1.184	0.567	0.097	0.0	0.0
3.5 - 2.5	1.546	0.235	0.0	0.0	0.0
2.5 - 1.5	1.445	0.0	0.0	0.0	0.0
1.5 - 0.85	0.808	0.0	0.0	0.0	0.0

### 6.1.3 Results

In each of the nine runs it was not necessary to obtain accurate results at points remote from the source region as the dose at any point is dominated by gamma-rays which originate in the immediate vicinity. The use of splitting for variance reduction was therefore limited to regions close to the source. Where there was considerable variation in the source strength, notably for sources in the breeder, importance sampling was used so that the sampling distribution was approximately uniform over the source region. Standard deviations of approximately 4% for the dose-rates were obtained.

In order for direct comparison with the dose-rates measured using the ionisation chambers and the SSCD, dose-rate conversion factors for zirconium as a function of energy were input as a step function to McGID. These were obtained from the mass energy absorption coefficient data set for zirconium described in sub-section 3.1.4. The spectra for various regions used in the PROCEED calculations are given in Figure 19. The total calculated dose-rates are presented in graphical form with the experimental results in sub-section 6.4 where the conclusions are made. Table 7 gives the calculated contributions expressed as a percentage of the total dose-rate at various positions, and it shows the dose in the core was dominated by fission gamma-rays, the dose in the breeder was dominated by capture gamma-rays from  $U^{238}$ , and the dose in the reflector was dominated by capture gamma-rays from the steel. The values of the dose-rates predicted by the ORNL derived spectrum described in 6.1.2 (iii) differed by about 3-5% from those given by the original calculation, but since the standard deviation of





PHOTON SPECTRA IN THE MZB(2) ASSEMBLY (MCGID CALCULATIONS)  
 FIGURE 19

these results was of the same order, this difference was not statistically significant.

Table 7

Percentage Contributions to the Dose-Rates in MZB

Position	Fission	Capture					Inelastic Scatter		
	U & Pu	U & Pu		Steel			U & Pu	Steel	
	Core and Breeder	Core	Breeder	Core	Breeder	Reflector	Core and Breeder	Core and Breeder	Reflector
Core centre	65	18	-	4	-	-	8	4	-
Mid-breeder	18	-	60	-	8	-	10	3	-
Mid-steel reflector	-	-	3	-	-	91	-	-	5
Mid-graphite reflector	-	-	-	-	-	99	-	-	1

## 6.2 The MZC Assembly Calculations

The neutron calculations from which the gamma-ray sources were obtained are described in Paper A17, Reference [4]. The calculations were performed using diffusion theory - RZ models for the rods in the central position and an XY geometry for the Ta(S) case. The gamma-ray calculations were performed by Avery [57] and only a brief outline will be given here. The method of obtaining the sources was as described in sub-section 6.1 for the MZB calculations.

An RZ model of the control rods was adopted for predicting gamma-ray migration for the centre position and the calculations were carried out with the program McGID. The rod was represented by a region of radius 42.35 mm for the absorber, calandria tubes and intervening sodium, surrounded by an annulus of thickness 18.87 mm for the control rod

sheath, sodium and outer sheath. The core region then extended outwards from the radius of 61.22 mm to a square reflecting outer boundary at 220 mm from the rod centre. This representation of the rod is similar to that adopted for the neutron calculations. In the axial direction, the source was constant with reflecting boundaries at the top and bottom thus giving an infinitely long cylindrical model of the control rod. Separate runs were carried out as in the MZB calculation to give energy deposition rates in the central 14 mm region of the homogenised representation of the B<sub>4</sub>C and Ta pins. Table 8 gives the percentage contributions to the dose-rates in these three situations.

Table 8  
Percentage Contributions to the Dose-Rates in MZC

Gamma-Ray Source	Percentage Contribution Ta(0)	Gamma-Ray Source	Percentage Contribution	
			B <sub>4</sub> C (natural)	B <sub>4</sub> C (80% enriched)
Fission	6.4%	Fission	46.0%	35.0%
U/Pu Capture	1.8%	U/Pu Capture	13.8%	9.3%
Steel Capture	0.5%	Steel Capture	10.4%	6.6%
Tantalum Capture	87.8%	Boron Capture	26.8%	46.8%
Tantalum Inelastic Scatter	3.1%	Steel Inelastic Scatter	2.1%	1.6%
Steel Inelastic Scatter	0.2%	U/Pu Inelastic Scatter	0.8%	0.6%
U/Pu Inelastic Scatter	0.1%			
Total	100%	Total	100%	100%

The calculation of the dose-rate in the tantalum rod when positioned close to the edge of the core was carried out in XY geometry with the code McBOX [56, 58]. The model adopted for the control rod was to homogenise the absorber and calandria regions of the RZ model into a single material. The neighbouring locations were occupied by core elements on three sides and breeder elements on the other. The area of

the model extended to the width of two ZEBRA elements on all four sides of the calandria. The area of the model for the calculation was thus a 6 x 6 ZEBRA array (325.5 mm square). The central region of the McBOX model covered the area of the absorber and calandria and eight surrounding regions represented the adjacent core and breeder elements. In the McBOX calculation it was possible to vary the source spectrum from region to region, and a single calculation was therefore performed for the sums of the sources from all of the reactions for each of the nine regions. The energy deposition was derived from the mean fluxes within the homogenised absorber using the appropriate dose-rate conversion factors as in the MZB calculations.

The calculated dose-rates are presented in sub-section 6.4 with the experimental results. The various corrections necessary before any comparison can be made are described in sub-section 6.3. However, discussion of the accuracy of the MZC calculations will be given here to illustrate the uncertainties which must be considered in this type of calculation.

#### 6.2.1 Accuracy of the MZC Calculations

##### (i) Neutron Reaction-Rates

The accuracy of the diffusion theory neutron reaction-rate calculations can be assessed for the core centre assemblies from Table VIII in Paper A17, Reference [4]. In the Ta case the distribution of  $U^{235}$  and  $U^{238}$  fissions was predicted within the core to an accuracy of better than 2%. Within the rod the errors become larger and the Ta capture-rate was overestimated by 9.3% in the centre pin. In the  $B_4C$  assemblies the behaviour was similar, although it was not possible to measure the capture-rate in  $B^{10}$  directly. The  $U^{235}$  fission-rate was overestimated

by 6% at the centre pin of the natural assembly and by 10% for the enriched assembly. If this accuracy was assumed to extend to the boron capture-rates then they would also be overestimated. This was consistent with the predictions of control rod worths. There were no reaction-rate measurements for the Ta(S) assembly and it was assumed that the neutron capture-rate errors in Ta(O) were applicable. In the results given in Table 12, calculated values with corrections for neutron capture-rates in the absorber are also included.

(ii) Normalisation of the Core Calculation

The normalisation for the  $B_4C$  assemblies was made relative to  $U^{235}$  fission foil measurements in position 40-50, the accuracy of the fission-rates estimated at  $\pm 5\%$ . For the tantalum assemblies no direct normalisation factors were available. It was therefore assumed that the  $U^{235}$  fission-rate at a position remote from the absorber was the same in Ta(O) with its extra loading of 24 elements (Paper A17, [4]) as in the natural  $B_4C$  with the 29 extra elements. Although Ta(S) required only 8 extra elements it was necessary to make the same assumptions. This introduced further uncertainty and an error of  $\pm 10\%$  was therefore attributed to the normalisation of Ta(O) and  $\pm 20\%$  to Ta(S).

(iii) The Gamma-Ray Calculations

The uncertainties due to the Monte Carlo statistics were less than 6% in all cases and are detailed in Table 12. However, further uncertainties must be included for the gamma-ray source energy and spectra. The gamma-ray energy released in fission due to prompt and delayed emission is given errors of  $\pm 14\%$  for  $Pu^{239}$  and  $\pm 13\%$  for  $U^{238}$  by James [59]. For capture sources the energy

emitted is well known although there are uncertainties in the spectra. The models adopted of the control rod mock-ups may have influenced the calculations - the main effects being the homogenisation of the pins and the replacement in the RZ model of the square outer boundary of the calandria element by a circular boundary. Without repeating the calculations with a more detailed representation of the assemblies it is difficult to estimate these effects. The overall uncertainties due to normalisation and statistics ranges from 7% in the central position to 21% in the outer core - this is discussed further in sub-section 6.4.

### 6.3 Corrections to the Measurements

In order that comparison could be made between the measured values and the calculated gamma-ray dose-rates it was necessary to make several corrections, some of which have been discussed in earlier sections. The complete dose-mapping of ZEBRA during the MZB program accumulated a vast amount of data that was necessary for the subsequent analysis. A computer program was therefore written to apply all the corrections to the "raw" IG8/TLD experimental data and calculate the uncertainties. This section describes the various stages of the correction program and gives a description of the necessary input data which illustrates the magnitude of the problem. Approximately 1000 ionisation chamber measurements and 200 TLD measurements were made over the MZB assembly. The special considerations associated with the MZC and DMSA measurements are discussed in sub-section 6.3.7.

#### 6.3.1 ZEBRA Geometry and Measurement Position Data

A model of the MZB assembly was specified in terms of region boundary positions and ZEBRA element positions. The relative location of an ionisation chamber measurement was given in terms

of the element number (ie 50-42) and the calibrated tube reading (5.5.1) and the program could convert this to an absolute position in the assembly (mm from the core centre). The locations of the TLD were calibrated in terms of distance from the end of the SSCD and it was a simple matter to obtain an accurate datum in the core.

### 6.3.2 Ionisation Chamber Readings

The current measuring devices used in this work contained a range selection switch which altered the instrument's full-scale deflection in six steps from  $10^{-9}$  amps to  $3 \times 10^{-12}$  amps. Each range had a separate current calibration at some 30 instrument readings. While taking a measurement it was therefore necessary to record both current and range setting in order that the program could adjust the current correctly. For a particular measurement instrument reading the adjusted value was obtained via a cubic spline fit to the current calibration data. It was then necessary to apply the appropriate chambers' gamma-ray sensitivity (amps/rad hr<sup>-1</sup>; Appendix A).

### 6.3.3 TLD Light Output Readings

The measured light counts were converted to dose by interpolating a cubic spline fit to a supralinearity calibration curve appropriate to the particular batch of TLD crystals.

### 6.3.4 Neutron Sensitivity

The neutron flux in the 37 fast reactor group scheme at 660 positions, as computed by an RZ GOG calculation, was input to the analysis program. In addition, for each isotope contributing to the neutron dose-rate, the information given in Appendix B and sub-

section 3.2.6 was required in the  $^{37}$  group scheme. This amounted to the appropriate elastic scattering cross-sections, the average cosine of the scattering angle, and the average energy required by the recoil nucleus to produce one iron pair (or in the case of SSCD results the relative sensitivity to the TLD recoils). The dose-rate due to neutron recoils ( $N_c$ ) was calculated at every measurement position by interpolation of the flux values given at the 660 model positions. The value of  $S_c$ , the relative sensitivity to these recoils, was obtained as described in Appendix B for the chamber measurements. Table 9 shows the magnitude of this correction ( $C_1 = S_c N_c / d_m$ ) at the core centre and mid-blanket.

Table 9

Magnitude of the Neutron Sensitivity Correction (-C %) and Non-Saturation of Fission Product Activity Correction (+C<sub>2</sub>%) for Ionisation Chamber Measurements - Dose-Rates (D rad hr<sup>-1</sup>) at the Core Centre and Mid-Blanket

Scan Position (distance from centre (mm))	Centre Plane			Mid-Blanket		
	D	C <sub>1</sub>	C <sub>2</sub>	D	C <sub>1</sub>	C <sub>2</sub>
50-50 (0.0)	958	3.1	4.1	117	1.7	1.2
50-48 (107.4)	951	3.1	5.2	112	1.8	1.0
50-46 (217.5)	916	3.1	4.0	110	1.8	0.8
50-44 (325.0)	966	2.8	5.9	116	0.9	1.8
50-42 (435.0)	760	3.2	4.4	90	1.1	1.1
50-40 (542.5)	779	2.9	6.7	92	1.1	1.5
50-37 (706.3)	597	2.9	5.9	65	1.6	1.0
50-35 (813.7)	245	2.8	2.4	42	0.0	1.5
50-32 (977.5)	81	1.2	0.8	21	0.0	1.7
50-30 (1085.0)	39	0.0	0.6	16	0.0	1.2
50-68 (977.5)	85	1.2	0.5	21	0.0	1.6



### 6.3.5 The Non-Saturation of Fission Product Activity

This correction was briefly outlined in sub-section 5.5.3.

If  $d_n$  is the total measured neutron corrected dose-rate and  $d_f$  is the dose-rate due to fission product decay contributing to D

and  $d_{fc}$  is the calculated dose-rate due to fission product decay then  $d_f < d_{fc}$  due to the non-saturation of fission product photons:

$$d_f = \frac{f_t}{f_s} d_{fc} \quad - - - \quad (23)$$

where  $f_t$  is the fission product photon source at the time of measurement;

and  $f_s$  is the fission product photon source at saturation.

Therefore the true dose-rate D in the photon source regions is given by:

$$D = d_n + d_{fc} \left(1 - \frac{f_t}{f_s}\right) \quad - - - \quad (24)$$

One-dimensional McGID calculations for the MZB depleted-sector core were carried out for the various processes contributing to the total dose-rate. Table 10 gives the total calculated dose-rate at radial positions, and the contribution to this dose-rate from fission. The following exponential fits to the fission gamma spectra are given in Reference [54]:

Prompt gammas:

0.3 to 1.0 MeV	$N(E_\gamma) = 26.8e^{-2.3E_\gamma}$
1.0 to 7.0 MeV	$N(E_\gamma) = 8.0e^{-1.1E_\gamma}$

[Photons above 7 MeV negligible.]

Table 10

1D McGID Calculation - Radial Scan Gamma Dose-Rates (Zr: rad hr<sup>-1</sup>)

	Position From Centre (mm)	Total Dose-Rate	Fission Dose-Rate	Decay Dose-Rate	Decay % Total
Inner Core	5.000	1037.1816	672.2490	265.9482	25.64
	30.000	1073.7830	700.2263	277.0164	25.80
	76.220	1074.0662	701.7620	277.6240	25.85
	107.440	1040.1143	680.7903	269.3274	25.89
	131.220	1037.7354	687.9060	272.1423	26.22
	181.261	1007.8633	649.8186	257.0747	25.51
	217.522	975.2947	621.8965	246.0284	25.23
	246.261	1009.5327	659.9729	261.0918	25.86
	294.981	994.3044	648.5369	256.5676	25.80
	324.962	963.0100	619.4436	245.0581	25.45
	354.981	946.9685	617.9629	244.4723	25.82
	405.022	907.3328	591.2786	233.9157	25.78
	435.044	838.6504	546.6609	216.2645	25.79
	465.022	862.4358	570.3176	225.6233	26.16
	513.742	805.3110	533.9541	211.2376	26.23
	542.484	792.9158	519.0923	205.3581	25.90
563.742	765.9011	503.5017	199.1903	26.01	
601.030	774.1106	522.2305	206.5996	26.69	
Outer Core	636.030	832.5168	589.3892	233.1682	28.01
	655.000	830.2441	606.5046	239.9393	28.90
	680.643	747.5024	521.3132	206.2367	27.59
	706.286	708.2935	498.7615	197.3150	27.86
	730.643	656.0327	455.3037	180.1227	27.46
	755.000	604.9565	422.6858	167.2187	27.64
778.215	483.1108	316.0144	125.0184	25.88	
Depleted Blanket	802.578	297.9707	158.4603	62.6885	21.04
	813.726	232.3326	104.4494	41.3212	17.79
	834.363	178.7648	64.0261	25.3293	14.17
	855.000	142.4806	40.3648	15.9687	11.21
	885.000	112.4183	25.9905	10.2821	9.15
	915.000	90.8575	16.4228	6.4970	7.15
	946.264	76.0413	12.9036	5.1048	6.71
	977.528	61.8538	8.0374	3.1797	5.14
	1006.264	51.5082	5.5382	2.1910	4.25
	1054.984	39.2985	4.4950	1.7783	4.53
1084.968	32.9981	2.9567	1.1697	3.54	
1097.864	31.5727	2.5185	0.9963	3.16	
Steel	1127.880	29.4081	0.7815	0.3092	1.05
	1155.000	26.0215	0.3146	0.1245	0.48
	1180.000	26.0104	0.1707	0.0675	0.26
	1205.000	27.2391	0.1122	0.0444	0.16
	1230.000	29.1728	0.0391	0.0155	0.05
	1255.000	35.8997	0.0126	0.0050	0.01
	1265.650	34.3671	0.0106	0.0042	0.01
Graphite	1285.650	30.6192	0.0113	0.0045	0.01
	1305.000	29.9473	0.0114	0.0045	0.02
	1330.000	28.8435	0.0092	0.0036	0.01
	1355.000	29.1407	0.0054	0.0021	0.01
	1380.000	27.9242	0.0043	0.0017	0.01

Fission product decay gammas:

$$N(E_\gamma) = 6.0e^{-1.1E_\gamma}$$

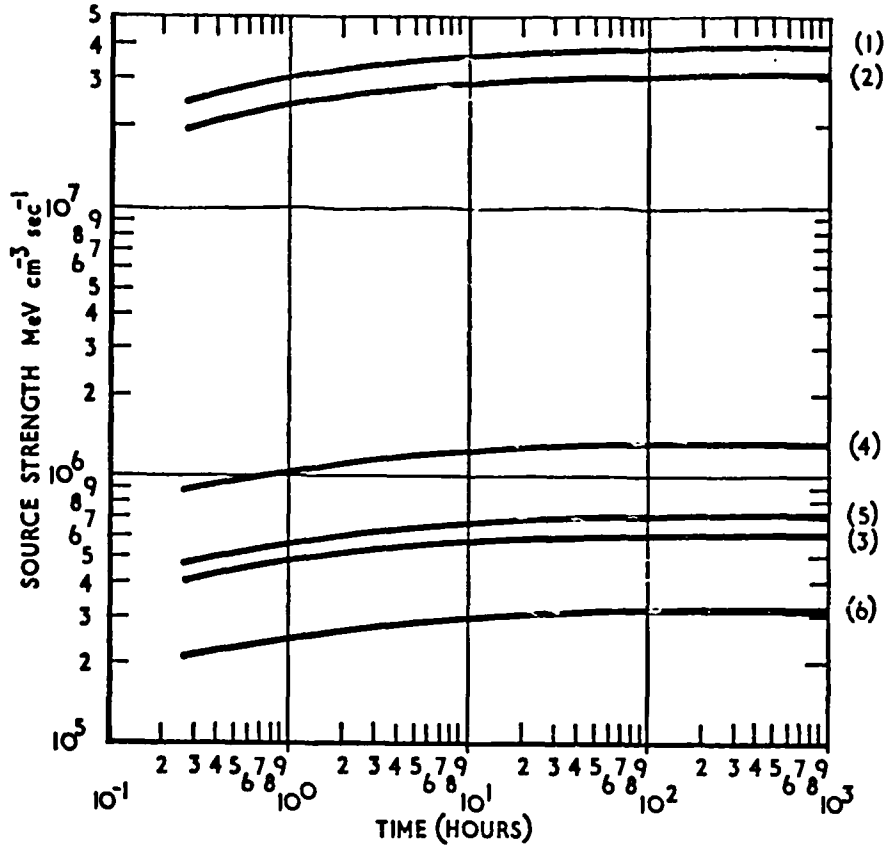
Thus, the ratio of fission product decay gammas to the total fission gamma source is given by:

$$\frac{6.0 \int_{0.3}^{7.0} E_\gamma e^{-1.1E_\gamma} dE_\gamma}{26.8 \int_{0.3}^{1.0} E_\gamma e^{-2.3E_\gamma} dE_\gamma + 8.0 \int_{1.0}^{7.0} E_\gamma e^{-1.1E_\gamma} dE_\gamma + 6.0 \int_{0.3}^{7.0} E_\gamma e^{-1.1E_\gamma} dE_\gamma} = 0.3956 \quad \text{--- (25)}$$

The fourth column of Table 10 gives the dose-rate due to fission product decay ( $d_{fc}$ ) and the final column quotes these values as a percentage of the total calculated dose-rate. It can be seen from this that the penetration contribution in the reflector rapidly decreases from 1%.

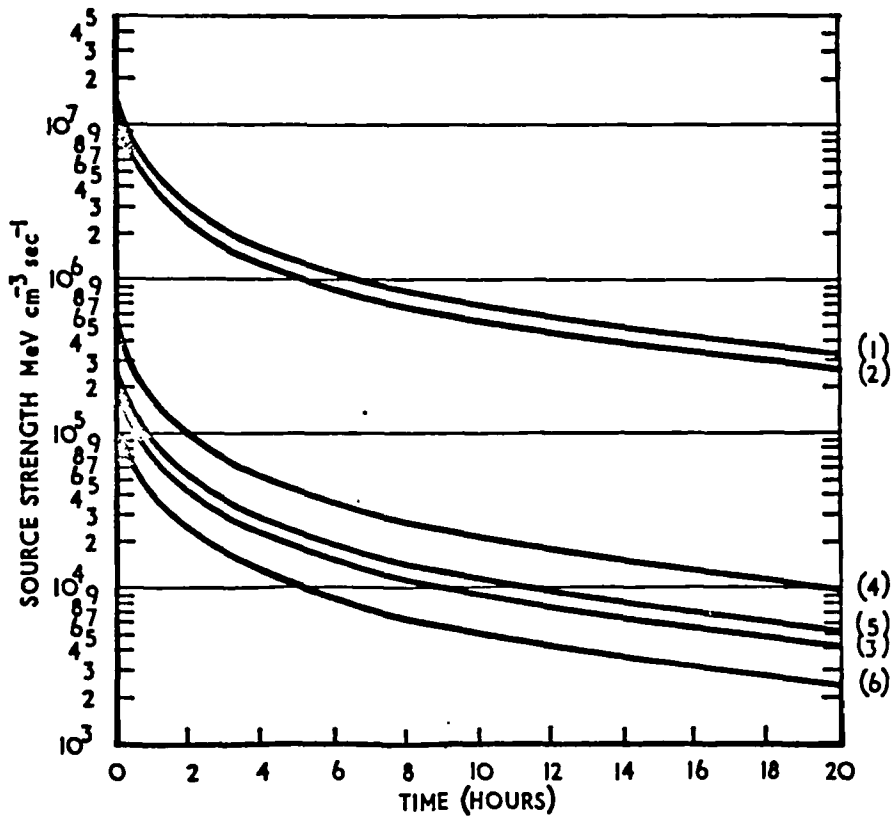
The contribution to the total gamma dose-rate from the fission process in the MZB depleted-sector core was also calculated using McGID for an RZ model. Again, interpolation at every measurement point by cubic spline fits to the RZ positions was carried out.

In order to calculate  $\frac{f_t}{f_s}$  the program FISPIN [60] was used. The fission-rates for each isotope were obtained from an RZ GOG calculation (normalisation factor of  $2.390 \times 10^4$ ) and the fission product gamma source was calculated for each isotope at various times. The results were summed to give build-up curves for the six source regions (Figure 20). Decay curves after a 7 hour full power run are given in Figure 21.



MZB(2) FISSION PRODUCT GAMMA BUILD-UP CURVES (FULL POWER)  
FIGURE 20

- (1) CORE CENTRE
- (2) MID-OUTER CORE
- (3) MID-INNER RADIAL BLANKET
- (4) MID-INNER AXIAL BLANKET
- (5) MID-OUTER AXIAL BLANKET
- (6) MID-OUTER RADIAL BLANKET



MZB(2) FISSION PRODUCT GAMMA DECAY CURVES (AFTER 7 HOUR FULL  
POWER RUN)  
FIGURE 21

FISPIN cannot calculate for  $\text{Pu}^{241}$  fast fission and thus the total source in the core regions was probably 3% low. However, this would have a negligible effect on the ratio  $\frac{f_t}{f_s}$ . The value of  $f_s$  was calculated for 1000 hours.

For cases where the pre-scan history was not a constant full power run the calculation of  $\frac{f_t}{f_s}$  is a little more difficult and two cases are outlined:

(i) For scans made after lower power runs:

Say x% power for time  $t_1$ , then y% power for time  $t_2$  and finally z% power for time  $t_3$  when scan made. Total time before scan =  $t_1 + t_2 + t_3$

$$f_t = f_{t(3)}^{(x\%)} + f_{t(3-1)}^{(y-x\%)} + f_{t(3-2)}^{(z-y\%)}$$

(ii) For pre-scan histories containing a shut-down:

Say x% power for time  $t_1$ , followed by shut-down lasting time  $t_2$ . Then z% power for time  $t_3$  when scan made.

$$f_t = f_{t(3-1)}^{(x_d)} + f_{t(3-2)}^{(z\%)}$$

where  $f_{t(3-1)}^{(x_d)}$  is source after decay for time  $t_3 - t_1$

from shut-down after run at x% for time  $t_1$ .

The effect on the fission product decay source from the previous day's run was also considered. Assuming a 9.30 am balance and 4.30 pm shut-down, the source was calculated after a 7 hour full power run at decay times up to 20 hours (Figure 21). For the case of a measurement 2 hours after balance, following the above history,

about 1% of the source was due to the previous day's run and thus could be neglected.

Although each scan took at least 30 minutes, the change in  $\frac{f_t}{f_s}$  over the scan period was not computed.

Table 11 gives the ratio  $\frac{f_t}{f_s}$  for the scan histories preceding the MZB gamma dose-rate measurements and Table 9 shows the magnitude of the non-saturation correction ( $C_2 = (D - d_n)/d_n$ ) at the core centre and mid-blanket positions.

### 6.3.6 The TLD Cavity Correction

The cavity corrections to the MOZART TLD measurements were calculated with the program PROCEED. Computed gamma-ray spectra (eg from McGID) were input to PROCEED from which the secondary particle source spectra were obtained. Examples of the calculated MZB spectra are given in Figure 19. The cavity correction was calculated for only a few positions within each assembly region and values interpolated for each point in a dose-rate scan. Typically in zirconium, to obtain the cavity correction to better than 2% required approximately 20 minutes computing time. In MZB the correction was approximately 10% in the core region, this decreased slightly in the blanket and then increased rapidly in the reflector regions. The magnitudes of the cavity correction for the MZC results are given in Table 12, the corrections in the B<sub>4</sub>C situations being for grouped TLD as described in sub-section 5.5.2. Burlin's theory was also applied to the MOZART measurements. For all but the MZC Ta cases, where the theory predicted lower values for the spectrum averaged cavity corrections, results were in agreement with the PROCEED calculations.

Table 11

The Ratio of the Fission Product Photon Source  
at Time of Measurement ( $f_t$ ) to the Source  
at Saturation ( $f_s$ ) for the MZB Histories

Position	History (times in minutes from balance to scan)	$f_t/f_s$					
		Inner Core	Outer Core	Inner Radial Blanket	Inner Axial Blanket	Outer Axial Blanket	Outer Radial Blanket
50-30(2)	69			0.80			0.79
50-32(1)	70			0.80			0.79
50-32(2)	130			0.85			0.83
50-32(T)	96			0.83			0.81
50-35(2)	20% 15 50% 73 SD 50 50% 137 109% 52			0.83			0.81
50-37(1)	109% 120 SD 64 109% 164		0.86			0.87	
50-37(2)	126		0.82			0.84	
50-37(T)	90		0.79			0.81	
50-40(2)	20% 15 50% 73 SD 50 50% 137 109% 22	0.75			0.77		
50-42(1)	210	0.85			0.87		
50-42(2)	195	0.85			0.86		
50-42(T)	120	0.82			0.83		
50-44(2)	68	0.77			0.79		
50-46(2)	30% 64 109% 290	0.87			0.88		
50-48(2)	166	0.84			0.85		
50-50(2)	30% 64 109% 145	0.84			0.85		
50-50(T)	30% 64 109% 245	0.86			0.88		
50-68(1)	109% 120 SD 63 109% 95			0.86			0.84
Radial(T)	412	0.88	0.88	0.90			
Radial(T)	457	0.89	0.89	0.90			
Radial(T)	660	0.90	0.90	0.92			
Radial(T)	705	0.90	0.90	0.92			

(1) = Electrometer 1

(2) = Electrometer 2

(T) = TLD

SD = Shut-Down

### 6.3.7 The MZC and DMSA Measurements

For the MZC and DMSA experiments the TLD were necessarily loaded before start-up and unloaded some time following shut-down. The photon source strengths from fission used in the MZC calculations are for saturated accumulations of fission products. In the experiments the operation period was too short for saturation to be approached and the contribution from fission sources were therefore reduced by appropriate factors to allow for this. These were derived with FISPIN for the operation times given in Table 12, including the run up to power and decay following shut-down in the period before the removal of the detectors. An integration over these times to obtain the total fission product sources was then compared with the saturation source for the period at power to provide correction factors for the heating rate due to fission sources. These effects typically reduced the energy deposition from fission by a factor of 0.82 and, unlike MZB, this correction was applied to the calculations. It is also necessary to account for the neutron dose-rate during these periods and this amounted typically to a 6% increase in the full power dose-rate.

## 6.4 Discussion of the Results

The MOZART program of calculations has been completed but, to date, the Assembly 13 gamma-ray calculations have not been undertaken. However, experimental results have been included for Assembly 13 to demonstrate the power of the TLD technique. The results (pages 91-100) for the MZB Assembly are presented graphically in Figures 22-28; the MZC measurements and calculations are compared in Table 12; the gamma DMSA experimental results are presented in Tables 13-14, and the Assembly 13/3 within-element oxide breeder radial scan in Figure 29. Comparison of the



results of identical materials in the Assembly 13 gamma DMSA (Tables 13-14) demonstrate the reproducibility that can be achieved with  $\text{Li}^7\text{F}$  TLD. The within-element oxide breeder radial scan is also a good example of the capability of TLD.

Before drawing conclusions from any of the results it is necessary to discuss the associated uncertainties. The contributing factors to the accuracy of the measurements can be summarised as follows.

The absolute measurement positions are correct to  $\pm 2.5$  mm but relative positions to  $\pm 0.5$  mm. ZEBRA can be held steady at power to  $\pm 0.25\%$ . The accuracy of the calibration of the ionisation chambers was given in 3.1.4. To obtain the final uncertainty in the MZB chamber measurements it was necessary to include the calculated corrections described in 6.3. Although these were difficult to estimate due to the uncertainties involved in cross-section data, Monte Carlo calculations, et cetera, it was estimated that the neutron sensitivity correction had a standard deviation of approximately 15% and the non-saturation of fission product activity correction of 20%. Their small contribution resulted in an 8% standard deviation for dose-rates above approximately  $50 \text{ rad hr}^{-1}$  and 12% below  $50 \text{ rad hr}^{-1}$ . In calculating the correction to the 50-32 and 50-68 scans the depleted sector fluxes and cross-sections were used, but this introduced negligible further error. The calibration of the TLD was accurate to  $\pm 3\%$ , the reproducibility of light output from the detectors increased this to  $\pm 5\%$ . The correction for the neutron response was typically 15% and had an associated standard deviation of 15%. Including the various uncertainties previously discussed, the TLD measurements are considered accurate to  $\pm 10\%$ . This does not include the uncertainty

associated with the cavity correction. The Monte Carlo statistics for the PROCEED results were approximately 2%. There is the additional consideration of the accuracy of the input data, especially the calculated photon spectrum. The correction is very sensitive to the spectrum and improvements in the accuracy of the MOZART McGID calculations and the use of the finer structured group schemes could affect the calculated cavity corrections. The uncertainties associated with the MOZART calculations were discussed in section 6.

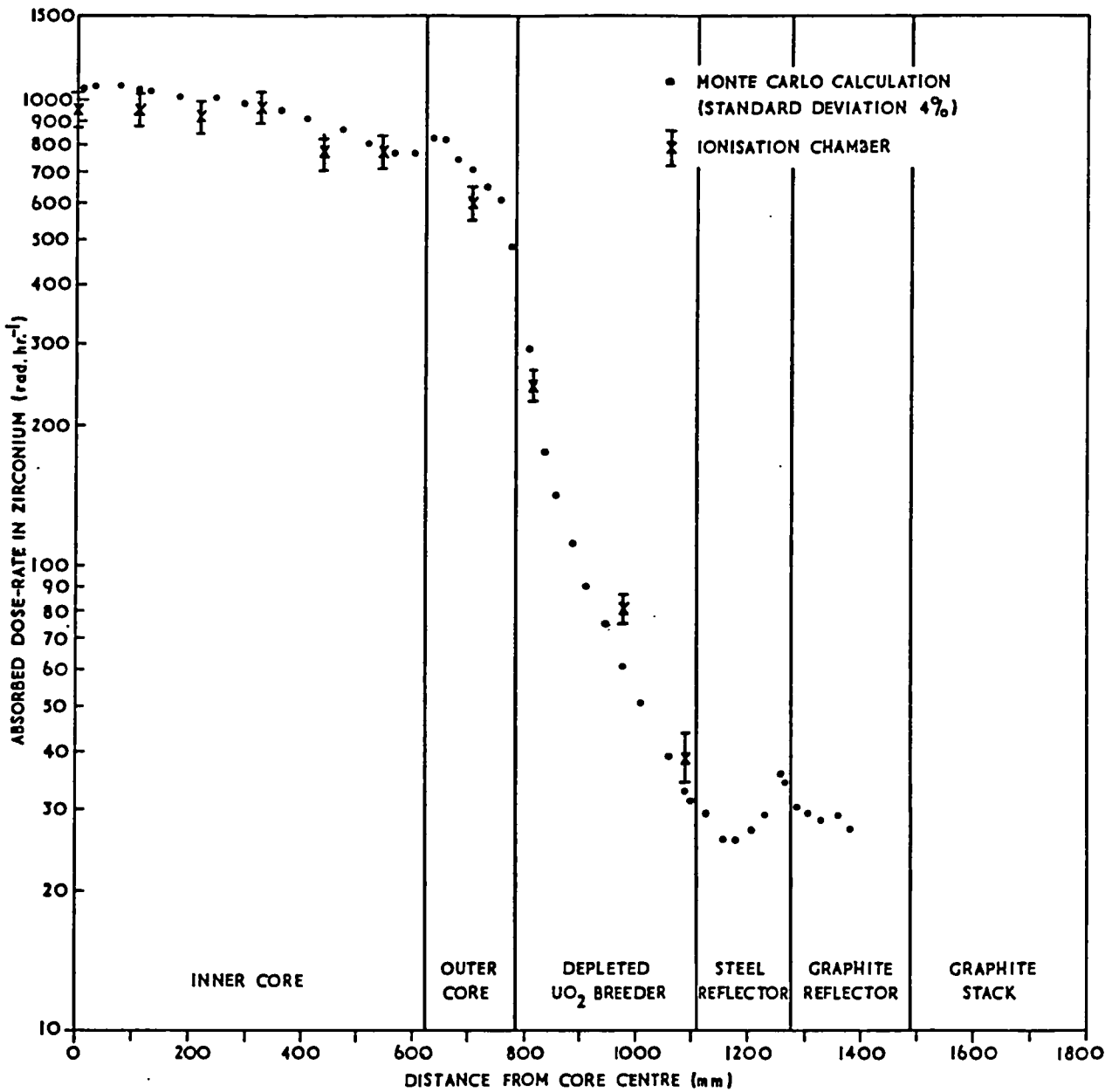
Comparison between the MZB calculations and measurements show that the TLD and ionisation chamber results are consistently lower than the calculated values in both radial and axial core scans. TLD measurements in the blanket regions show good agreement whereas the ionisation chamber results are too high, especially along the major axis (Figure 22). All the curves presented are the result of a continuous scan, apart from Figure 22 where the chamber measurements were made over a period of twelve weeks. Thus, the exceptionally high experimental value in the depleted  $UO_2$  breeder may in part be due to experimental error. The reason for the discrepancy between the axial calculations and measurements in the plenum (Figures 24,25), particularly in the lower aluminium region, is not clear. Representation of the plenum by the homogenised material is a possible source of error. However, it should be observed that the TLD measurements tend to confirm the dose-rate dip at the reflector boundary. This discrepancy does not influence the results in the breeder since the gamma-ray sources in the plenum make negligible contributions to the dose-rates in all but the last two points.

The ratio of the calculated and experimental values (C/E) from the MZC control rod mock-ups show good agreement in the core centre positions.

(Calculated values with and without the adjustment made due to the overestimate of the capture rate by diffusion theory are given.)

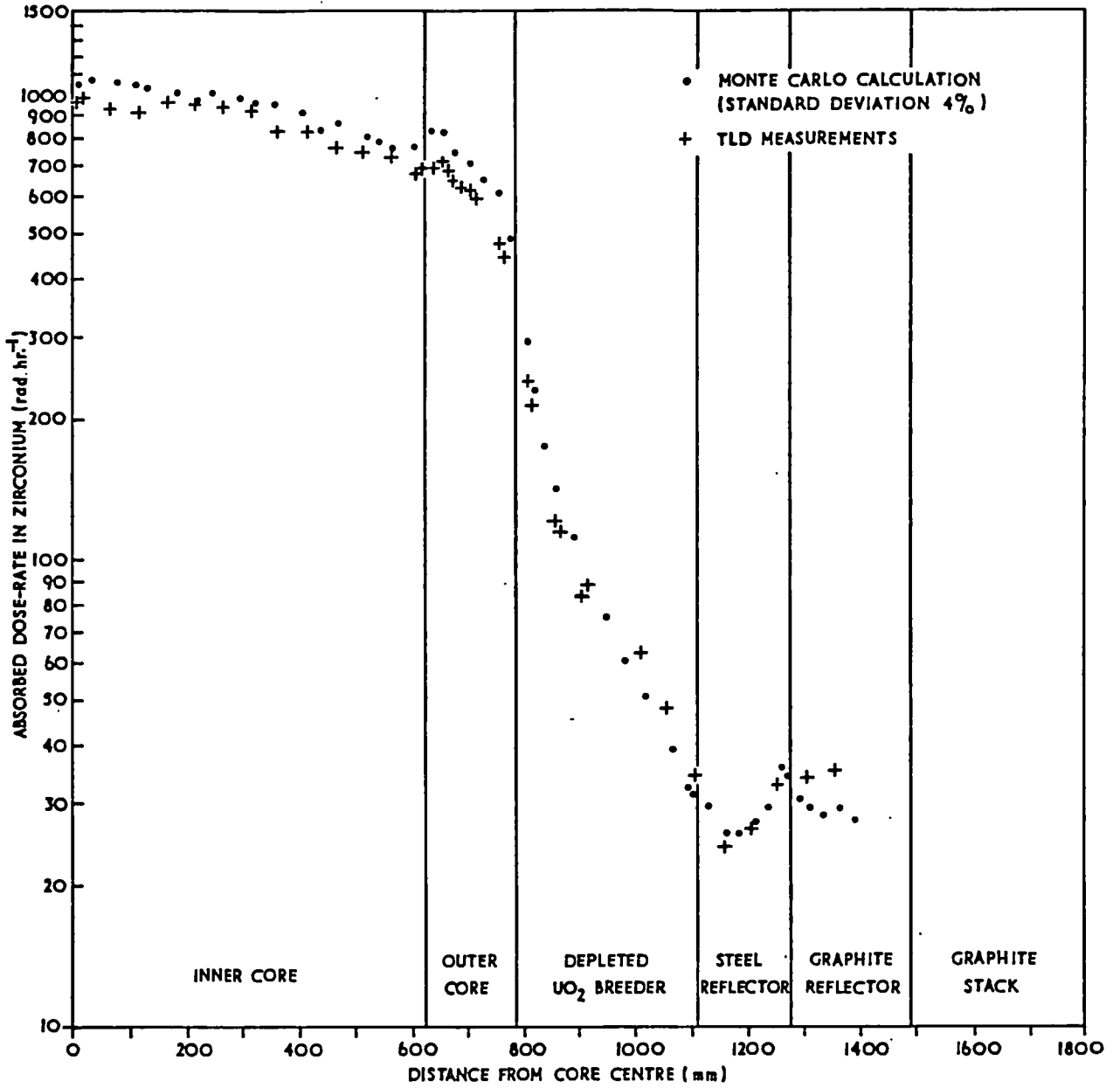
However, the outer core (S) tantalum control rod experimental result is very much higher than the predicted value ( $C/E = 0.66$ ). There are several factors which may account for this discrepancy and these were outlined in sub-section 6.2.1. The expected value can be approximately attained by comparing the change in dose-rate in the MZB core (Figure 22) between the two positions and this indicates that the experimental value is probably correct. It should be noted from Table 12 that the cavity correction is greater in the tantalum outer core position and this is due to a softer calculated photon spectrum. The softer spectrum is a result of the capture-rate in the homogenised position (S) calculation being relatively smaller than that in the central position. It is therefore concluded that the representation of the outer core control rod mock-up is not sufficiently detailed. Coupled with this factor is the large uncertainty in the Ta(S) normalisation factor.

---

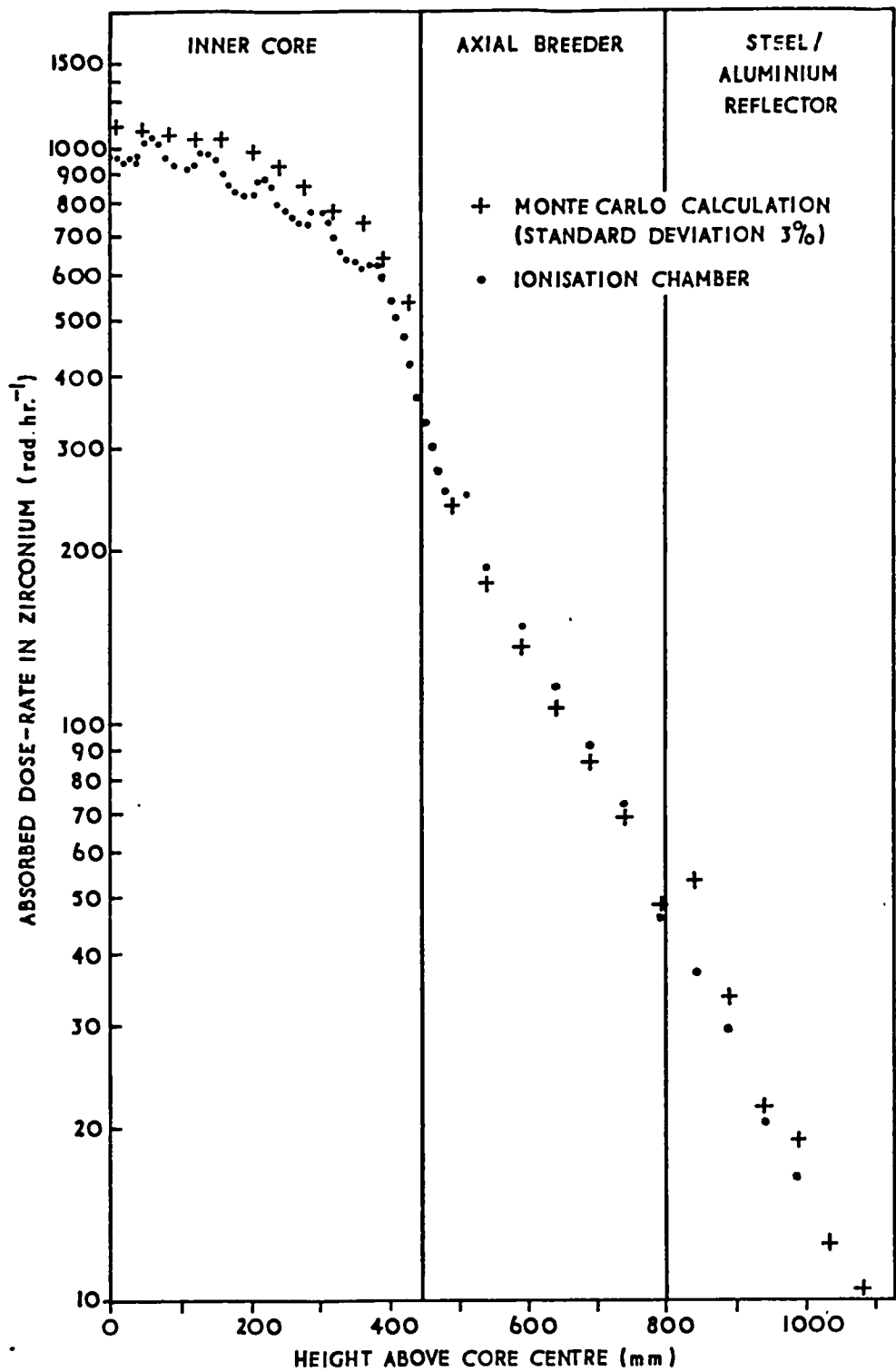


COMPARISON OF MONTE CARLO CALCULATION OF  
 ABSORBED DOSE-RATE AND IONISATION CHAMBER  
 MEASUREMENTS ALONG MAJOR AXIS OF ASSEMBLY MZB(2)

FIGURE 22

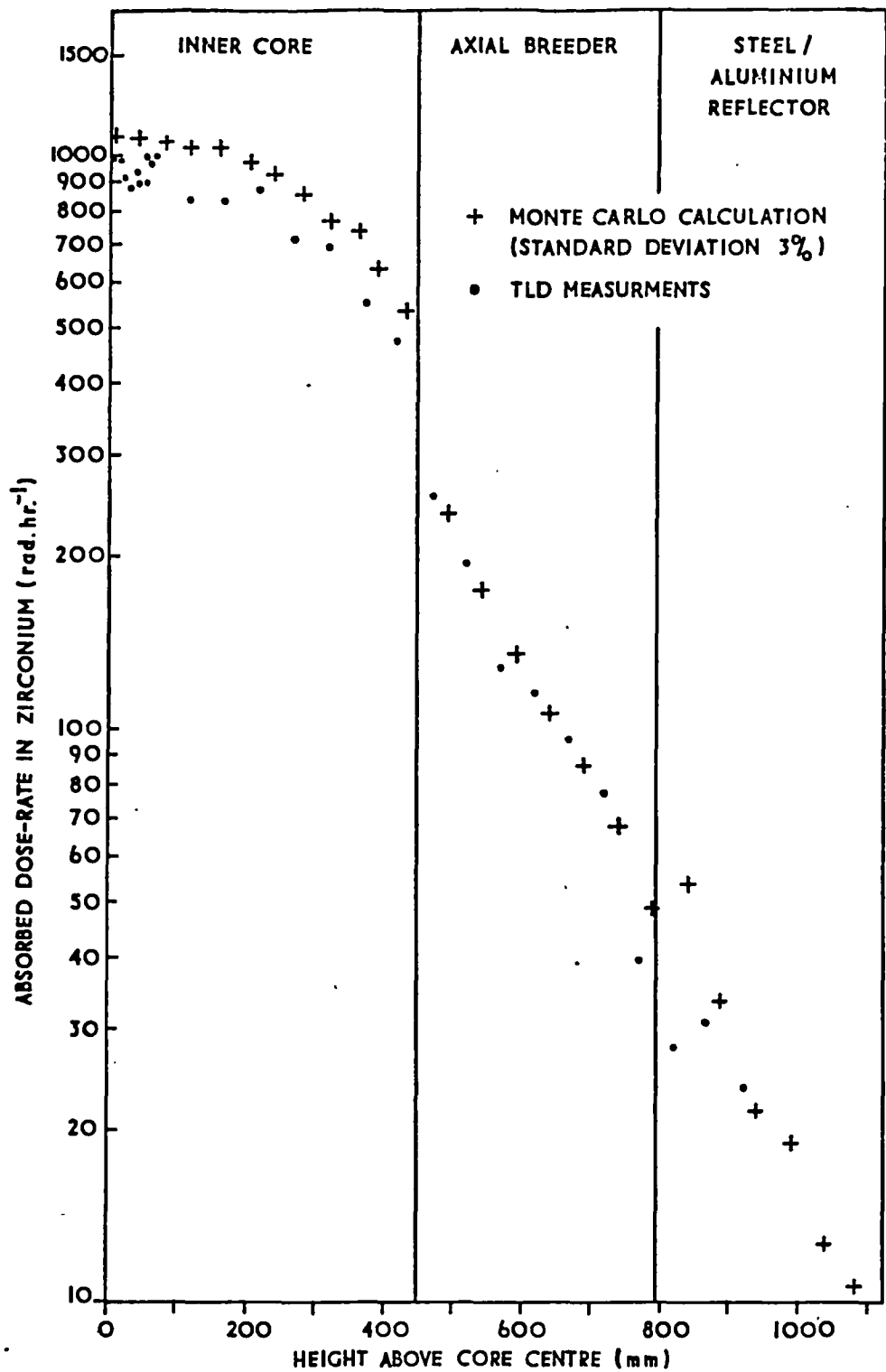


COMPARISON OF MONTE CARLO CALCULATION OF  
 ABSORBED DOSE-RATE AND TLD MEASUREMENTS  
 ALONG MAJOR AXIS OF ASSEMBLY MZB (2)  
 FIGURE 23



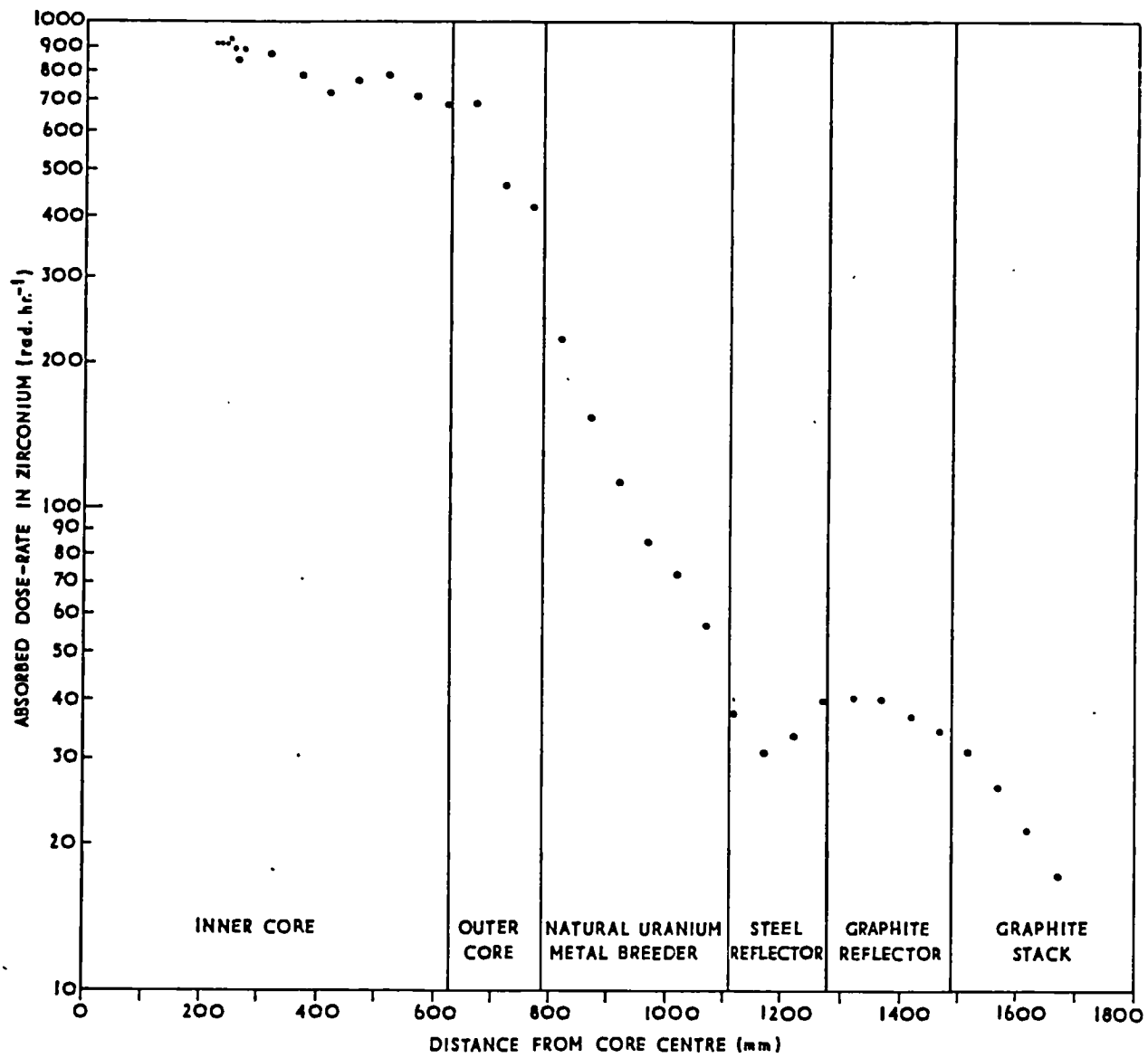
COMPARISON OF MONTE CARLO CALCULATION OF ABSORBED DOSE-RATE AND IONISATION CHAMBER MEASUREMENTS ALONG CENTRAL VERTICAL AXIS OF ASSEMBLY MZB (2)

FIGURE 24



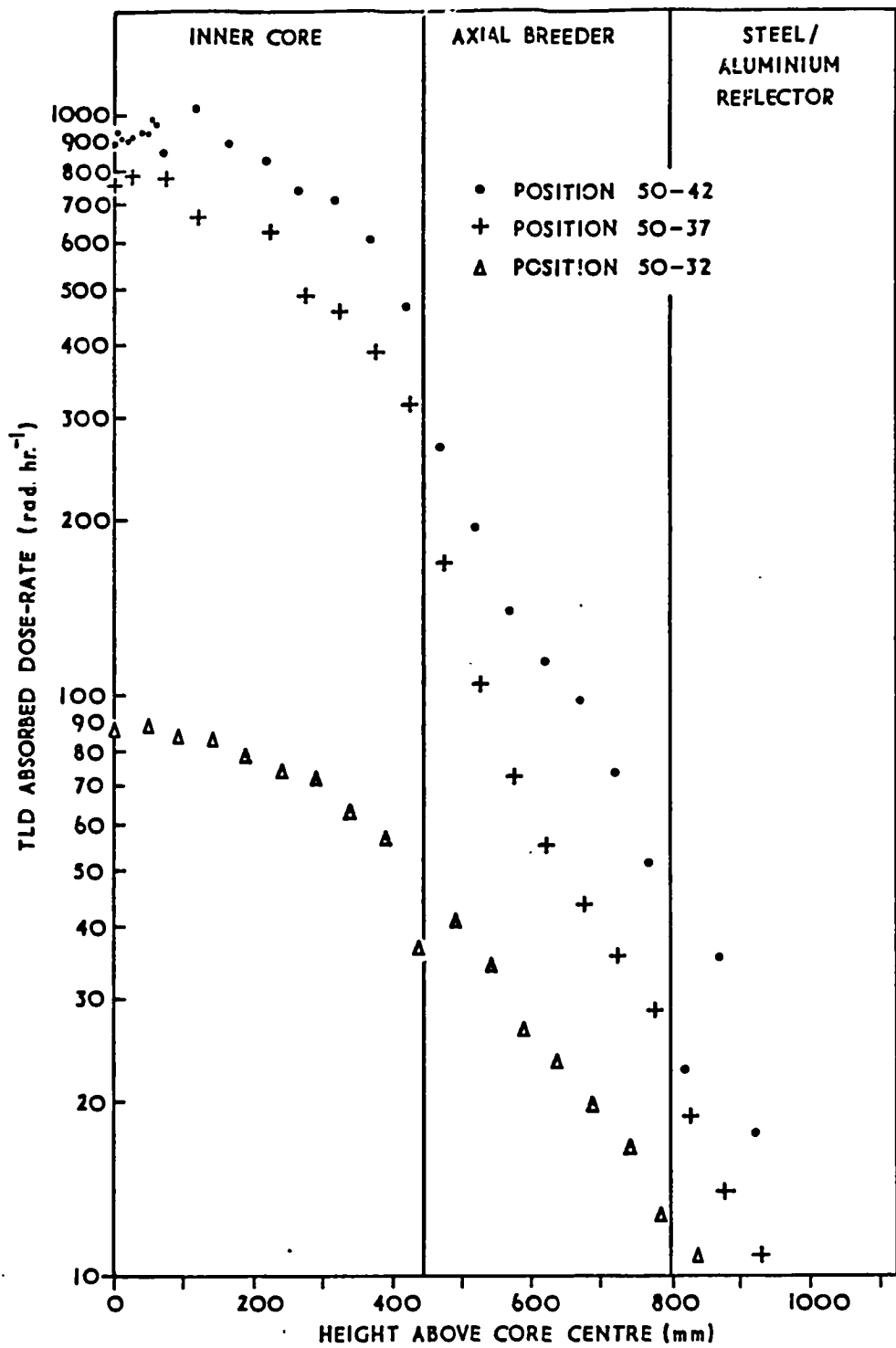
COMPARISON OF MONTE CARLO CALCULATION OF ABSORBED DOSE-RATE AND TLD MEASUREMENTS ALONG CENTRAL VERTICAL AXIS OF ASSEMBLY MZB(2)

FIGURE 25

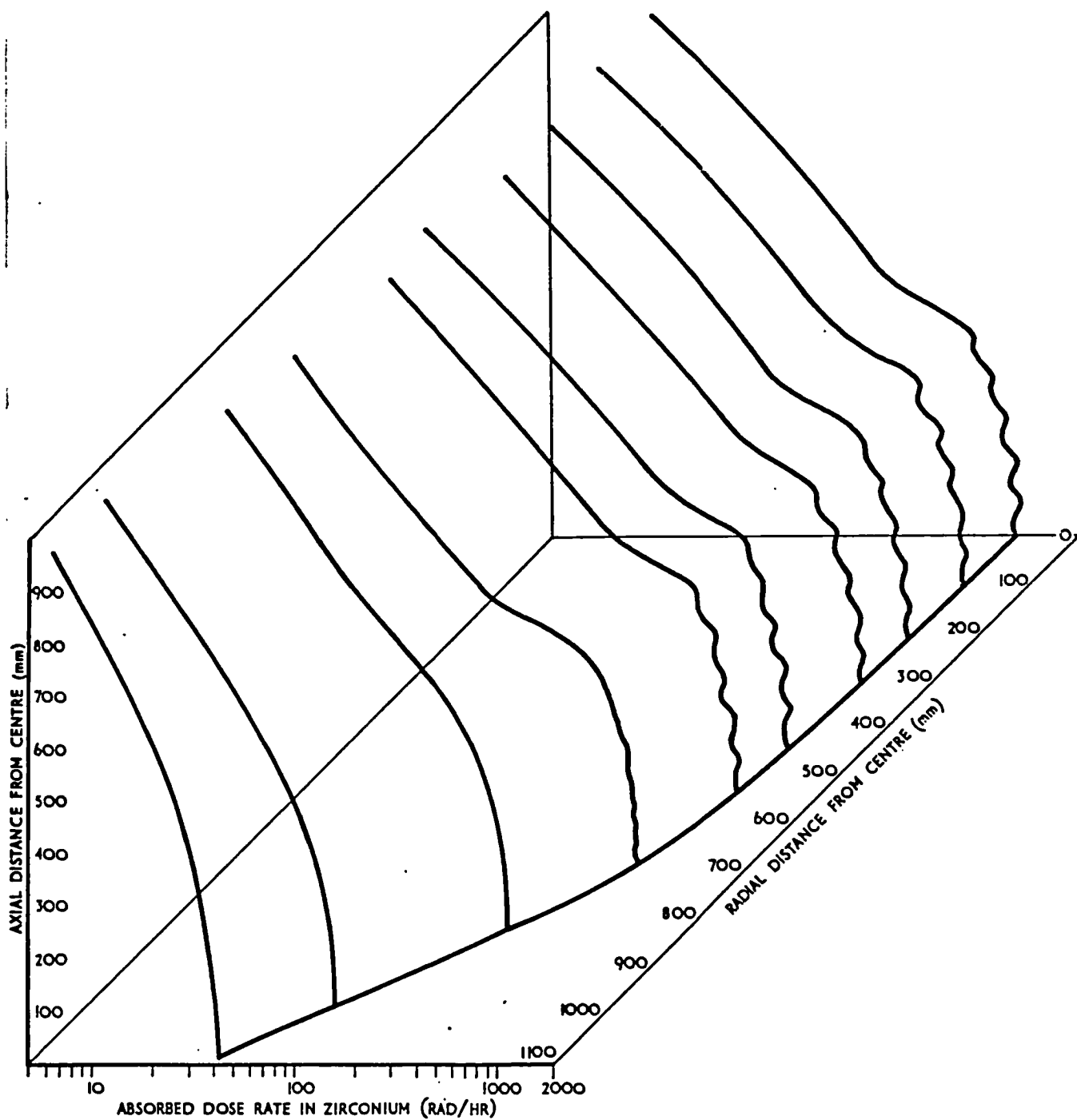


ABSORBED DOSE-RATE ALONG MAJOR AXIS  
 OF ASSEMBLY MZB (3) MEASURED WITH TLD.  
**FIGURE 26**





TLD AXIAL SCANS IN ASSEMBLY MZB (2)  
 (NO CAVITY CORRECTION APPLIED)  
 FIGURE 27



ZEBRA MZB GAMMA DOSE RATE DISTRIBUTION  
 FIGURE 28

Table 12

The MZC Results

Array	Start-up Time	Balance Time	Shut-Down Time	Calandria Removed from Core	Dose-Rates Corrected for Supralinearity and Neutron Sensitivity (rad hr <sup>-1</sup> )	PROCEED $\epsilon_w/\epsilon_c$	Cavity Corrected Dose-Rate (rad hr <sup>-1</sup> )	Calculated Dose-Rate (rad hr <sup>-1</sup> )	C/E	Calculated Values With Corrections for Neutron Capture Rates in the Absorber (rad hr <sup>-1</sup> )	C/E
Ta(O)	13.00	13.16	14.16	14.23	889 ± 10%	1.189 ± 2%	1057	1071 ± 4%	1.01	986	0.93
Ta(S)	14.32	14.51	15.51	15.58	509 ± 10%	1.347 ± 2%	686	456 ± 1%	0.66	420	0.61
B <sub>4</sub> C(O) Natural	18.27	18.48	19.48	19.56	376 ± 10%	0.990 ± 2%	372	356 ± 6%	0.96	351	0.94
B <sub>4</sub> C(O) Enriched	13.36	13.59	14.59	15.10	355 ± 10%	1.084 ± 2%	385	393 ± 5%	1.02	376	0.98

Table 13

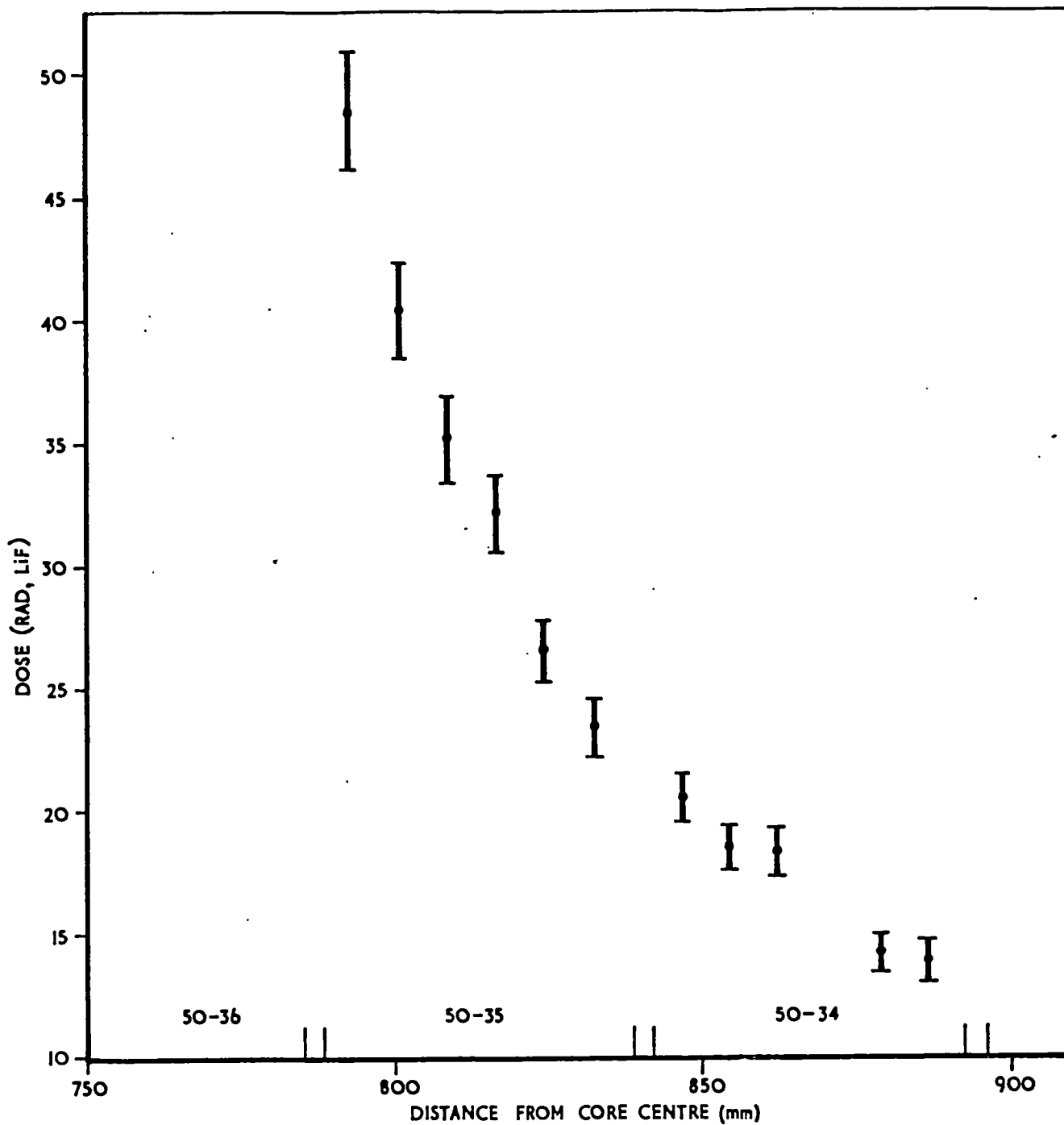
Gamma DMSA Pattern A

Pin Position	Pin Diameter (mm)	Material	Dose (rad, LiF)
A	7.0	Carbon	141.0 $\pm$ 7.1
B	7.0	Carbon	140.0 $\pm$ 7.0
C	7.0	Carbon	144.2 $\pm$ 7.2
D	6.96	Europium Oxide	329.0 $\pm$ 16.5
E	6.96	Europium Oxide	330.0 $\pm$ 16.5
F	6.96	Europium Oxide	324.0 $\pm$ 16.2
G	7.00	Stainless Steel	149.8 $\pm$ 7.5
H	12.70	Stainless Steel	144.8 $\pm$ 7.2
I	19.03	Boron Carbide (without liner)	158.8 $\pm$ 7.9
I	19.03	Boron Carbide (with liner)	169.7 $\pm$ 8.5
J	21.7	Carbon	137.6 $\pm$ 6.9

Table 14

Gamma DMSA Pattern B

Pin Position	Pin Diameter (mm)	Material	Dose (rad, LiF)
A	7.0	Carbon	141.3 $\pm$ 7.1
B	7.0	Carbon	141.6 $\pm$ 7.1
C	7.0	Carbon	141.1 $\pm$ 7.1
G	7.0	Stainless Steel	151.9 $\pm$ 7.6
H	12.70	Tantalum	235.1 $\pm$ 11.8
I	18.95	Tantalum	248.8 $\pm$ 12.4



OXIDE BREEDER RADIAL SCAN IN ASSEMBLY 13/5  
 FIGURE 29

## 7 CONCLUSIONS

The ZEBRA MZB dose-rate measurements have demonstrated that the procedures for the calculation of gamma-ray energy deposition in the fast reactor environment are generally satisfactory. The improved measurement techniques and source data for the calculations removed the large discrepancies that existed in previous studies. However, the over-estimation by approximately 10% for the calculated dose-rate in the core warrants further investigation. In the centre of a uniform core with no flux gradient, migration, and therefore the spectrum of photon sources, is unimportant. Errors in the calculated dose-rate can therefore be closely related to the gamma-ray energy released from epithermal fission. In the centre of the MZB core 83% of the dose-rate was due to uranium/plutonium sources of which 65% was due to fission. In addition to the core, the region where the dose-rate decreases by at least a factor of five within 200 mm of entering the breeder needs further examination - the recent Assembly 13/3 radial breeder scans will afford a useful check on this region. Capture in uranium in the breeder contributed 60% to the total dose-rate and the effect of changing the spectrum from that assumed for thermal capture to the more recent measurements for epithermal capture was small. The MZC control rod mock-up measurements in boron carbide and tantalum have established the feasibility of using TLD in this type of experiment; and, again, the more extensive study in the Assembly 13 DMSA will provide further information. It was unfortunate that the large discrepancy with the outer core tantalum control rod mock-up was not appreciated at the time of the Assembly 13 measurements to allow for a repeat experiment. One of the main objectives for the MZC study was to assess the suitability of the geometry models and it appears that the homogenisation of the

mock-up in the outer core situation was not satisfactory. Future work therefore involves gamma-ray codes with more general geometry capabilities. In addition, experience from the MOZART program and the associated studies have shown that the development of linked neutron-gamma codes and the setting up of permanent photon production data sets is desirable. Improvements in source data and the implementation of a reliable point-flux estimator are also essential.

There are several areas where the experimental techniques could be improved. More accurate and extensive calibration is required, and this applies to both the ionisation chambers and the TLD. The ionisation chamber was a valuable and sensitive instrument as was demonstrated in the MZB fine structure core scans. However, stability over a long period of time was a problem with the particular chambers and current measuring devices used. The attempt to measure the neutron sensitivity of the ionisation chambers provided evidence that some published W values (energy required by a recoil nucleus to produce one ion pair) are not reliable. The TLD technique has proved very satisfactory - good reproducible results can be achieved as long as the crystals are handled with care, and sufficient attention to detail is taken during the read-out stage. The TLD, when incorporated in the SSCD, gave a useful method of obtaining dose-rate scans while at power in ZEBRA, and the method proved suitable for measuring the energy deposition directly within materials. Neutron sensitivity of  $\text{Li}^7\text{F}$  is an outstanding problem and more experimental work is required to increase the limited data of its fast neutron response. Improved thermoluminescent materials, with better photon responses and less neutron sensitivity, are becoming available.

A major portion of this work was concerned with the calculation of the cavity correction - resulting in the Monte Carlo program for electron energy deposition within a cavity. The Monte Carlo predictions are in general agreement with those from the theory by Burlin although there are discrepancies which only experiments can resolve - in particular, for the energy region above that in the benchmark spectra for cavity and wall materials of widely differing atomic number. The program was written specifically for reactor energy deposition calculations, where computed spectra do not include the low energy photons from the photoelectric effect or bremsstrahlung photons, and it would be an advantage to handle these photons. A more general geometry capability would allow for different cavity shapes, non-homogeneous walls, and non-equilibria spectra to be treated. Other improvements that would extend the value of the Monte Carlo program include a more accurate representation of electron collisions (ie refining the continuous-slowing-down-model and the Molière theory of multiple scattering) and distinguishing between electrons and positrons.

Many of the difficulties in measuring and calculating gamma-ray energy deposition within a fast reactor have been examined. Although several problems have yet to be overcome, this work has demonstrated the capability of predicting the energy deposition to a satisfactory degree of confidence.



APPENDIX A

CALIBRATION SHEET FOR TYPE IG8 IONISATION CHAMBERS (MAY 1972)

(I) MASS ENERGY ABSORPTION COEFFICIENTS (CM<sup>2</sup>/G)

	CO60*	CS137
AIR	0.265045E-01	0.293760E-01
CARBON	0.266715E-01	0.292800E-01
ZIRCONIUM	0.238650E-01	0.293260E-01

(II) EXPOSURE - SOURCES AT 1 METRE (FARMER SUB-STANDARD)

CO60	0.293708E 03	ROENTGEN/HOUR
CS137	0.330507E 03	ROENTGEN/HOUR

(III) CURRENT (AMPS) - SOURCES AT 1 METRE (IG8)

	CO60	CS137
ZR/45/A/1	0.448000E-10	0.564000E-10
ZR/150/A/1	0.140000E-09	0.175000E-09
C/45/A/1	0.307000E-10	0.338000E-10
C/150/A/2	0.990000E-10	0.111000E-09
C/150/CO2/1	0.108000E-09	0.121000E-09

(IV) SENSITIVITY (AMPS/RAD/HOUR)

	CO60	CS137	MEAN
ZR/45/A/1	0.194940E-12	0.196706E-12	0.195823E-12
ZR/150/A/1	0.609186E-12	0.610347E-12	0.609767E-12
C/45/A/1	0.119529E-12	0.118069E-12	0.118799E-12
C/150/A/2	0.385453E-12	0.387743E-12	0.386598E-12
C/150/CO2/1	0.420494E-12	0.422675E-12	0.421584E-12

\* MEAN VALUES OF CO60 MASS ENERGY ABSORPTION COEFFICIENTS

## APPENDIX B

### IONISATION CHAMBER NEUTRON SENSITIVITY EXPERIMENT

#### B1 The Theory

The relationship between the dose-rate  $D$  and signal  $C_\gamma$  for a dosimeter calibrated in a pure gamma-ray field is given by:

$$D = C_\gamma / S_\gamma \quad - - - \quad (B1)$$

where  $S_\gamma$  is the dosimeter sensitivity to gamma-rays.

It is assumed that this relationship is valid in the reactor gamma-ray field. In the mixed gamma/neutron environment it is necessary to estimate the contribution to the signal from neutron interactions in order to obtain the true gamma-ray dose-rate. The dosimeter is usually designed to minimise the production of secondary particles from neutron interactions within the device itself, although this is not always possible.

In the ionisation chamber the major neutron response is due to recoil ions generated by scattering collisions with fast neutrons in the gas and surrounding wall and structural materials. The neutron corrected gamma-ray dose-rate ( $d_n$ ) is given by:

$$d_n = d_m - S_c N_c - S_w N_w \quad - - - \quad (B2)$$

where  $d_m$  is the apparent measured gamma-ray dose-rate;

$N_c$  is the neutron recoil dose-rate in the gas;

$N_w$  is the neutron recoil dose-rate in the wall;

$S_c$  is the relative sensitivity to the gas recoils;

$S_w$  is the relative sensitivity to the wall recoils.

Assuming that the optical diameter of the gas cavity is small compared

with the photon mean-free-path and large compared with the recoil nucleus mean-free-path then:

$$S_c = \frac{S_{cr}}{S_\gamma} \quad \text{where } S_{cr} \text{ is the chamber's sensitivity to the gas cavity recoils;}$$

$$= \frac{N_{cr}}{N_e} \quad \text{where } N_{cr} \text{ is the number of ion pairs produced by a gas recoil nucleus;}$$

$N_e$  is the number of ion pairs produced by a secondary electron induced by a photon;

- - - (B3)

$$= \frac{W_e}{W_{cr}} \quad \text{where } W_e \text{ is the average energy required by an electron to produce one ion pair;}$$

$W_{cr}$  is the average energy required by a gas cavity recoil nucleus to produce one pair.

$S_c$  is therefore independent of chamber pressure.  $S_w$ , however, is inversely proportional to chamber pressure because although the chamber's sensitivity to the wall recoils ( $S_{wr}$ ) is independent of pressure (wall recoils are stopped very close to wall)  $S_\gamma$  is proportional to pressure.

Defining a pressure independent sensitivity to photons ( $S_\gamma'$ ):

$$S_\gamma' = S_\gamma/p \quad \text{where } p \text{ is the chamber gas pressure}$$

then

$$S_w = \frac{S_w'}{p} \quad \text{where } S_w' = \frac{S_{wr}}{S_\gamma'} \quad \text{- - - (B4)}$$

(ie  $S_w'$  is pressure independent sensitivity to wall recoils).

Consider making a measurement in a reactor with three chambers of identical wall materials but with the gas fillings as follows:

Chamber 1, gas type a at pressure  $p_1$

Chamber 2, gas type a at pressure  $p_2$

Chamber 3, gas type b at pressure  $p_1$

In equation (B2), the quantities  $S_c$ ,  $N_c$  and  $d_n$  are common to the measurements made with chambers 1 and 2:

$$\begin{aligned} \therefore d_{m_2} - d_{m_1} &= S_{w_2} N_{w_2} - S_{w_1} N_{w_1} \\ &= \frac{S_{w_2}'}{p_2} N_{w_2} - \frac{S_{w_1}'}{p_1} N_{w_1} \end{aligned} \quad \text{--- (B5)}$$

As both chambers possess identical walls and gas type  $N_{w_1} = N_{w_2}$  and

$$S_{w_1}' = S_{w_2}'$$

$$\therefore d_{m_2} - d_{m_1} = S_w' N_w \left[ \frac{1}{p_2} - \frac{1}{p_1} \right] \quad \text{--- (B6)}$$

Assuming that  $S_w$  is independent of the gas type (equation B15) then

$S_w N_w$  and  $d_n$  are common to the measurements made with chambers 1 and 3:

$$\therefore d_{m_3} - d_{m_1} = S_{c_b} N_{c_b} - S_{c_a} N_{c_a} \quad \text{--- (B7)}$$

Assuming that  $S_c$  is independent of the gas type (equation B16) then:

$$S_c = \frac{d_{m_3} - d_{m_1}}{N_{c_b} - N_{c_a}} \quad \text{--- (B8)}$$

Thus, substituting equations (B6) and (B8) in equation (B2):

$$d_n = d_{m_1} - (d_{m_3} - d_{m_1}) \left( \frac{N_{c_b}}{N_{c_a}} - 1 \right)^{-1} - \frac{p_2}{p_1 - p_2} (d_{m_2} - d_{m_1}) \quad \dots \quad (B9)$$

It can be shown [61] that the total energy lost per  $\text{cm}^3$  per second by a neutron of energy  $E$  is:

$$E_n = \frac{2A}{(1+A)^2} \int_{E_1}^{E_u} E \Phi(E) \Sigma_s(E) [1 - \bar{u}(E)] dE \quad \text{MeV cm}^{-3} \text{ sec}^{-1} \quad \dots \quad (B10)$$

where  $A$  is the atomic weight;

$\Phi(E)$  is the neutron flux;

$\Sigma_s(E)$  is the macroscopic elastic scattering cross-section;

$\bar{u}(E)$  is the average cosine of the scattering angle in the centre-of-mass system.

The neutron dose-rate is given by

$$N_c = \frac{k E_n}{\rho} \text{ rad hr}^{-1}$$

where  $k$  is the unit constant defined in sub-section 2.4.2;

$\rho$  is the density ( $\text{g cm}^{-3}$ )

$$\therefore N_c = \frac{2kN_A}{(1+A)^2} \int_{E_1}^{E_u} E \Phi(E) \sigma_s(E) [1 - \bar{u}(E)] dE \quad \dots \quad (B11)$$

where  $N_A$  is the Avagadro constant;

$\sigma_s$  is the microscopic elastic scattering cross-section.

## B2 The Experiments

The neutron sensitivity in the ZEBRA MZB(2) assembly was investigated by making measurements with three carbon-walled, type IG8, ionisation

chambers with gas fillings as follows:

Chamber 1, Ar gas at 1500 mm Hg pressure

Chamber 2, Ar gas at 450 mm Hg pressure

Chamber 3, CO<sub>2</sub> gas at 1500 mm Hg pressure

Table B1 gives the neutron recoil dose-rates in materials of interest calculated using equation (B11) at three measurement positions. The neutron fluxes were obtained from the RZ GOG calculations (sub-section 6.3.4) and the nuclear data mainly from the UK Library.

Table B1

Calculated Neutron Recoil Dose-Rates (rad hr<sup>-1</sup>) at the MZB Centre Plane

Material	MZB Core Position		
	Core Centre (50-50)	Inner Core (50-42)	Mid-Depleted Blanket (50-32)
Zr	46	38	3
Ar	87	72	4
CO <sub>2</sub>	1162	956	78
C	1548	1272	105
Li <sup>7</sup> F	1062	874	67

The chamber's sensitivity to recoils from the carbon wall was calculated from equation (B6) using the experimental results and the calculated neutron recoil dose-rates given in Table B1. At the core centre position  $S_{wr} = 9.994 \times 10^{-15}$  amps/rad hr<sup>-1</sup> and thus  $S_w$  for chamber 2 is 0.084. Assuming this relative sensitivity can be approximately applied to the zirconium-walled chamber used in the ZEBRA scans the correction necessary for wall recoils is less than 0.4%. The wall correction can therefore be neglected and equation (B2) becomes:

$$d_n = d_m - S_c N_c \quad - - - \quad (B12)$$

The chamber's relative sensitivity to cavity recoils was calculated from equation (B8) using the experimental values and the calculated neutron recoil dose-rates given in Table B1. The results are given in Table B2 for the three measurement positions and are called  $S_c(\text{expt.})$ . It will, however, be remembered that two assumptions were made in deriving equation (B8) and these will now be discussed.

### B3 Discussion of the Assumptions

As previously shown (equation B3)  $S_c = W_e/W_{cr}$  and therefore an independent check on  $S_c(\text{expt.})$  can be provided. The average energy dissipated in a gas per ion pair produced depends upon the ionising particle and the gas.  $W_e$  is not a function of energy and the values for Ar and  $\text{CO}_2$  have been taken from Myers [62]. However,  $W_{cr}$  is not constant with particle energy and it is therefore necessary to obtain a mean value:

$$\bar{W}_{cr} = \frac{\int E \phi(E) \sigma_s(E) [1 - \bar{u}(E)] dE}{\int E \phi(E) \sigma_s(E) [1 - \bar{u}(E)] / W_{cr}(E_r) dE} \quad \text{--- (B13)}$$

where  $E_r$  is the recoil energy given by:

$$E_r = \frac{2AE}{(1+A)^2} [1 - \bar{u}(E)] \quad \text{--- (B14)}$$

Dennis [63, 64] has examined the variation of  $W_{cr}$  with initial particle energy. The empirical formulae and data given in the latest paper by Dennis were used to calculate  $W_{cr}$  for  $\text{C}^+$  and  $\text{O}^+$  recoils in  $\text{CO}_2$ . Data for argon was not available in that paper and therefore the empirical relationships in Reference [64] were used to calculate  $W_{cr}$  for  $\text{Ar}^+$  recoils in argon. The mean values for  $W_{cr}$  were obtained using equation (B13) with the data already described. The results are given in Table B2. The first assumption made in relation to these chamber

measurements was as follows:

$$\frac{W_e}{\bar{W}_{wr}} \text{ for } C^+ \text{ recoils in } CO_2 = \frac{W_e}{\bar{W}_{wr}} \text{ for } C^+ \text{ recoils in Ar} \quad - - - (B15)$$

This appeared to be valid as Dennis's latest work showed that the average energy required by a recoil nucleus to produce one ion pair was dependent only on the recoil ion and not the gas type. The second assumption was:

$$\frac{W_e}{\bar{W}_{cr}} \text{ for } C^+, O^+ \text{ recoils in } CO_2 = \frac{W_e}{\bar{W}_{cr}} \text{ for } Ar^+ \text{ recoils in Ar} \quad - - - (B16)$$

Table B2

Experimental and Calculated Values for  $S_c$

$S_c$	MZB Core Position		
	Core Centre (50-50)	Inner Core (50-42)	Mid-Depleted Breeder (50-32)
$S_c$ (expt.)	0.36	0.36	0.31
$S_c$ (calc.) Ar <sup>+</sup> in Ar	0.34	0.34	0.31
$S_c$ (calc.) O <sup>+</sup> in CO <sub>2</sub>	0.68	0.68	0.59
$S_c$ (calc.) C <sup>+</sup> in CO <sub>2</sub>	0.60	0.60	0.52

From the values of  $S_c$  (calc.) in Table B2 the validity of (B16) was in doubt. However, if the calculated values were correct it would have been expected for  $S_c$  (expt.) to be closer to the values for CO<sub>2</sub> (equation B7). It therefore appeared that  $\bar{W}_{cr}$  for oxygen and carbon recoils in CO<sub>2</sub> was being underestimated by approximately a factor of two. Due to the uncertainty in the procedure for obtaining an experimental value for



the neutron sensitivity, a calculated correction was applied to the dose-rate scans made with the zirconium-walled, argon-filled ionisation chamber.

---

## APPENDIX C

### THE MONTE CARLO PROGRAM PROCEED

#### C1 Definitions

Terms used in this appendix are defined below and symbols are listed in Appendix D.

- C1.1 Electrons and positrons generated by photon interactions are treated identically - this is discussed in more detail in subsection C2.1.3 - and are referred to as "particles" throughout.
- C1.2 A "cavity" is the volume occupied by a detecting medium during a measurement of gamma-ray energy deposition.
- C1.3 The "wall" is the medium surrounding the cavity in which the gamma-ray energy deposition per unit mass is required.
- C1.4 The "wall contribution volume" is the wall region which can supply particles to the cavity. The boundaries of the wall contribution volume are defined by the maximum range of the most energetic particles generated by the photon interactions.
- C1.5 The "cavity correction" is the ratio of the energy deposited per unit mass in the cavity when it contains the wall medium to the energy deposited per unit mass in the cavity when it contains the detecting medium.
- C1.6 The term "standard gamma-ray programs" refers to programs which assume the particle energy is deposited at the site of the photon interaction, which is either a photoelectric, Compton or pair-production interaction. The computed spectra from such a program consists only of source, Compton and two-quanta annihilation

photons. The binding energy loss in the photoelectric effect is ignored and bremsstrahlung losses are not included. Two-quanta annihilation of the pair-production positron only takes place when the positron has come to rest, and annihilation with the emission of a single photon is ignored.

## C2 Description of the Program

The Monte Carlo program which calculates the cavity correction is called PROCEED (Photon Response Of Cavity Electron Energy Deposition).

The relationship between the measured energy deposition per unit mass ( $E_c$ ) and the required energy deposition per unit mass in the wall medium ( $E_w$ ) is given by:

$$E_w = \frac{\epsilon_w}{\epsilon_c} E_c \quad - - - \quad (C1)$$

where  $\epsilon_w/\epsilon_c$  is the cavity correction to be calculated.

The energy deposition in the cavity is from particles generated both in the contribution volume and within the cavity itself.

$$\frac{\epsilon_w}{\epsilon_c} = \frac{\epsilon_{w_e} + \epsilon_{w_i}}{\epsilon_{c_e} + \epsilon_{c_i}} \quad - - - \quad (C2)$$

where  $\epsilon_{w_e}$  is the energy per unit mass deposited in the cavity filled with the wall medium from particles generated in the wall (external);

$\epsilon_{c_e}$  is the energy per unit mass deposited in the cavity filled with the detecting medium from particles generated in the wall (external);

$\epsilon_{w_i}$  is the energy per unit mass deposited in the cavity filled

with the wall medium from particles generated in the cavity (internal);

$\epsilon_{c_i}$  is the energy per unit mass deposited in the cavity filled with the detecting medium from particles generated in the cavity (internal).

For a small cavity where there are few interactions in the cavity itself:

$$\frac{\epsilon_w}{\epsilon_c} \rightarrow \frac{\epsilon_{w_e}}{\epsilon_{c_e}} \quad - - - (C3)$$

For a large cavity where the wall contribution is negligible:

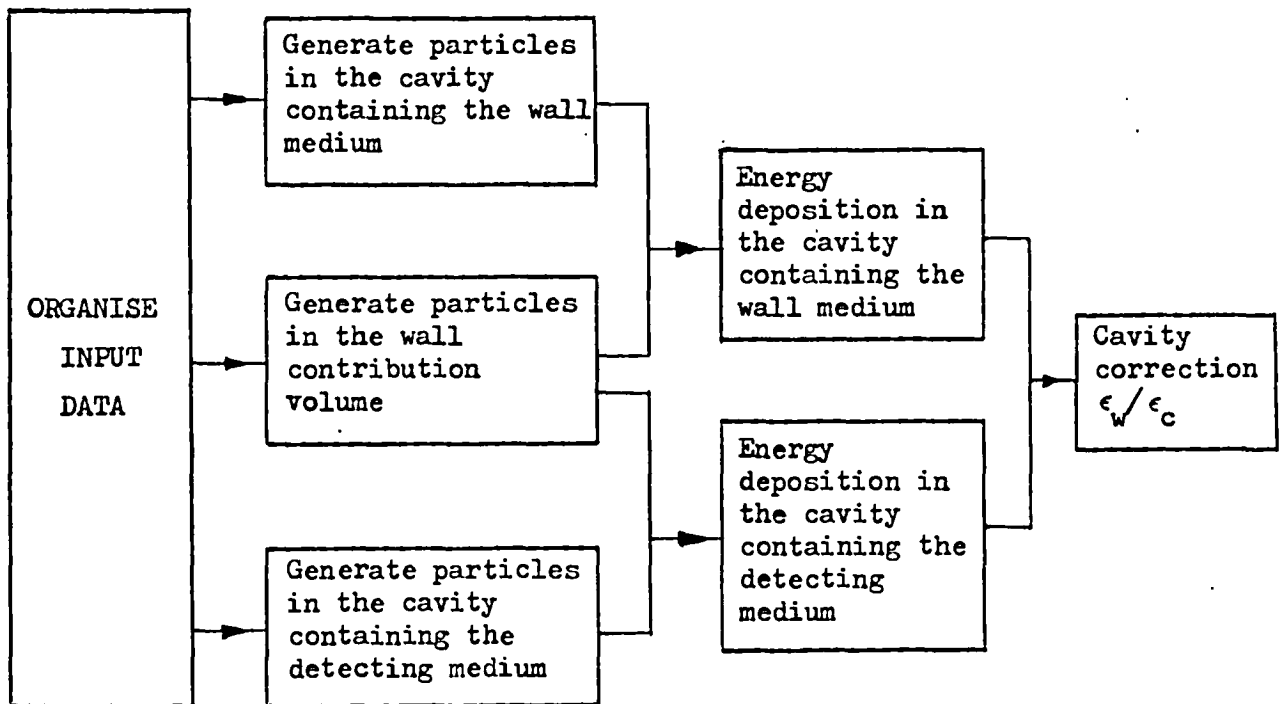
$$\frac{\epsilon_w}{\epsilon_c} \rightarrow \frac{\epsilon_{w_i}}{\epsilon_{c_i}} \quad - - - (C4)$$

A schematic of the program PROCEED is given in Figure C1. Particles are first generated in the wall contribution volume and in the cavity containing the wall medium (details in sub-section C2.4). As these particles cross the cavity the energy deposition is scored (C2.3) giving  $\epsilon_{w_e}$  and  $\epsilon_{w_i}$ . Using the identical wall particles, but with a new particle source spectrum generated for the detecting medium in the cavity,  $\epsilon_{c_e}$  and  $\epsilon_{c_i}$  are computed. The particles are generated with a uniform spatial distribution and the direction is chosen from an isotropic angular distribution. Because of the immense number of collisions an electron undergoes in slowing down it is not possible to represent every individual collision. For example, a 0.5 MeV electron in gold requires approximately  $1.7 \times 10^5$  collisions to lose half its energy. Therefore in an electron Monte Carlo program it is necessary to group many steps of the real physical random walk into a single step to

give a "condensed" random walk. In PROCEED the average energy deposition in each step is calculated from the continuous-slowing-down-model (C2.1.3). The multiple scattering angular distribution used is discussed in sub-section C2.3.

FIGURE C1

A SCHEMATIC OF THE PROGRAM PROCEED



### C2.1 Organisation of the Input Data

C2.1.1 "Effective values" for materials are calculated using Bragg's additivity rule [34]:

$$\bar{Z}/A = \sum_j w_j \left( \frac{Z_j}{A_j} \right) \quad \text{--- (C5)}$$

where Z is the atomic number;

A is the atomic weight,

$w_j$  is the fraction by weight of the  $j$ th element of a material

$$\ln I = \sum_j w_j \left( \frac{Z_j}{A_j} \right) \ln I_j / \bar{Z}/A \quad - - - \quad (C6)$$

where  $I$  is the mean excitation potential of an atom (see equation (C8)).

C2.1.2 In order to randomly select a photon of energy  $E_\gamma$  from the input group photon flux it is necessary to compute group reaction rates. Photon interaction cross-sections are obtained from a modified version of the HEITLER subroutine [43] which uses the Hubbel data [11] as the reference set. The ratio of the number of photon interactions in the cavity containing the detecting medium,  $N_{c_{det}}$ , and the wall medium,  $N_{c_{wall}}$ , is given by:

$$\frac{N_{c_{det}}}{N_{c_{wall}}} = \frac{\int \Phi(E_\gamma) \mu_{det}(E_\gamma) dE_\gamma}{\int \Phi(E_\gamma) \mu_{wall}(E_\gamma) dE_\gamma} \quad - - - \quad (C7)$$

where  $\Phi(E_\gamma)$  is the photon flux at energy  $E_\gamma$ ;

$\mu_{det}(E_\gamma)$  is the macroscopic cross-section in the detecting medium at energy  $E_\gamma$ ;

$\mu_{wall}(E_\gamma)$  is the macroscopic cross-section in the wall medium at energy  $E_\gamma$ .

C2.1.3 The preliminary part of the program also creates electron energy deposition data sets for the wall medium and detecting medium which are referred to throughout the tracking processes. The mean inelastic collision loss is given by the Bethe equation

for electrons using the formulation of Bichsel [34]:

$$\frac{-dT}{ds} = \frac{0.1535\rho}{\beta^2} \left( \frac{Z}{A} \right) \left\{ \ln \left[ \frac{2(T_m + 2)}{(I/m_0 c^2)^2} \right] + F^-(T_m, \Delta) - \delta \right\} \text{ MeV cm}^{-1} \quad \text{--- (C8)}$$

where  $F^- = -1 - \beta^2 + \ln [(T_m - \Delta)\Delta] + [T_m/(T_m - \Delta)] + \frac{\frac{1}{2}\Delta^2 + (2T_m + 1)\ln[1 - \Delta/T_m]}{(T_m + 1)^2}$

$\beta$  is the ratio of the particle velocity  $v$  to the velocity of light;

$m_0 c^2$  is the energy equivalent of electron mass = 511006 eV;

$T_m$  is the electron energy in  $m_0 c^2$  units;

$I$  is the mean excitation potential (eV);

$\delta$  is the correction for the polarisation of the medium by the charged particle;

$\Delta$  is the delta-ray cut off energy in  $m_0 c^2$  units;

$$\beta^2 = \frac{T_m^2 + 2T_m}{(T_m + 1)^2}$$

A large energy transfer in a single collision results in an energetic secondary electron (delta-ray).  $\Delta$  is the maximum energy, in  $m_0 c^2$  units, given to a delta-ray. The formulation of the equation (C8) and the nondistinguishability of the electrons after collision limits the energy transfer to  $T_m/2$ . Modern cavity theories [33, 65] treat the delta-rays separately arguing that some energy is carried away from the collision site by these energetic electrons. This is not particularly relevant to this work as the mean chord length of the  $\text{Li}^7\text{F}$  crystals is  $0.242 \text{ g cm}^{-2}$  which corresponds to an electron energy of approximately 0.7 MeV. The ratio of the radiative to

collision loss is given approximately [66] by:

$$\frac{(dT/ds)_{\text{rad}}}{(dT/ds)_{\text{col}}} = \frac{ZE_{\gamma_m}}{1600} \quad - - - \quad (C9)$$

where  $E_{\gamma_m}$  is the photon energy in  $m_0 c^2$  units. However, as the photon spectrum from the standard gamma-ray programs does not include bremsstrahlung losses, this has been neglected.

The derivation of a mean energy loss equation for positrons is very similar to that for electrons. However, the upper limit of energy transfer is now  $\Delta = T_m$  as the electron and positron are distinguishable and the electron-electron Møller cross-section must be replaced by the electron-positron Bhabha cross-section. These cross-sections are compared in Reference [6]. The changes alter the expression for  $F^-$  in equation (C8) to the expression for  $F^+$  in Reference [34]. In this work positrons created during pair-production are treated as electrons but a useful addition to PROCEED would be to treat the positron energy deposition separately.

From equation (C8) the electron energy deposition data sets are compiled as follows:

$$\frac{dT}{ds} = -f(T) \quad - - - \quad (C10)$$

$$s = \int_{T_f}^{T_i} \frac{dT}{f(T)} \quad \text{where } T_i \text{ is the initial electron energy;}$$

$$T_f \text{ is the final electron energy.}$$

$$= \int_{T_f}^{T_{\text{max}}} \frac{dT}{f(T)} - \int_{T_i}^{T_{\text{max}}} \frac{dT}{f(T)} \quad \text{where } T_{\text{max}} \text{ is defined below.}$$



$$\text{Let } g(T) = \int_T^{T_{\max}} \frac{dT}{f(T)} \quad \text{--- (C11)}$$

$$g(T_f) = g(T_i) + s \quad \text{--- (C12)}$$

Equation (C8) is not valid for small electron energies and is applied until the electron energy is reduced to 10 KeV after which the energy is deposited "on the spot". Thus  $g(T)$  is computed at 500 values between  $T = 10$  KeV to  $T_{\max}$  which is the maximum electron energy produced by the input photon spectrum. A smooth curve fit by a cubic spline is made to the 500 values of  $g(T)$  and the energy deposition data set consists of the knot positions, the values of the spline at the knots, and the first derivative of the spline at each knot.

## C2.2 Generation of a Charged Particle

From an input photon spectrum PROCEED generates uniformly distributed particle source spectra in the wall medium and detecting medium. These spectra are a function of the photon spectrum and the relevant macroscopic photon interaction cross-sections. For a photoelectric interaction it is assumed that all the photon energy is transferred to the electron in order to be consistent with standard gamma-ray programs (ie  $T_- = E_\gamma$ ). For the Compton effect the recoil electron energy is taken from the distribution given below [67]:

$$N_{\text{com}}(T_-) = \frac{\pi r_0 m_0 c^2}{E_\gamma^2} \left\{ 2 + \left( \frac{T_-}{E_\gamma - T_-} \right)^2 \left[ \frac{m_0^2 c^4}{E_\gamma^2} + \frac{(T_- - 2m_0 c^2)(E_\gamma - T_-)}{E_\gamma T_-} \right] \right\} \quad \text{--- (C13)}$$

where  $r_0$  is the classical electron radius;

$E_\gamma, T_-$  are in eV.

The maximum electron energy (Compton edge) is given by:

$$T_{-}(\max) = \frac{E_{\gamma}}{1 + \frac{m_0 c^2}{2E_{\gamma}}} \quad \text{eV} \quad \text{--- (C14)}$$

The Bethe-Heitler pair-production distribution [66] is used to obtain the electron and positron kinetic energies:

$$N_{PP}(E_{+}) = Z^2 r_0^2 \alpha \frac{P_{+} P_{-}}{E_{\gamma m}^3} \left\{ -\frac{4}{3} - 2E_{+} E_{-} \left( \frac{P_{+}^2 + P_{-}^2}{P_{+}^2 P_{-}^2} \right) + \frac{K_{-} E_{+}}{P_{-}^3} + \frac{K_{+} E_{-}}{P_{+}^3} - \frac{K_{+} K_{-}}{P_{+} P_{-}} + L \right.$$

$$\left. \left[ -\frac{8}{3} \frac{E_{+} E_{-}}{P_{+} P_{-}} + \frac{E_{\gamma m}^2 (E_{+}^2 E_{-}^2 + P_{+}^2 P_{-}^2)}{P_{+}^3 P_{-}^3} - \frac{E_{\gamma m}}{2P_{+} P_{-}} \left( \left( \frac{E_{+} E_{-} - P_{-}^2}{P_{-}^3} \right) K_{-} + \left( \frac{E_{+} E_{-} - P_{+}^2}{P_{+}^3} \right) K_{+} + \frac{2E_{\gamma m} E_{+} E_{-}}{P_{+}^2 P_{-}^2} \right) \right] \right\}$$

$$\text{where } K_{+} = \ln \left[ \frac{E_{+} + P_{+}}{E_{+} - P_{+}} \right]; \quad K_{-} = \ln \left[ \frac{E_{-} + P_{-}}{E_{-} - P_{-}} \right]; \quad L = 2 \ln \left[ \frac{E_{+} E_{-} + P_{+} P_{-} + 1}{E_{\gamma m}} \right] \quad \text{--- (C15)}$$

$$E_{+}^2 = P_{+}^2 + 1, \quad E_{-}^2 = P_{-}^2 + 1, \quad E_{\gamma m} = E_{+} + E_{-}$$

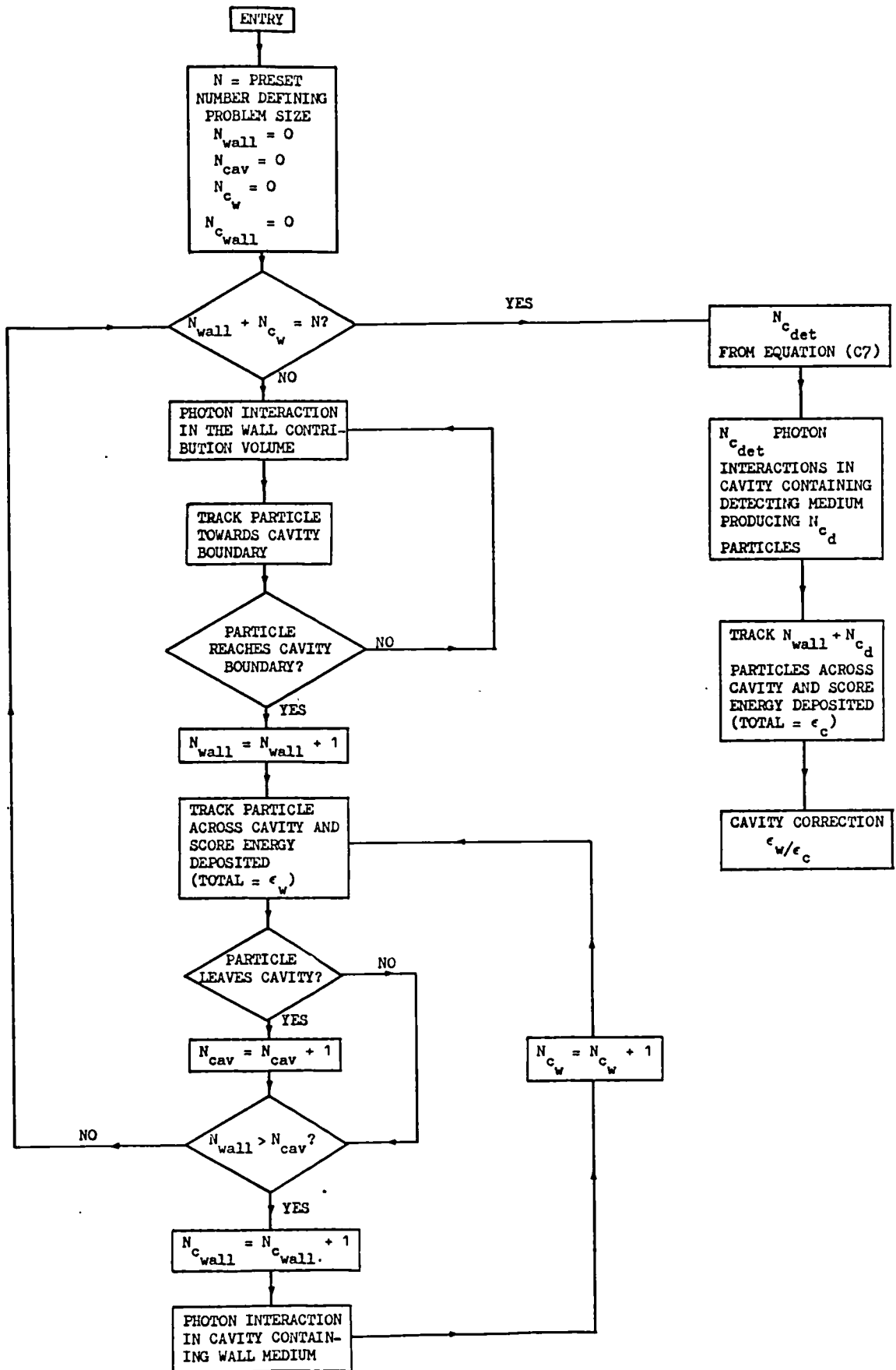
$$T_{+} = m_0 c^2 (E_{+} - 1), \quad T_{-} = m_0 c^2 (E_{-} - 1)$$

$\alpha = e^2/\hbar c$  where  $e$  is the elementary charge;

$\hbar$  is Planck's constant/ $2\pi$ ;

$c$  is the velocity of light;

$E_{\gamma m}$ ,  $E_{+}$ ,  $E_{-}$ ,  $P_{+}$ ,  $P_{-}$ , are in units of  $m_0 c^2$  and  $T_{+}$ ,  $T_{-}$  are in eV.



FLOW DIAGRAM FOR THE CALCULATION OF THE RELATIVE NUMBER  
OF PHOTON INTERACTIONS IN THE WALL AND CAVITY REGIONS

FIGURE C2

### C2.3 Particle Energy Deposition

Elastic collisions with a nucleus predominate and, as outlined previously, it was necessary to group collisions together to include this effect. The charged particle path was divided into steps of length  $\Delta s$  mm ( $\Delta s' \text{ gcm}^{-2}$ ) and at the end of each step a polar direction  $\phi$  was chosen from the multiple scattering distribution described below. The azimuthal angle  $\theta$  was sampled from an isotropic distribution. The new  $x_1, y_1, z_1$  co-ordinates for a particle having travelled a distance  $\Delta s$  from co-ordinates  $x_0, y_0, z_0$  are given by:

$$\begin{aligned} x_1 &= x_0 + \Delta s \sin\phi_1 \cos\theta_1 \\ y_1 &= y_0 + \Delta s \sin\phi_1 \sin\theta_1 \\ z_1 &= z_0 + \Delta s \cos\phi_1 \end{aligned} \quad \text{--- (C16)}$$

where the directions at the beginning of the step  $\phi_0, \theta_0$  are related to the new directions  $\phi_1, \theta_1$  by:

$$\begin{aligned} \cos\phi_1 &= \cos\phi_0 \cos\phi + \sin\phi_0 \sin\phi \cos\theta \\ \sin\phi_1 &= (1 - \cos^2\phi_1)^{\frac{1}{2}} \end{aligned} \quad \text{--- (C17)}$$

$$\begin{aligned} \sin\theta_1 &= a' \sin\theta_0 + b' \cos\theta_0 / \sin\phi_1 \\ \cos\theta_1 &= a' \cos\theta_0 - b' \sin\theta_0 / \sin\phi_1 \end{aligned} \quad \text{--- (C18)}$$

$$\begin{aligned} \text{where } a' &= \cos\phi \sin\phi_0 - \cos\phi_0 \sin\phi \cos\theta \\ b' &= \sin\phi \sin\theta \end{aligned}$$

The distance  $r_s$ , between the particle's starting position  $x, y, z$ , and its position at the end of any given step is given by:

$$r_s^2 = (x_1 - x)^2 + (y_1 - y)^2 + (z_1 - z)^2 \quad \text{--- (C19)}$$

In order that time was not wasted following particles that could not finally score in the cavity a straight line track from the random starting position to a random position on the cavity boundary was first defined. This will be called the projected particle path,  $p_s$ . A particle's history was "frozen" once the distance  $r_s$  exceeded the projected particle path. The energy loss in each step due to inelastic collisions was computed from the appropriate energy deposition data set (G2.1.3). The particle's energy was therefore known when its history was frozen, this energy being adjusted to account for the fact that  $r_s$  exceeded  $p_s$  in the final step. Obviously the final co-ordinates will not be the same as the original final position chosen on the cavity boundary but this is irrelevant since the particle had only travelled through the homogeneous wall medium. The same procedure was adopted when the particles traversed the cavity. A vast amount of computing time is saved with this approach. The shortcoming of the method is that particles may enter and leave the cavity more than once during a "true" history. However, in the majority of problems this approach is valid since the errors due to the assumption tend to cancel when large numbers of particles are considered.

It has been shown [ 7 ] that if a logarithmic step is chosen the average angular multiple scattering deflection per step remains approximately constant. A formula derived by Blanchard and Fano is given in the above reference which approximates the mean value of the cosine of the deflection angles as a function of electron energy and atomic number:

$$\langle \cos\phi \rangle_{av} = \left[ \frac{a(T_m + 2)}{aT_m + 2} \right]^{0.3Z} \quad - - - \quad (G20)$$

where  $a$  is the factor by which the energy is reduced.

The resultant angular multiple scattering deflection from a large number of collisions in distance  $\Delta s$  tends to a Gaussian distribution provided the individual deflections are small and energy losses can be ignored. Rossi [68] gives the following probability distribution in the Gaussian approximation:

$$P(\phi)d\phi = \frac{(2\pi X)^{-\frac{1}{2}}}{\phi_s} e^{-\frac{\phi^2}{2\phi_s^2 X}} \quad \text{--- (C21)}$$

where  $X$  is the step size in radiation lengths ( $\Delta s'/X_0$ )

$$\frac{1}{X_0} = 4\alpha \frac{N_A}{A} Z^2 r_o^2 \ln(183 Z^{-\frac{1}{2}}) \quad \text{--- (C22)}$$

$\phi$  is measured in a plane normal to the incident direction.  $\phi_s$  is calculated from an appropriate single-scattering cross-section. Rossi used the Rutherford scattering formula and obtained two results depending on the scattering angle limits used in the evaluation, the formula giving the smaller value being used in equation (C21):

$$\phi_s^2 = 16\pi N_A \frac{Z^2}{A} r_o^2 \left( \frac{m_o c}{\beta p_o} \right)^2 \ln \left[ 196 Z^{-\frac{1}{2}} \left( \frac{Z}{A} \right)^{1/6} \right] \quad \text{--- (C23)}$$

$$\phi_s^2 = 16\pi N_A \frac{Z^2}{A} r_o^2 \left( \frac{m_o c}{\beta p_o} \right)^2 \ln \left[ \frac{137 p_o}{Z^{\frac{1}{2}} m_o c} \right]^{\frac{1}{2}} \quad \text{--- (C24)}$$

where  $p_o$  is the particle momentum

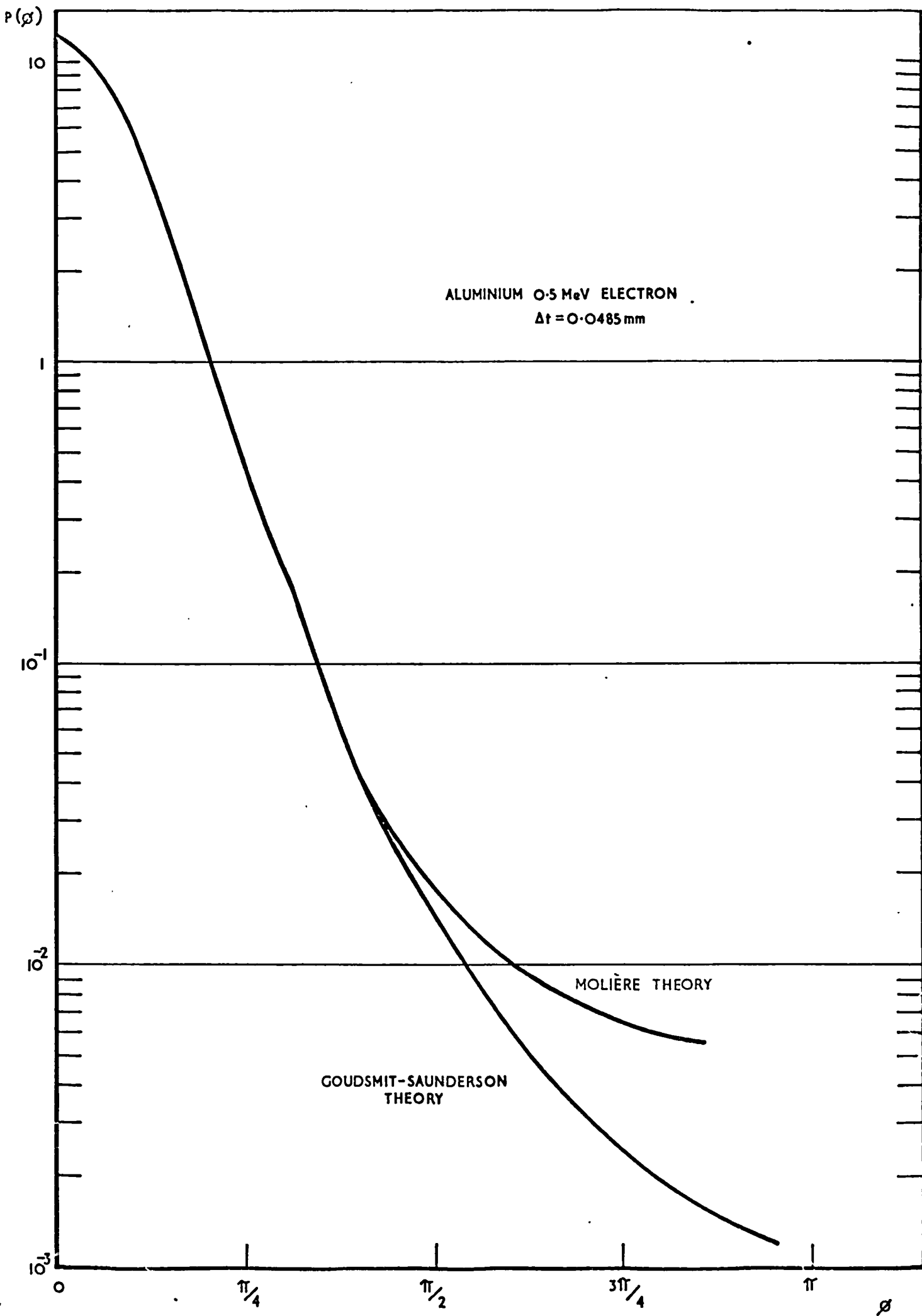
$$= (T_m^2 + 2T_m)^{\frac{1}{2}} m_o c \text{ g cm sec}^{-1}$$

The above method was initially used in PROCEED but because the expressions cannot be correct for all angles, results were not

satisfactory. As Rossi pointed out, it is possible for the Gaussian distribution to give a probability of deflection smaller than the probability for the same deflection to occur in a single scattering process.

The exact determination of the distribution function has been carried out in the small-angle approximation by Snyder and Scott, and Molière. Multiple-scattering theory is very complicated and the evaluation difficult. The data and method used in PROCEED were obtained from a review article on small-angle scattering by Scott [69] and a paper by Bethe [70] on Molière's theory. The latter paper discusses the relationship with an exact theory by Goudsmit and Saunderson which is valid for any angle by means of an expansion in Legendre polynomials. PROCEED uses the Molière theory to compute the total scattering angle distribution and extends the theory to include large angles by multiplying the distribution by a factor  $(\phi/\sin\phi)^{\frac{1}{2}}$  as suggested by Bethe. Figure C3 compares the angular distribution of multiply scattered electrons in aluminium calculated using the Molière theory and the general Goudsmit-Saunderson theory. The following description details the steps involved in calculating the scattering distribution; the derivation is best described in the above references.

Molière assumed that all scattering angles are small so that  $\sin\phi$  may be replaced by  $\phi$  and that the distribution can be considered independent of the azimuthal angle. The Molière distribution is given by equation (C25) where the parameters  $\chi_c$  and B are evaluated on the basis of a single scattering theory which is reasonably exact but does not distinguish between



ANGULAR DISTRIBUTION OF MULTIPLY SCATTERED ELECTRONS IN ALUMINIUM  
 FIGURE C3



electrons and positrons.

$$p(\phi)d\phi = \nu d\nu \left[ f^{(0)}(\nu) + B^{-1}f^{(1)} + B^{-2}f^{(2)}(\nu) + \dots \right] \quad (C25)$$

where  $f^{(n)}$  are purely numerical functions;

$$\text{and } \nu = \phi/(\chi_c B^{\frac{1}{2}}) - \text{the "reduced scattering angle"} \quad (C26)$$

The angular distribution depends only on the ratio  $\chi_c/\chi'_\alpha$ .

The probability of a single scatter in the step size (foil thickness)  $\Delta s'$  through an angle greater than  $\chi_c$  is unity.

The "unit probability angle" describes the foil thickness and is given by:

$$\chi_c^2 = \frac{4\pi N_A \Delta s' e^4 Z^2}{A(p_o^v)^2} \quad (C27)$$

$$p_o^v = \frac{(T_m^2 + 2T_m)m_o c^2}{T_m + 1} \quad \text{g cm}^2 \text{sec}^{-2} \quad (C28)$$

The "screening angle"  $\chi'_\alpha$  is given by:

$$\chi'_\alpha{}^2 = 1.167 \chi_\alpha^2 \quad (C29)$$

$$\text{where } \chi_\alpha^2 = \chi_o^2 (1.13 + 3.76 Z^2 \alpha^2) \quad (C30)$$

$$\text{and } \chi_o = \frac{\hbar}{0.885 p_o a_o Z^{-\frac{1}{2}}} \quad (C31)$$

where  $a_o$  is the Bohr radius.

Nigam et al [71] have shown these expressions for the screening angle to be incorrect and have refined the theory which also enables differences between electrons and positrons to be taken into account.

The mean number of scatterings in  $\Delta s$  is given approximately by

$(X_c/X_\alpha)^2$  and for the Molière theory this should be in the range 20 and  $10^5$  (although the lower limit has been decreased to a certain extent by the work of Zeil et al as described in Reference [69]). When there are less than 20 collisions in a distance  $\Delta s$  PROCEED increases the step size so that the Molière conditions apply. There is, however, a limit when multiple scattering becomes a random walk. For the reasons described earlier the program uses a logarithmic step size. In order to compute this it is necessary to input a "multiple scattering step parameter" (n). The quantity  $nZ^{1/2}$  represents the number of steps required to reduce a particle of energy  $T_m$  to an energy  $T_m/2$ :

$$a = 2^{-1/nZ^{1/2}} \quad \text{--- (C32)}$$

PROCEED can also automatically select a value for n that has proved suitable for most situations:

$$n = \frac{Sp}{T_m} + 3 \quad \text{--- (C33)}$$

The parameter B is obtained from the transcendental equation

$$b = B - \ln B \quad \text{--- (C34)}$$

$$\text{where } b = \ln \left( \frac{X_c}{X_\alpha} \right)^2 \quad \text{--- (C35)}$$

The first function  $f^{(0)}$  is given by:

$$f^{(0)} = 2e^{-v^2} \quad \text{--- (C36)}$$

The functions  $f^{(1)}$  and  $f^{(2)}$  were obtained from the calculations in the Scott paper and are given in Table C1. PROCEED interpolates from this data.

In order to include inelastic collisions  $Z(Z+1)$  replaced the  $Z^2$  in

Table C1

The Functions  $f^{(n)}$  Used in Molière's Theory of Multiple Scattering

$\nu$	$f^{(0)}$	$f^{(1)}$	$f^{(2)}$
0.0	2.00000E+00	8.45600E-01	2.49290E+00
0.10	1.98010E+00	8.09000E-01	2.38270E+00
0.20	1.92160E+00	7.03800E-01	2.06940E+00
0.30	1.82790E+00	5.42400E-01	1.60140E+00
0.40	1.70430E+00	3.43600E-01	1.04880E+00
0.50	1.55760E+00	1.29600E-01	4.89600E-01
0.60	1.39540E+00	-7.75999E-02	-4.40000E-03
0.70	1.22530E+00	-2.58400E-01	-3.79400E-01
0.80	1.05460E+00	-3.98000E-01	-6.06800E-01
0.90	8.89720E-01	-4.88600E-01	-6.85200E-01
1.00	7.35760E-01	-5.28400E-01	-6.35900E-01
1.10	5.96390E-01	-5.21800E-01	-4.95900E-01
1.20	4.73860E-01	-4.77000E-01	-3.08600E-01
1.30	3.69040E-01	-4.05200E-01	-1.15100E-01
1.40	2.81720E-01	-3.18200E-01	5.25000E-02
1.50	2.10800E-01	-2.26600E-01	1.74000E-01
1.60	1.54610E-01	-1.39560E-01	2.42200E-01
1.70	1.11150E-01	-6.29600E-02	2.60300E-01
1.80	7.83280E-02	-6.10000E-04	2.38700E-01
1.90	5.41040E-02	4.62600E-02	1.91100E-01
2.00	3.66310E-02	7.82200E-02	1.31600E-01
2.20	1.58140E-02	1.05420E-01	1.96400E-02
2.40	6.30220E-03	1.00780E-01	-4.67200E-02
2.60	2.31850E-03	8.26200E-02	-6.48900E-02
2.80	7.87340E-04	6.24800E-02	-5.46000E-02
3.00	2.46820E-04	4.55000E-02	-3.56900E-02
3.20	7.14260E-05	3.28800E-02	-1.92300E-02
3.40	1.90800E-05	2.40200E-02	-8.47000E-03
3.60	4.70510E-06	1.79060E-02	-2.64300E-03
3.80	1.07110E-06	1.36560E-02	4.57200E-05
4.00	2.25070E-07	1.06380E-02	1.07400E-03
5.00	2.77760E-11	3.83000E-03	8.32600E-04
6.00	4.63900E-16	1.74000E-03	3.49500E-04
7.00	1.04860E-21	9.08000E-04	1.58300E-04
8.00	3.20760E-28	5.21200E-04	7.83300E-05
9.00	1.32790E-35	3.20800E-04	4.17600E-05
10.00	7.44020E-44	2.08400E-04	2.36800E-05

equation (C27) and similarly in equation (C22), although Fano [72] suggested an extra term to increase b in equation (C35).

Bethe suggested that Molière's theory could be made exact and relativistic by multiplying by the ratio of the exact single-scattering cross-section to the Molière non-relativistic cross-section and this has been carried out by Spencer and Blanchard [73]. It was, however, found that the inclusion of this correction and that of Nigam et al made negligible difference to the cavity correction results and was therefore not worth the extra computing effort.

#### C2.4 Particle Equilibrium

Figure C2, page 122, shows in the form of a flow diagram how the relative number of interactions in the wall contribution volume, cavity containing the wall medium, and cavity containing the detecting medium, are computed. Equilibrium must be maintained between particles entering and leaving the cavity whilst containing the wall medium:

$$N_{\text{wall}} = N_{\text{cav}} \quad - - - \quad (C37)$$

where  $N_{\text{wall}}$  is the number of particles entering the cavity;

$N_{\text{cav}}$  is the number of particles leaving the cavity.

Due to the existence of charged particle equilibrium the same amount of energy therefore enters and leaves the cavity while containing the wall medium.

PROCEED generates and tracks particles until:

$$N = N_{\text{wall}} + N_{\text{c}_w} \quad - - - \quad (C38)$$

where N is a preset number defining array space and  $N_{\text{c}_w}$  is the

number of particles generated in the cavity containing the wall medium from  $N_{c_{wall}}$  interactions. Once  $N$  has been reached  $N_{c_d}$  particles are generated in the cavity containing the detecting medium where  $N_{c_{det}}$  (the number of photon interactions in the cavity detecting medium) is first obtained from equation (C7).

### C3 Monoenergetic Photon Sources

Assuming uniformly distributed monoenergetic photon sources PROCEED has been used to calculate  $\epsilon_w/\epsilon_c$  and its components for various wall materials surrounding a 1 mm x 1 mm x 6 mm lithium fluoride cavity. The results are given in Figures C4-C6. These calculations do not include in the input spectrum the Compton scattered photons and pair-production photons, but only the monoenergetic source. To obtain a value  $\epsilon_w/\epsilon_c$  for the true energy photon spectrum, or any other given spectrum, from these curves it is necessary to perform the following operation:

$$\frac{\bar{\epsilon}_w}{\epsilon_c} = \frac{\int \Phi(E_\gamma) \mu_{wall}(E_\gamma) E_\gamma dE_\gamma}{\int \Phi(E_\gamma) \mu_{wall}(E_\gamma) E_\gamma / \frac{\epsilon_w}{\epsilon_c} dE_\gamma} \quad \text{--- (C39)}$$

Table C2 gives the mass energy absorption coefficients for  $Li^7F$  used in this work. These were obtained from page 625 of Reference [2] and to account for the isotopic effect in  $Li^7F$  the values have been corrected as suggested by Attix [74]. The mass energy absorption coefficients for  $Cs^{137}$  and  $Co^{60}$  photons are  $0.02713 \text{ cm}^2 \text{ g}^{-1}$  and  $0.02458 \text{ cm}^2 \text{ g}^{-1}$  respectively. However, it should be noted that to be consistent with PROCEED the escape of fluorescence radiation and bremsstrahlung should not be included in the coefficients.

Table C2

Li<sup>7</sup>F Mass Energy Absorption Coefficients

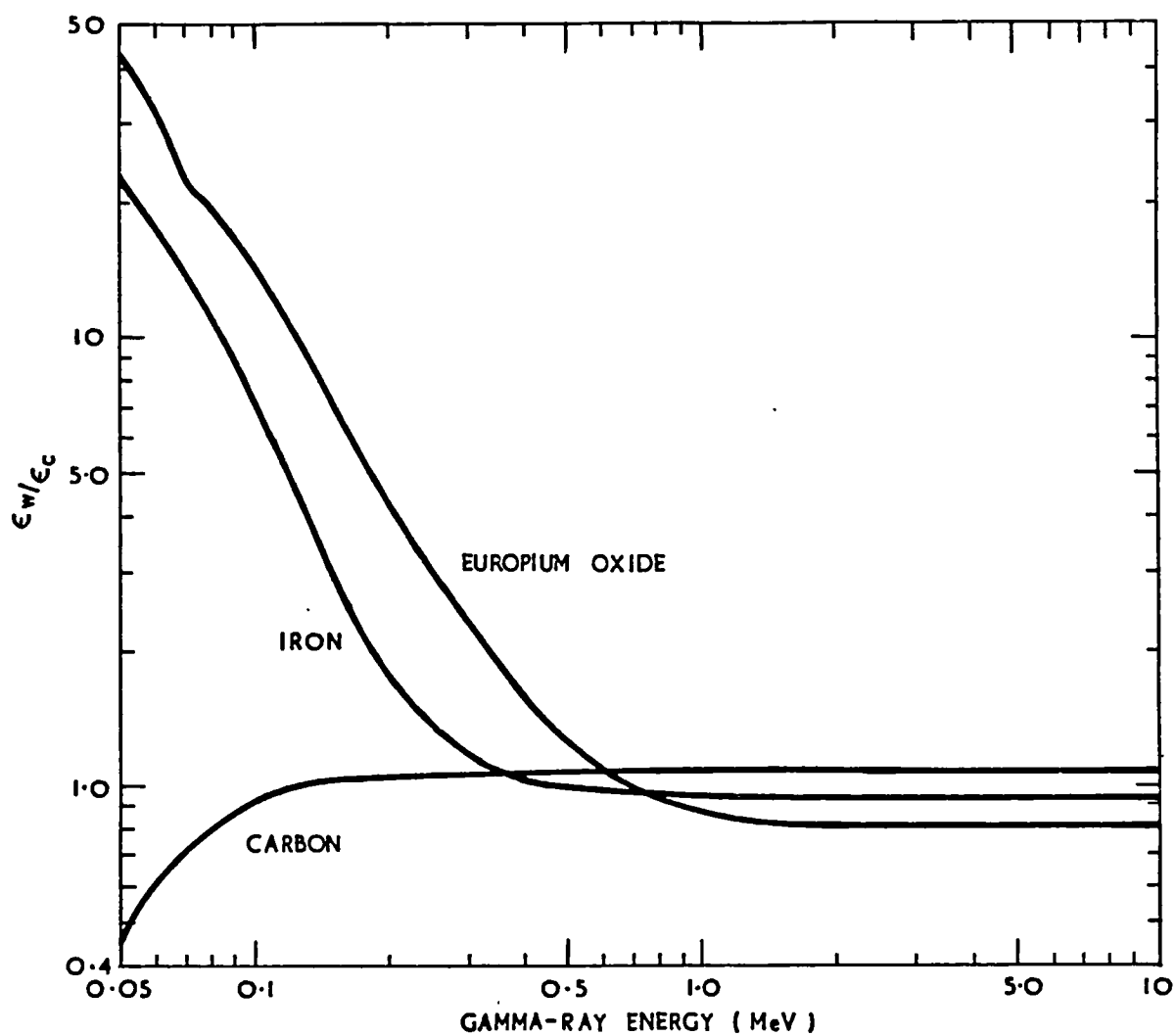
Energy (MeV)	$\frac{\mu_{en}}{\rho}$ (cm <sup>2</sup> g <sup>-1</sup> )
0.010	5.5932
0.015	1.5055
0.020	0.6052
0.030	0.1735
0.040	0.0761
0.050	0.0447
0.060	0.0322
0.080	0.0239
0.100	0.0223
0.150	0.0233
0.200	0.0248
0.300	0.0265
0.400	0.0273
0.500	0.0275
0.600	0.0273
0.800	0.0266
1.000	0.0257
1.500	0.0235
2.000	0.0216
3.000	0.0189
4.000	0.0173
5.000	0.0161
6.000	0.0152
8.000	0.0141
10.000	0.0134

Table C3 demonstrates the effect of the change of cavity size for a fixed photon energy (0.66 MeV) for a lead wall and carbon cavity.  $\epsilon_w/\epsilon_c$  tends towards the mass stopping power ratio for the small cavity and the mass absorption coefficient for the large cavity.

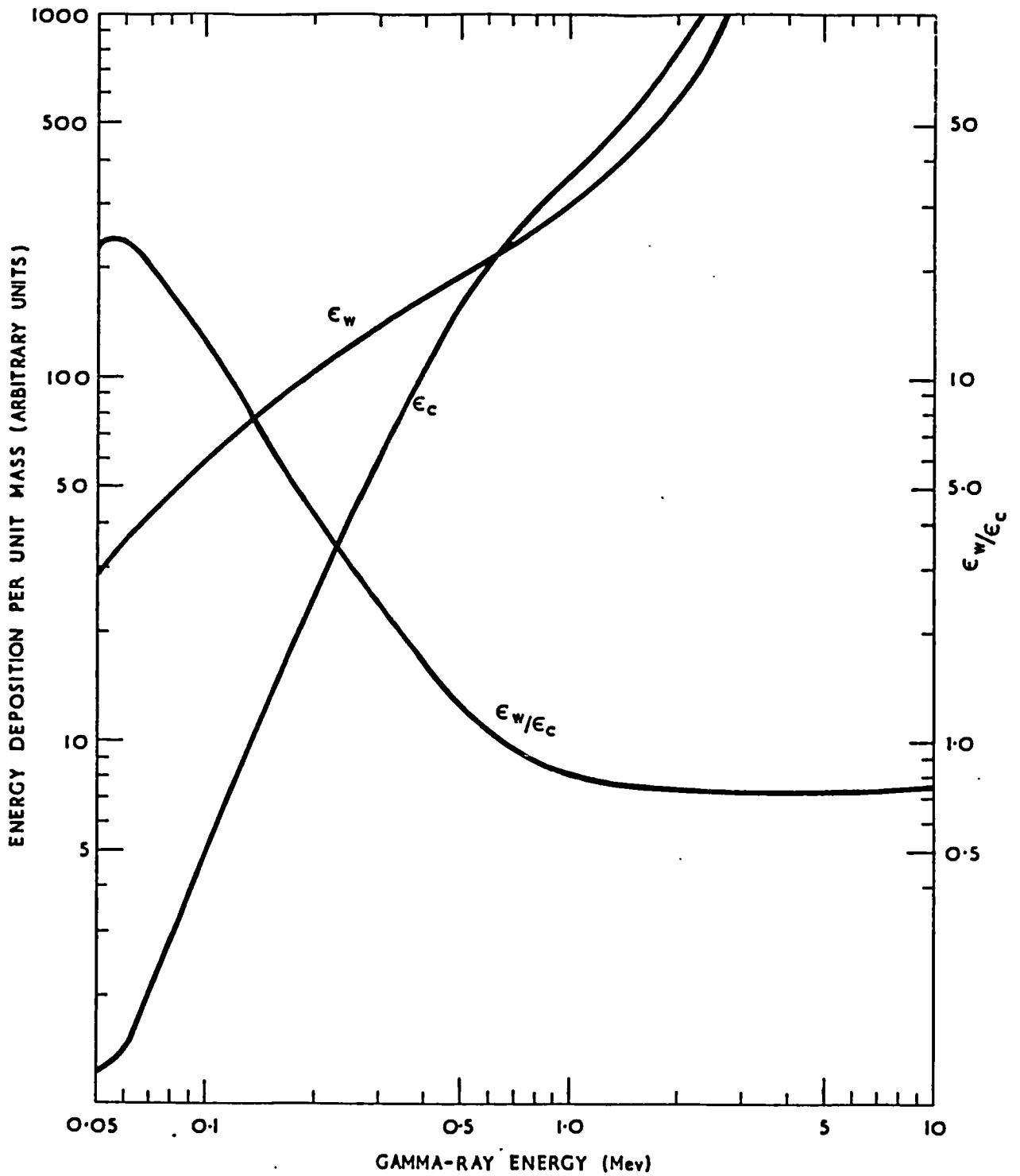
Table C3

$\epsilon_w/\epsilon_c$  as a Function of Cavity Size for Lead Wall and Carbon Cavity at 0.66 MeV

Dimension (mm) of cavity side (x=y=z)	$\epsilon_w/\epsilon_c$
0.001	0.60
0.01	0.65
0.1	1.12
1.0	1.27
10.0	1.94
1000.0	2.25



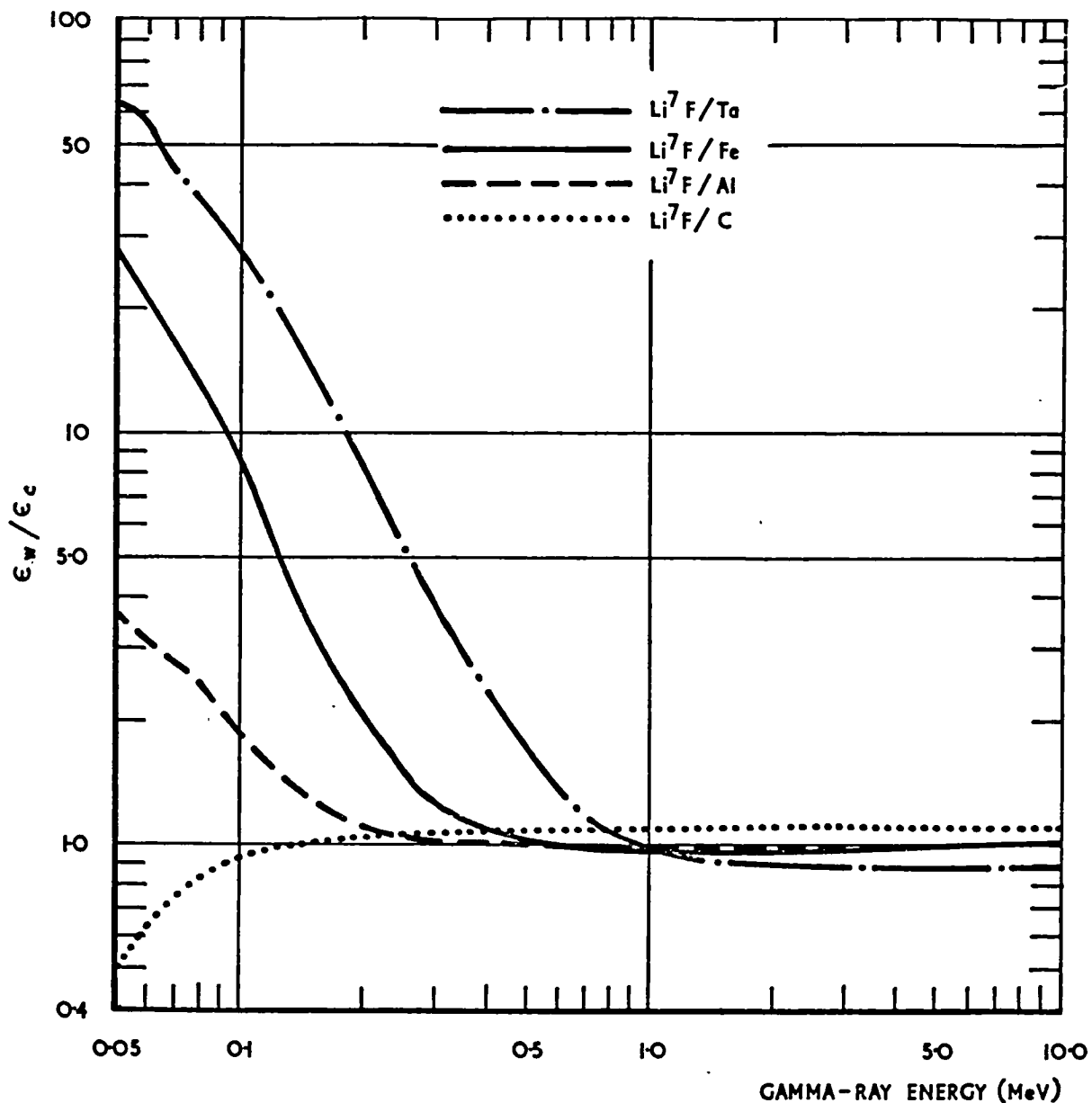
THE CAVITY CORRECTION RATIO  $\epsilon_w/\epsilon_c$  AS A FUNCTION OF ENERGY FOR A 1mm X 1mm X 6mm  $\text{Li}^{7}\text{F}$  CAVITY SURROUNDED BY VARIOUS MATERIALS WITHOUT MULTIPLE SCATTERING  
 FIGURE C4



THE CALCULATED ENERGY DEPOSITION, AS A FUNCTION OF ENERGY, IN A 1mm X 1mm X 6mm CAVITY CONTAINING  $Ta(\epsilon_w)$  AND  $Li^7F(\epsilon_c)$  WHILE SURROUNDED BY TANTALUM WITHOUT MULTIPLE SCATTERING

FIGURE C5





THE CAVITY CORRECTION RATIO  $\frac{\epsilon_w}{\epsilon_c}$  AS A FUNCTION OF ENERGY FOR A  
 1mm X 1mm X 6mm Li<sup>7</sup>F CAVITY SURROUNDED BY VARIOUS MATERIALS  
 WITH MULTIPLE SCATTERING

FIGURE C6

The input data for the calculations is given below in Table C4.

Table C4

Data for the PROCEED Calculations

Material	Density (g cm <sup>-3</sup> )	Elements	Z	Atomic Weight*	Mean Excitation Potential (eV)
Li <sup>7</sup> F	2.62	Li <sup>7</sup>	3	7.016	42.0
		F	9	18.998	110.3
C	1.77	C	6	12.011	78.0
B <sub>1</sub> C(nat)	2.388	B(nat)	5	10.811	66.5
B <sub>4</sub> C(enr)	2.282	B(enr)	5	10.213	66.5
Al	2.70	Al	13	26.9815	164.0
Eu <sub>2</sub> O <sub>3</sub>	7.68	Eu	63	151.960	607.0
		O	8	15.999	98.0
Fe	7.86	Fe	26	55.847	279.0
Ta	16.57	Ta	73	180.948	700.8

\*Based on C<sup>12</sup> scale [11]

#### C4 Program Users Guide

##### C4.1 Machine Requirements

The program is stored as a disc load module under the data set name ZXKPRCD for the Harwell IBM 370. It is stored without the system library routines and the free format routine (ZXAREAD3). Photon cross-section data for the program are stored on disc under the data set name ZXKHYTR.

PROCEED interrogates the JCL at run time, enabling the program to access the whole available fast core partition. Problems of widely differing size can therefore be run efficiently without the need for recompilation. Should insufficient core have been allocated in the G.REGION the job will stop, printing details of the extra space required.

The problem size is controlled by the first number in the input data (NOHIST). The size of the G.REGION in kilobytes is approximately given by  $(0.023 \times \text{NOHIST}) + 180$ . NOHIST can be interpreted in most cases as the number of charged particles scoring in the cavity whilst it contains the wall medium. The CPU time for a particular job is very much problem dependent.

#### C4.2 Input Data

Apart from the title, which must occupy a single card image, all input is free format, although type (real/integer) must be adhered to. The input data is given in Table C5. To ensure that enough working space is allowed it is recommended that NOHIST is set to at least 1000. The initial random number can be any integer between 1 and  $10^6$ . Table C5 reference numbers 5 to 8 are repeated for each element in the wall medium and similarly with numbers 10 to 13 for the detecting medium. The choice of a suitable multiple scattering step parameter (MSTEP) is problem dependent (see C2.3 where n is the step parameter). For trial runs, and cases where multiple scattering is unimportant, MSTEP can be set to zero and PROCEED will assume straight line paths for the particles. A negative value of this parameter gives the program control to automatically select the value of MSTEP and this facility should prove suitable for most problems. All energies in the input data must be given in electron-volts. The photon spectrum can only be entered in histogram form and should be in the energy range 15 KeV to 15 MeV.

#### C4.3 Output from Calculation

The output from the program consists of the relative contribution

Table C5

## PROCEED Input Data

Reference Number	Variable	Format	Description
1	NOHIST	Integer	Number of histories. Defines problem size and sets array dimensions (>1000)
2	NRAND	Integer	Initial random number between 1 and $10^6$
3	TITLE	Alpha-numeric	Case title (single card image)
4	NELEMW	Integer	Number of elements in wall For each element numbers 5 to 8 repeated:
5	NZW	Integer	Atomic number
6	AW	Real	Atomic weight
7	CIW	Real	Mean excitation potential (eV)
8	WIFRW	Real	Fraction by weight
9	NELEMC	Integer	Number of elements in detecting medium For each element numbers 10 to 13 repeated:
10	NZC	Integer	Atomic number
11	AC	Real	Atomic weight
12	CIC	Real	Mean excitation potential (eV)
13	WIFRC	Real	Fraction by weight
14	ROW	Real	Density of wall medium ( $\text{g cm}^{-3}$ )
15	ROC	Real	Density of detecting medium ( $\text{g cm}^{-3}$ )
16	XC	Real	Cavity dimension in x-direction (mm)
17	YC	Real	Cavity dimension in y-direction (mm)
18	ZC	Real	Cavity dimension in z-direction (mm)
19	MSTEP	Integer	Multiple scattering step parameter (0 for no multiple scattering, -ve for program selected value)
20	NGAM	Integer	Number of energy groups in photon spectrum
21	EGAM	Real array	Energy group boundaries, NGAM+1 values (eV)
22	PGAM	Real array	Relative group flux, NGAM values

to the cavity correction along with the final ratio and associated standard deviation. In addition, the computed path lengths in the two media for the maximum source energy electron and a breakdown of the number of photon interactions and particles involved, are also output. A test case output is included at the end of this appendix (pages 141-145).

#### C4.4 Error Messages

Should a job fail during the input stage the data being queried is flagged. A flag on the last entry usually indicates that the program expects further data. Apart from the details of extra core requirements discussed in C4.1, there are no other error messages.

One of the system subroutines called by PROCEED produces an underflow which does not affect the calculation. Therefore the program interrupts have simply been suppressed using the ERRSET subprogram (although the error number 208 is still printed at the end of the job). However, program interrupts due to underflow and other errors occurring elsewhere during the execution are not suppressed and must always be investigated. This type of error should only occur with unreasonable input data or where insufficient histories have been considered.

\*\*\*\*\*  
\* \* \* \* \*  
\* PROCEED \*  
\* \* \* \* \*  
\*\*\*\*\*

LIF CAVITY (1\*1\*6) WITH FE WALL (EXAMPLE RUN)

INPUT DATA:

ELEMENTS IN THE WALL MEDIUM

ATOMIC NUMBER= 26  
ATOMIC WEIGHT= 55.847  
MEAN EXCITATION ENERGY=279.000  
FRACTION BY WEIGHT= 1.00000

ELEMENTS IN DETECTING MEDIUM

ATOMIC NUMBER= 3  
ATOMIC WEIGHT= 7.016  
MEAN EXCITATION ENERGY= 42.000  
FRACTION BY WEIGHT= 0.26970

<sup>241</sup>  
ATOMIC NUMBER= 9  
ATOMIC WEIGHT= 18.998  
MEAN EXCITATION ENERGY=110.250  
FRACTION BY WEIGHT= 0.73030

DENSITY OF WALL MEDIUM= 7.860 GM/CM3

DENSITY OF DETECTING MEDIUM= 2.620 GM/CM3

CAVITY DIMENSIONS(MM)= 1.00000\* 1.00000\* 6.00000

MULTIPLE SCATTERING STEP PARAMETER= -1

NUMBER OF HISTORIES= 1000

INITIAL RANDOM NUMBER= 3459

PHOTON SPECTRUM

ENERGY BOUNDARIES (EV)

0.50000E+05	0.10000E+06	0.15000E+06	0.20000E+06	0.25000E+06	0.30000E+06	0.35000E+06	0.40000E+06
0.45000E+06	0.50000E+06	0.55000E+06	0.60000E+06	0.65000E+06	0.70000E+06	0.75000E+06	0.80000E+06
0.85000E+06	0.90000E+06	0.95000E+06	0.10000E+07	0.10500E+07	0.11000E+07	0.11500E+07	0.12000E+07
0.12500E+07	0.13000E+07	0.13500E+07					

NUMBER

0.60230E+02	0.46815E+03	0.53023E+03	0.51148E+03	0.42216E+03	0.26754E+03	0.27590E+03	0.28662E+03
0.19506E+03	0.16745E+03	0.14029E+03	0.10746E+03	0.10044E+03	0.12957E+03	0.10569E+03	0.10529E+03
0.11103E+03	0.82951E+02	0.12135E+03	0.77453E+02	0.65034E+02	0.64896E+02	0.22824E+03	0.30213E+02
0.39223E+02	0.23887E+03						



COMPUTED DATA:

PATHLENGTH OF MAXIMUM ENERGY SOURCE ELECTRON( 1.35MEV) IN WALL MEDIUM = 1.106 MM

PATHLENGTH OF MAXIMUM ENERGY SOURCE ELECTRON( 1.35MEV) IN DETECTING MEDIUM = 2.913 MM

NUMBER OF INTERACTIONS GENERATING PARTICLES WHICH TRACK TOWARDS CAVITY= 1218

NUMBER OF ELECTRONS/POSITRONS THAT REACH CAVITY BOUNDARY WITH ENERGY GREATER THAN 10KEV= 43

NUMBER OF INTERACTIONS GENERATING PARTICLES IN CAVITY(WALL MEDIUM)= 957

NUMBER OF ELECTRONS/POSITRONS LEAVING THE CAVITY(WALL MEDIUM)= 43

NUMBER OF INTERACTIONS GENERATING PARTICLES IN CAVITY(DETECTING MEDIUM)= 251

SCORED ENERGY(WALL MEDIUM IN CAVITY):

CONTRIBUTION FROM WALL= 9.8929 MEV/CM3  
= 1.2586 MEV/G

CONTRIBUTION FROM CAVITY= 120.9015 MEV/CM3  
= 15.3819 MEV/G

SCORED ENERGY(DETECTING MEDIUM IN CAVITY):

CONTRIBUTION FROM WALL= 7.8300 MEV/CM3  
= 2.9886 MEV/G

CONTRIBUTION FROM CAVITY= 26.6923 MEV/CM3  
= 10.1879 MEV/G

ENERGY DEPOSITION /UNIT MASS(WALL)= 1.2629 \* ENERGY DEPOSITION/UNIT MASS(CAVITY)

STANDARD DEVIATION= 7.44%

## APPENDIX D

### LIST OF SYMBOLS

The majority of symbols, constants and basic relationships used throughout the thesis are listed in this appendix.

A	Atomic weight
B	Molière distribution parameter (equation C34)
$C_n$	Contribution to detector signal from neutrons
$C_\gamma$	Contribution to detector signal from photons
D	Absorbed dose-rate ( $\text{rad hr}^{-1}$ )
E	Neutron energy (MeV)
$E_c$	Energy deposited per unit mass in the cavity detecting medium ( $\text{MeV g}^{-1}$ )
$E_n$	Energy lost by neutron in elastic scattering ( $\text{MeV cm}^{-3} \text{sec}^{-1}$ )
$E_r$	Energy of a recoil nucleus (MeV)
$E_w$	Energy deposited per unit mass in the wall medium ( $\text{MeV g}^{-1}$ )
$E_\gamma$	Photon energy (eV)
$E_{\gamma'}$	Compton scattered photon energy (eV)
$E_{\gamma_m}$	Photon energy ( $m_0 c^2$ units)
$E_+$	Energy of positron produced in pair production ( $m_0 c^2$ units)
$E_-$	Energy of electron produced in pair production ( $m_0 c^2$ units)
F	Sub-section C2.1.3
I	Mean excitation potential of atom (eV)
J	Number of ion pairs per unit mass of gas
K	Kerma (rad)
$K_+$ , $K_-$ , L	Equation C15
LET	Linear energy transfer ( $\text{erg cm}^{-1}$ )

$M$	Number of Legendre coefficients
$N$	Total number of particles entering cavity, and generated in cavity, whilst containing the wall medium
$N_A$	Avagadro constant = $6.02252 \times 10^{23}$ atoms/mole
$N_c$	Neutron recoil dose-rate in ionisation chamber gas ( $\text{rad hr}^{-1}$ )
$N_{\text{cav}}$	Number of particles leaving the cavity whilst containing wall medium
$N_{c_d}$	Number of particles produced from $N_{c_{\text{det}}}$ interactions
$N_{c_{\text{det}}}$	Number of photon interactions in cavity whilst containing detecting medium
$N_{c_w}$	Number of particles produced from $N_{c_{\text{wall}}}$ interactions
$N_{c_{\text{wall}}}$	Number of photon interactions in cavity whilst containing wall medium
$N_{\text{com}}(T_-)$	Compton distribution
$N_{\text{cr}}$	Number of ion pairs produced by a gas recoil nucleus
$N_e$	Number of ion pairs produced by a secondary electron induced by a photon
$N_{\text{pp}}(E_+)$	Bethe-Heitler pair-production distribution
$N_w$	Neutron recoil dose-rate in ionisation chamber wall ( $\text{rad hr}^{-1}$ )
$N_{\text{wall}}$	Number of particles entering the cavity from wall contribution volume
$P(\phi)$	Multiple scattering distribution (Appendix C)
$P(\theta, E_\gamma)$	Probability that photon of energy $E_\gamma$ is scattered through an angle between $\theta$ and $\theta+d\theta$
$P^{i-j}(u)$	Probability per steradian of scattering from group $i$ to $j$ through angle whose cosine is $u$
$P_l(u)$	Value of the $l$ th Legendre polynomial for angle whose cosine is $u$
$P_s^{i-j}$	Probability of scattering from group $i$ to $j$

Q	Li <sup>7</sup> F recoil response relative to Co <sup>60</sup> energies
R	Exposure rate (Roentgen hr <sup>-1</sup> )
R <sub>e</sub>	Electron range (g cm <sup>-2</sup> )
S <sub>c</sub>	Relative sensitivity to ionisation chamber gas recoils
S <sub>cr</sub>	Ionisation chamber's sensitivity to gas cavity recoils
S <sub>w</sub>	Relative sensitivity to ionisation chamber wall recoils
S <sub>wr</sub>	Ionisation chamber's sensitivity to wall recoils
S <sub>γ</sub>	Detector sensitivity to photons
S <sub>γ</sub> '	Pressure independent detector sensitivity to photons
S/ρ	Mass stopping power (MeV cm <sup>2</sup> g <sup>-1</sup> )
T <sub>i</sub>	Initial electron energy (eV)
T <sub>f</sub>	Final electron energy after travelling distance s (eV)
T <sub>m</sub>	Electron energy (m <sub>0</sub> c <sup>2</sup> units)
T <sub>max</sub>	Maximum electron energy produced during photon interactions (eV)
T <sub>+</sub>	Positron energy (eV)
T <sub>-</sub>	Electron energy (eV)
T <sub>-</sub> (max)	Maximum recoil electron energy from Compton interaction (eV)
W <sub>cr</sub>	Average energy required by a cavity recoil nucleus to produce one ion pair (eV/ip)
W <sub>e</sub>	Average energy required by an electron to produce one ion pair (eV/ip)
X	Multiple scattering step size in radiation lengths (= Δs'/X <sub>0</sub> )
X <sub>0</sub>	Radiation length (equation C22 g cm <sup>-2</sup> )
Z	Atomic number

a	Multiple scattering energy reduction factor (equation C32)
$a_0$	Bohr radius = $5.29167 \times 10^{-9}$ cm
b	Equation C35
c	Velocity of light = $2.997925 \times 10^{10}$ cm sec <sup>-1</sup>
d	Burlin theory weighting factor (equation 13)
$d_f$	Dose-rate due to fission product decay (rad hr <sup>-1</sup> )
$d_{fc}$	Calculated dose-rate due to fission product decay (rad hr <sup>-1</sup> )
$d_m$	Measured gamma-ray dose-rate (rad hr <sup>-1</sup> )
$d_n$	Neutron corrected gamma-ray dose-rate (rad hr <sup>-1</sup> )
e	Elementary charge = $4.80298 \times 10^{-10}$ erg <sup>1/2</sup> cm <sup>1/2</sup>
$f_l^{i-j}$	The lth Legendre coefficient for scattering from group i to group j
$f_j$	Fission product photon source at saturation
$f_t$	Fission product photon source at time of measurement
$f^{(n)}$	Molière distribution numerical functions (equation C25)
g	Fraction of secondary electron energy lost to bremsstrahlung
$\hbar$	Planck's constant/ $2\pi$ = $1.05450 \times 10^{-27}$ erg sec
i, j	Energy group numbers and material numbers
k	Unit conversion constant $1 \text{ MeV g}^{-1} \text{ sec}^{-1} = 5.76788 \times 10^{-5} \text{ rad hr}^{-1}$
l	Equations 15 and 16
$m_0$	Electron rest mass = $9.1091 \times 10^{-28}$ g
$m_0 c^2$	Energy equivalent of electron rest mass = 511006 eV
n	Multiple scattering step parameter
p	Ionisation chamber gas pressure (mm Hg)
$p_0$	Particle momentum = $(T_m^2 + 2T_m)^{1/2} m_0 c$ g cm sec <sup>-1</sup>

$p_o v$	$(T_m^2 + 2T_m)m_o c^2 / T_m + 1 \text{ g cm}^2 \text{ sec}^{-2}$
$p_s$	Projected particle path (mm)
$p+$	Momentum of positron produced in pair production ( $m_o c$ units)
$p-$	Momentum of electron produced in pair production ( $m_o c$ units)
$q$	Cavity mean chord length ( $\text{g cm}^{-2}$ )
$r$	Distance travelled by photon before collision (cm)
$r_o$	Classical electron radius = $e^2/m_o c^2 = 2.81777 \times 10^{-13} \text{ cm}$
$r_s$	Distance between particles initial and final positions (mm)
$s$	Electron path length (mm)
$t$	Time (secs)
$u$	Cosine $\theta$
$\bar{u}$	Average cosine of the scattering angle in the centre-of-mass system
$v$	Particle velocity ( $\text{cm sec}^{-1}$ )
$w$	Source particle weight.
$w_j$	Fraction by weight of the jth element in medium
$x, y, z$	Cartesian co-ordinates defining particle position
$\alpha$	$= e^2/\hbar c = 1/137.04$
$\beta$	$= v/c = (T_m^2 + 2T_m)^{1/2} / T_m + 1$
$\delta$	Correction for polarisation of medium by charged particle
$\Delta$	Delta-ray cut-off energy ( $m_o c^2$ units)
$\Delta_s$	Multiple scattering step size (mm)
$\Delta'_s$	Multiple scattering step size ( $\text{g cm}^{-2}$ )
$\epsilon_w$	Calculated electron energy deposited per unit mass in the cavity whilst containing wall medium ( $\text{MeV g}^{-1}$ )

$\epsilon_c$	Calculated electron energy deposited per unit mass in the cavity whilst containing detecting medium ( $\text{MeV g}^{-1}$ )
$\epsilon_{c_e}$	Energy per unit mass deposited in the cavity filled with the detecting medium from particles generated in the wall (external)
$\epsilon_{c_i}$	Energy per unit mass deposited in the cavity filled with the detecting medium from particles generated in the cavity (internal)
$\epsilon_{w_e}$	Energy per unit mass deposited in the cavity filled with the wall medium from particles generated in the wall (external)
$\epsilon_{w_i}$	Energy per unit mass deposited in the cavity filled with the wall medium from particles generated in the cavity (internal)
$\theta$	Azimuthal angle
$\lambda$	Mean free path (cm)
$\mu$	Macroscopic photon interaction cross-section ( $\text{cm}^{-1}$ )
$\mu/\rho$	Photon mass attenuation coefficient ( $\text{cm}^2 \text{g}^{-1}$ )
$\mu_{e/\rho}$	Effective electron mass absorption coefficient ( $\text{cm}^2 \text{g}^{-1}$ )
$\mu_{en/\rho}$	Photon mass energy absorption coefficient ( $\text{cm}^2 \text{g}^{-1}$ )
$\mu_{K/\rho}$	Photon mass energy transfer coefficient ( $\text{cm}^2 \text{g}^{-1}$ )
$\nu$	Molière distribution reduced scattering angle (equation C26)
$\rho$	Medium density ( $\text{g cm}^{-3}$ )
$\sigma$	Microscopic cross-section ( $\text{cm}^2/\text{atom}$ )
$\sigma_{KN}$	Klein-Nishina cross-section ( $\text{cm}^2/\text{electron}$ )
$\Sigma_s$	Macroscopic neutron elastic scattering cross-section ( $\text{cm}^{-1}$ )
$\phi$	Polar angle
$\phi_s$	Equations C23 and C24
$\Phi(E)$	Particle fluence
$\chi_c$	Molière distribution unit probability angle (equation C27)
$\chi'_\alpha$	Molière distribution screening angle (equation C29)
$\Omega$	Solid angle



## REFERENCES

- 1 ZEBRA-6: Dilute Plutonium-Fuelled Assembly  
Proc. International Conf. Fast Critical Experiments and Their Analysis  
Argonne National Laboratory ANL-7320, 1966  
J Adamson, K M Absalom, A R Baker, G Ingram, S K I Pattenden and  
J M Stevenson
- 2 Radiation Dosimetry (Three Volumes) Second Edition, Academic Press  
1966-1969  
Edited by F H Attix, W C Roesch and E Tochilin
- 3 Cavity-Chamber Theory  
Chapter 8 of Reference 2  
T E Burlin
- 4 The Scope of the MOZART Programme and the General Conclusions Drawn  
From It  
Proceedings of the International Symposium on Physics of Fast  
Reactors, Tokyo, Japan, 16-19 October 1973  
C G Campbell, J E Sanders, J L Rowlands and S Kobayashi
- 5 Radiation Quantities and Units  
International Commission on Radiation Units and Measurements  
July 1971, ICRU Report 19
- 6 Positron-Electron Differences in Energy Loss and Multiple Scattering  
Phys. Rev., Vol 93, page 38, 1954  
F Rohrlich and B C Carlson
- 7 Methods in Computational Physics, Vol 1, Statistical Physics,  
Academic Press (1963)  
Edited by B Alder, S Fernbach and M Rotenberg  
Monte Carlo Calculation of the Penetration and Diffusion of Fast  
Charged Particles, page 135  
M J Berger
- 8 Bremsstrahlung Cross-Section Formulas and Related Data  
Rev. Mod. Phys., Vol 31, No 4, page 920, October 1959  
H W Koch and J W Motz
- 9 The Quantum Theory of Radiation  
3rd Edition, Oxford University Press (1957)  
W Heitler
- 10 Ionisation Chambers  
Chapter 9 of Reference 2  
J W Boag
- 11 Photon Cross Sections, Attenuation Coefficients and Energy Absorption  
Coefficients from 10 KeV to 100 GeV  
NSRDS-NBS 29 (1969)  
J H Hubbell
- 12 Proceedings of International Conference on Luminescence Dosimetry  
Stanford University, Stanford, California, 21-23 June 1965

- 13 Proceedings of Second International Conference on Luminescence  
Dosimetry  
CONF-680920  
23-26 September 1968
- 14 Proceedings of Third International Conference on Luminescence  
Dosimetry  
RISO Report Number 249  
11-14 October 1971
- 15 Proceedings of Fourth International Conference on Luminescence  
Dosimetry, Kraków, Poland  
27-31 August 1974
- 16 Thermoluminescent Dosimetry, University of Wisconsin Press, 1968  
J R Cameron, W Suntharalingam and G N Kenney
- 17 The Quality and LET Dependence of Three Thermoluminescent  
Dosimeters and Their Potential Use as Secondary Standards  
Page 424 of Reference 13  
E Tochilin, N Goldstein and J T Lyman
- 18 Energy Response of Certain Thermoluminescent Dosimeters and Their  
Application to the Dose Measurements  
Page 1089 of Reference 14  
H K Pendurkar, R Boulenger, L Ghooos, W Nicasi and E Mertens
- 19 Energy Dependence of Lithium Fluoride Dosemeters and High Electron Energies  
Phys. Med. Biol., Vol 11, page 129, 1966  
A P Pinkerton, J S Laughlin and J G Holt
- 20 Energy Dependence of Lithium Fluoride Dosemeters at High Energies  
Phys. Med. Biol., Vol 11, page 131, 1966  
E H Crosby, P R Almond and R J Shalek
- 21 Energy Dependence of LiF and CaF<sub>2</sub> Thermoluminescent Dosimeters for  
High Energy Electrons  
Health Physics, Vol 14, page 266, 1968  
T Nakajima, T Hiraoka and T Habu
- 22 Energy Dependence of Lithium Fluoride Dosemeters at Electron Energies  
from 10 to 35 MeV  
Phys. Med. Biol., Vol 14, page 327, 1969  
C Binks
- 23 Lithium Fluoride Thermoluminescence Dosimetry  
Phys. Med. Biol., Vol 9, page 273, 1964  
C J Karzmare, J White and J F Fowler
- 24 Fading in Thermoluminescent Lithium Fluoride after Irradiation with  
Gamma-Ray Doses up to 1000 rad  
Brit. J. Appl. Phys., Vol 18, page 1567, 1967  
G A M Webb
- 25 Fading in Thermoluminescent Dosimetry  
Page 132 of Reference 14  
Z Spurný and J Novotný

- 26 The Effects of Fast Neutron Exposure on the  ${}^7\text{LiF}$  Thermoluminescent Response to Gamma Rays  
Health Phys., Vol 13, page 918, 1967  
B G Oltman, J Kastner, P Tedeschi and J N Beggs
- 27 Additivity of Neutron and Gamma-Ray Exposures for TLD Dosimeters  
Health Phys., Vol 18, page 157, 1970  
N Goldstein, W G Miller and P F Rago
- 28 Changes in Gamma Sensitivity of  $\text{Li}{}^7\text{F}$  Dosimeters  
Health Phys., Vol 23, page 123, 1972  
P H Bloch and R J Weber
- 29 Thermoluminescence Response of LiF to Reactor Neutrons  
Radiation Research Vol 40, page 552, 1969  
A R Reddy, K Ayyangar and G L Brownell
- 30 Response of Lithium Fluoride to Neutrons and Charged Particles  
Page 421 of Reference 12  
C L Wingate, E Tochilin and N Goldstein
- 31 Response of  ${}^6\text{LiF}$  and  ${}^7\text{LiF}$  Thermoluminescence Dosimeters to Fast Neutrons  
Nuclear Instruments and Methods, Vol 104, page 365, 1972  
Y Furuta and S Tanaka
- 32 Application of Thermoluminescence Dosimeters for Nuclear Heating Measurements of Gamma Rays and Neutrons  
Proceedings of First ASTM-Euratom Symposium on Reactor Dosimetry  
Petten, 22-26 September 1975  
S Tanaka, K Takeuchi and Y Furuta
- 33 A General Theory of Cavity Ionisation  
Brit. J. Radiol., Vol 39, page 727, 1966  
T E Burlin
- 34 Charged-Particle Interactions  
Chapter 4 of Reference 2  
H Bichsel
- 35 Range-Energy Relations for Electrons and the Determination of Beta-Ray End-Point Energies by Absorption  
Rev. Mod. Phys., Vol 24, No 1, January 1952  
L Katz and A S Penfold
- 36 Generalised Semiempirical Equations for the Extrapolated Range of Electrons  
Nuclear Instruments and Methods, Vol 103, page 85, 1972  
T Tabata, R Ito and S Okabe
- 37 An Experimental Examination of a General Cavity Theory Using a Solid State Dosemeter  
Brit. J. Radiol., Vol 43, page 54, 1970  
F K Chan and T E Burlin

- 38 The Effect of the Wall on the Fricke Dosimeter  
Int. J. App. Rad. and Isot., Vol 20, page 767, 1969  
T E Burlin and F K Chan
- 39 Measurements of Gamma-Ray Heating by Thermoluminescent Dosimeters  
TI-707-140-022, May 1972  
R J Tuttle
- 40 Gamma-Ray Heating Measurements in Zero-Power Fast Reactors with  
Thermoluminescent Dosimeters  
Nucl. Sci. & Eng., Vol 53, page 162, 1974  
G G Simons and T J Yule
- 41 ETRAN: Monte Carlo Code System for Electron and Photon Transport  
Through Extended Media  
NBS 9836/NBS 9837 (1968)  
M J Berger and S M Seltzer
- 42 McNID - A Monte Carlo Programme for Calculating the Penetration of  
Neutrons in Systems with Cylindrical Symmetry  
AEEW-R 308 (1966)  
D E Bendall
- 43 Subroutine HEITLER  
AERE-M 1956 (1967)  
A Foderaro
- 44 MUG - A Program for Generating Multigroup Photon Cross-Sections  
ORNL, CTC-17 (1970)  
J R Knight and F R Mynatt
- 45 A User's Manual for ANISN  
K-1693 (1967)  
W W Engle
- 46 DOT III - A Two-Dimensional Discrete Ordinates Transport Code  
ORNL-TM-4280 (1973)  
W A Rhoades and F R Mynatt
- 47 The MORSE Code - A Multigroup Neutron and Gamma-Ray Monte Carlo  
Transport Code  
ORNL-4585 (1970)  
E A Straker, P N Stevens, D C Irving and V R Cain
- 48 A Revision of Photon Interaction Data in the UKAEA Nuclear Data  
Library  
AEEW-M 1368 (1975)  
A D Knipe
- 49 User's Manual for the DOT II W Discrete Ordinates Transport  
Computer Code  
WANL-TME-1982 (1969)  
R G Soltesz and R K Disney
- 50 A F Avery  
Private Communication - April 1974

- 51 Bounded Estimators for Flux at a Point in Monte Carlo  
Nucl. Sci. & Eng., Vol 44, page 406, 1971  
H A Steinberg and M H Kalos
- 52 The ZEBRA Multi-Chamber Scanning System  
AEEW-M 1272 (1974)  
R G Batt, A Goodings, J Marshall, J E Sanders and D W Sweet
- 53 Spectra of Energy Released by Thermal Neutron Capture  
TRG Report 2189(R) (1972)  
E W Sidebotham
- 54 Fundamental Aspects of Reactor Shielding  
Pergamon Press (1959)  
H Goldstein
- 55 Neutron Energy-Dependent Capture Gamma-Ray Yields for  $U^{238}$  and  
 $Ta^{181}$   
Am. Nuc. Soc. Trans., Vol 13, No 2, 1970  
K J Yost, J E White and C Y Fu
- 56 The UK Programme of Datam Experiments on Energy-Deposition and  
Radiation Penetration  
EACRP-L-100 (1974)  
J Butler, M D Carter, A K McCracken and A Packwood
- 57 The MOZART MZC Calculations  
Unpublished  
A F Avery
- 58 McBOX  
Unpublished  
D E Bendall
- 59 Energy Released in Fission  
AEEW-M 863 (1969)  
M F James
- 60 FISPIN - A Computer Program to Predict Gamma and Beta Decay  
Activities and Spectra from Fissile Isotopes  
UKAEA Sept. 1971  
B L Richardson
- 61 The Elements of Nuclear Reactor Theory  
D Van Nostrand Company, Inc. (1957)  
S Glasstone and M C Edlund
- 62 Ionisation  
Chapter 7 of Reference 2  
I T Myers
- 63 Energy Loss Characteristics of Heavy Ions in Nitrogen, Carbon  
Dioxide, Argon, Hydrocarbon Gases and Tradescantia Tissue  
AERE-M 2346 (1971)  
J A Dennis

- 64 Computed Ionization and Kerma Values in Neutron Irradiated Gases  
Phys. Med. Biol., Vol 18, No 3, page 379, 1973  
J A Dennis
- 65 A Theory of Cavity Ionisation  
Radiation Research, Vol 3, page 239, 1955  
L V Spencer and F H Attix
- 66 On the Stopping of Fast Particles and on the Creation of Positive  
Electrons  
Proc. Royal Soc., Vol A146, page 83, 1934  
H Bethe and W Heitler
- 67 X-Ray and Gamma-Ray Interactions  
Chapter 3 of Reference 2  
R D Evans
- 68 High Energy Particles  
Constable and Co Ltd (1952)  
B Rossi
- 69 The Theory of Small-Angle Multiple Scattering of Fast Charged  
Particles  
Revs. Mod. Phys., Vol 35, No 2, page 231, 1963  
W T Scott
- 70 Molière's Theory of Multiple Scattering  
Phys. Rev., Vol 89, No 6, page 1256, 1953  
H A Bethe
- 71 Theory of Multiple Scattering: Second Born Approximation and  
Corrections to Molière's Work  
Phys. Rev., Vol 115, No 3, page 491, 1959  
B P Nigam, M K Sundaresan and T Wu
- 72 Inelastic Collisions and the Molière Theory of Multiple Scattering  
Phys. Rev., Vol 93, No 1, page 117, 1954  
U Fano
- 73 Multiple Scattering of Relativistic Electrons  
Phys. Rev., Vol 93, No 1, page 114, 1954  
L V Spencer and C H Blanchard
- 74 Isotopic Effect in Lithium Fluoride Thermoluminescent Dosimeters  
Phys. Med. Biol., Vol 14, page 147, 1969  
F H Attix